PULSED LASER DEPOSITION OF (SrBa)Nb_2O_6 THIN FILMS AND THEIR PROPERTIES

THÈSE N^O 3327 (2005)

PRÉSENTÉE À LA FACULTÉ SCIENCES ET TECHNIQUES DE L'INGÉNIEUR

Institut des matériaux

SECTION DE SCIENCE ET GÉNIE DES MATÉRIAUX

ÉCOLE POLYTECHNIQUE FÉDÉRALE DE LAUSANNE

POUR L'OBTENTION DU GRADE DE DOCTEUR ÈS SCIENCES

PAR

Anna INFORTUNA

dottore in fisica, Università degli Studi di Torino, Italie
et de nationalité italienne

acceptée sur proposition du jury:

Prof.N. Setter, directrice de thèse
Dr D. Marré, rapporteur
Dr P. pMuralt, rapporteur
Prof. P. Stadelmann, rapporteur
Prof. J. Trodahl, rapporteur

Lausanne, EPFL
2005

Abstract

Strontium barium niobate ($Sr_xBa_{1-x}Nb_2O_6$, shortly SBN) is a solid solution system with tetragonal tungsten bronze crystal structure. It exhibits a ferroelectric phase with only one polar axis and a transition temperature depending on the Sr/Ba ratio. This thesis studies the growth of SBN thin films, in order to obtain a ferroelectric thin film model system for the study of 180° domain switching close to the ferroelectric phase transition. SBN has been chosen not only because uniaxial, but because it is possible to tune the temperature of phase transition varying the Sr/Ba ratio. It is thus possible to study electric properties of the phase transition close to room temperature, where conduction phenomena related to defects are normally lower.

Thin films of SBN were grown by Pulsed Laser Deposition in a vacuum system constructed during this thesis work. For the formulation of a model it is desirable to have a system as close as possible to a single crystal. Therefore deposition parameters have been optimized to grow SBN thin films with the polar axis oriented perpendicular to the film plane. The films are integrated in parallel plate capacitor structures, in order to measure dielectric properties.

The stability of the ferroelectric phase is found to be sensitive to impurities; contaminants with concentration below 1% induce a lowering of the transition temperature of about 100°C. Strain as well has influence on the phase transition; in the case of substrate with thermal expansion coefficients different from the SBN ones, the SBN film is under stress. A 0.6% tensile strain induces a lowering of the transition temperature of about 100°C, this is the case of silicon single crystal substrate. Grown on strontium titanate single crystals (STO), whose thermo-mechanical properties are close to the one of SBN, the films exhibit a phase transition temperature compatible with the one measured on single crystals.

The obtained films suffer from leakage that is reduced by thermal treatment in oxygen rich atmosphere. The oxygen vacancies, created during the deposition process, are considered to be responsible of leakage. Vacancies recovery upon annealing does not

eliminate the problem, and measurement of polarization at room temperature is difficult. However, piezoelectric measurements performed on individual grains, with atomic force microscope, prove that these have ferroelectric properties; by these experiment has been proved that it is possible to switch the polarization. Films with a disordered structure of grains are much less leaky than the ones with columnar grains spanning the whole cross section. These observations lead to the conclusion that conduction goes trough the grain boundaries.

On STO single crystals, SBN grows epitaxial in Volmer-Weber mode. With a suitable preparation of the substrate surface, it is possible to induce the growth of films with different orientations of the polar axis: in the film plane, perpendicular to it or inclined of 45°. A model is proposed, explaining the epitaxial relation with the substrate on the basis of the perovskite kernel contained in the unit cell of the tetragonal tungsten bronze structure. The film grows from the nucleation of the perovskite structure that rules the orientation of the film; the high temperature at which the substrate is kept during the deposition, assure the necessary mobility for the arriving atoms to organize in the SBN structure around these nuclei. The study of literature data allows to state that such a model is valid not only for substrates with perovskite structure, but can be extended to substrates with a cubic crystal structure, like magnesium oxide.

Riassunto

Il Niobato di Stronzio e Bario è una soluzione solida di formula $Sr_xBa_{1-x}Nb_2O_6$, (nel seguito SBN), e struttura cristallina tetragonale. Questo composto ha una fase ferroelettrica con asse polare unico e la temperatura di transizione dipende dal rapporto tra concentrazione di Stronzio e di Bario.

In questa tesi viene studiata la crescita di film sottili di SBN; lo scopo è di ottenere un sistema modello per lo studio dell'inversion di polarità in domini a 180°, in prossimità della transizione di fase, per l'appunto in film sottili. SBN è stato scelto non solo per l'unicità dell'asse polare ma anche per la possibilità di variare la temperatura di transizione cambiando il rapporto tra stronzio e bario. Questo permette di effettuare lo studio delle proprietà elettriche in intervalli di temperatura non lontani dalla temperatura ambiente. Uno dei vantaggi, oltre a quelli legati alla praticità sperimentale, è la minimizazione dei fenomeni di conduzione.

I film per queso studio sono ottenuti con la tecnica nota come "Pulsed laser deposition", abbreviata PLD e il sistema di deposizione è stato costruito durante il lavoro di tesi. Dal punto di vista della modellizzazione è desiderabile avere un sistema il piu possibile prossimo a un monocristallo. Per questo motivo i parametri di deposizione sono ottimizzati per la deposizione di film con l'asse cristallino [001], coincidente con l'asse polare, perpendicolare al piano del film. I campioni cosi ottenuti sono integrati in condensatori a faccie piane e parallele, per mezzo di tecniche standard di foto-litografia.

La stabilità della fase ferroelettrica nei film di SBN, risulta essere sensibile alle impurità; la presenza di contaminanti in concentrazione inferiore all' 1% e sufficiente per indurre un abbassamento della temperatura della transizione fase di circa 100°. Anche le deformazioni hanno un influenza sulla transizone di fase; a causa dell'elevata temperatura di deposizione, quando la costante di dilatazione termica del substrato è molto diversa da quella di SBN, in prossimità della temperatura ambiente il film di SBN risulta sottoposto ad una deformazione. Deformazioni di 0.6% inducono variazioni della transizione di fase di circa 100°. È questo il caso dei substrati di silicio monocristallino.

Cresciuti su substrati monocristallini di Titanato di Stronzio (STO nel seguito), il cui comportamento termo-meccanico è prossimo a quello di SBN, i film possiedono una temperatura di transizione compatibile con quella misurata nei monocristalli.

I film ottenuti sono affetti da perdite elettriche. Questo fenomeno è ridotto da un trattamento termico in atmosfera di ossigeno, dunque una delle cause è da trovarsi nelle di lacune di ossigeno che si formano nel processo di deposizione. L'incorporazione di ossigeno tramite ricottura non elimina completamente il problema, e la misura della polarizzazione a temperatura ambiente risulta difficoltosa. Tuttavia, misure di piezoelettricità, effettuate con il microscopio a forza atomica su singoli grani del film, provano che questi ultimi hanno proprieta ferroelectriche in quanto è possibile invertire il verso della polarizzazione. Questa osservazione porta alla conclusione che la conduzione sia confinata ai bordi di grano.

Su cristalli di STO, SBN cresce epitassiale secondo il processo Volmer-Weber. Con l'opportuna preparazione della superficie del substrato, è possibile indurre la crescita di film di SBN con differenti direzioni dell asse polare. In questo modo film con l'asse polare nel piano del film, perpendicolare ad esso e inclinato di 45° sono ottenuti. Il modello di crescita proposto spiega la fenomenologia di crescita, orientazione e forma dei grani, considerando il ruolo del nucleo con struttura cristallina di perovskite, contenuto nella struttura tetragonale di SBN. Il film di SBN nuclea formando la struttura perovskite, che determina l'orientazione finale. L'elevata temperature di deposizione assicura agli atomi in arrivo, la mobilità necessaria per formare la struttura di SBN attorno a questi nuclei. Lo studio della letteratura permette di affermare che tale modello non è valido solamente nel caso di substrati con struttura perovskite, ma puo essere applicato ugualmente nel caso di substrati a struttura cubica come l'ossido di magnesio.

Contents

Chapter 1

Introduction

1.1 Motivation and primary goal of the work

Strontium barium niobate ($Sr_xBa_{1-x}Nb_2O_6$, shortly SBN) is a very interesting material from the point of view of both fundamental research and application.

Single crystals of SBN show strong piezo,[1] and pyroelectricity,[2] a large spontaneous polarization and high linear electro-optical coefficients.[3] SBN undergoes a ferroelectric phase transition in the temperature range from 60 to $250°C$, depending on the Sr content. SBN is a uniaxial ferroelectric and shows relaxor behavior for $x>0.5$. Owing to its intrinsic charge disorder, and to the unique polarization direction, strontium barium niobate is considered a model system for the three-dimensional ferroic random field Ising model.[4]

The relatively low critical temperature of SBN allows to operate devices near to them and thus to profit from enhanced properties such as high pyroelectric coefficients. SBN with $x=0.5$ (critical temperature 120°C), is one of the classical crystalline materials applied in pyroelectric uncooled infrared detectors. Doping with rare earth is another fruitfully and widely employed possibility to tune the properties of SBN.

All the previously mentioned reasons motivated the effort in production and characterization of SBN single crystals, starting from the early work of Jamieson and Glass in 1968.[2,5] Recently, production of defect free crystals has been triggered mainly by the realization of optical applications; they are investigated for optical memory, optical frequency conversion and wave guide applications. The high costs and the difficulties related to the production of big and defect free crystals, stimulated the research on SBN ceramics. Down scaling of devices and on chip integration motivated research on thin films. Potential applications are: infrared detectors, optical memories, optical switches, and surface acoustic waveís devices. While pyroelectric applications work well with polycrystalline c-axis textured films, electro-optic applications require monocrystalline epitaxial films. There is thus some interest to study integration onto Si based microsystems as well as in epitaxial growth on single crystals substrate.

As will be shown in the following literature review, the knowledge in SBN thin film growth and resulting properties is still rudimentary. This work is devoted to the growth and characterization of SBN thin films by pulsed laser deposition (PLD). The first aim was to fabricate SBN capacitors structures, integrated on silicon, by growing polycrystalline SBN films on suitable electrode films withstanding the high growth temperature. The second goal was to understand growth mechanisms governing film orientation and texture, through the study of epitaxial growth. The third goal was to investigate fundamental properties of the obtained films and capacitors.

1.2 SBN: structural and physical properties

1.2.1 Crystal structure

The strontium barium niobate solid-solution series crystallize in the tetragonal tungsten bronze (TTB) structure. At room temperature it has the symmetry of the space group $P4bm$ for $0.25 < x < 0.75$. It belongs to the 4mm point group in the ferroelectric phase and changes to the 4/mmm when in the paraelectric phase. The full formula per unit cell is: $(Sr, Ba)_5Nb_{10}O_{30}$. The unit cell lattice parameters are a=b=1.245 nm c=0.395 nm. It consists of a framework of ten oxygen octahedra linked in such a manner as to form three different types of tunnels running through the structure parallel to the four fold axis (c-axis). The tunnels are delimited by octahedra chains that resemble those in the perovskite structure (figs.1.1,1.2).

Of the six available sites for Sr and Ba, only five are actually occupied. That leads to a certain degree of disorder responsible for the dielectric behavior of SBN. The Ba^{+2} cations, being substantially larger than Sr^{+2} (Ba 1.75, Sr 1.58), find place in the bigger tunnels with pentagonal cross-section, which have a total occupancy probability of 88% for all x. The Sr^{+2} cations can be in both the pentagonal and squared cross-secion tunnels, the latter have an occupancy of 71-72%, increasing with Sr content. The broad channels are statistically occupied by both Ba and Sr, the Sr atoms are displaced from the symmetry planes m_{xy} while the Ba atoms occupy the symmetric position[5] (fig.1.1).

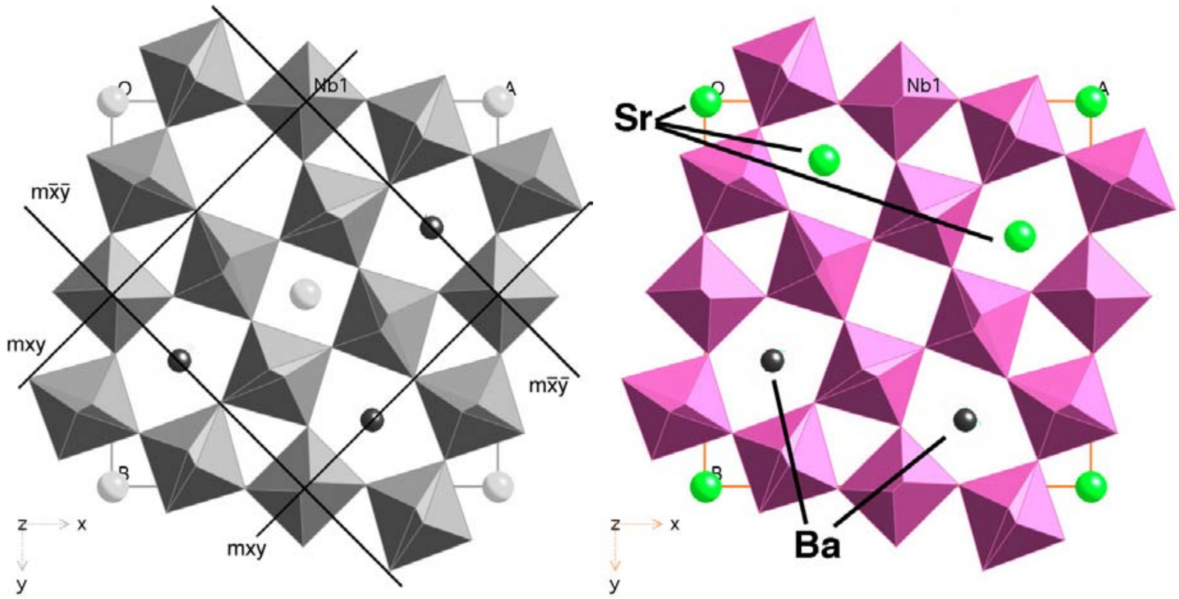

a) b)

Figure 1.1: SBN50 unit cell: two possible configurations for the distribution of Sr/Ba atoms. The octahedra have oxygen atoms at the vertices and a Nb atom is sitting in the center, they are actually tilted along the c-axis and the splitting of vertices in the picture indicate the two possible position of oxygen.

The triangular cross-section tunnels are empty and Nb^{+5} cations occupy the central site of the octahedra. In the Nb-octahedron the apical oxygen atoms, located in the planes of Sr and Ba atoms, are statistically disordered over two positions with a probability of 0.5. The distances between the split positions increase monotonically with an increase in the strontium content, giving a wider tilting of oxygen octahedra along the c axis. In other words, the planes statistically occupied by Sr and Ba atoms also contain statistically arranged apical oxygen atoms of the Nb-octahedra.[6–9] Upon heat treatment at high temperature super-lattice structures due to ordering in the octahedra tilt and in the occupation of pentagonal and squared cavities, has been observed.[10, 11] Because of the structural complexity, a wide range of cationic substitutions can be accommodated. The presence of impurities, as well as non-stoichiometry, does not induce conduction in SBN but strongly affect its ferroelectric properties. Therefore doping is widely used in this sense to improve the characteristic of the material for specific applications. The main effects of doping are the decrease of the transition temperature and the enhancement of the relaxor behavior.

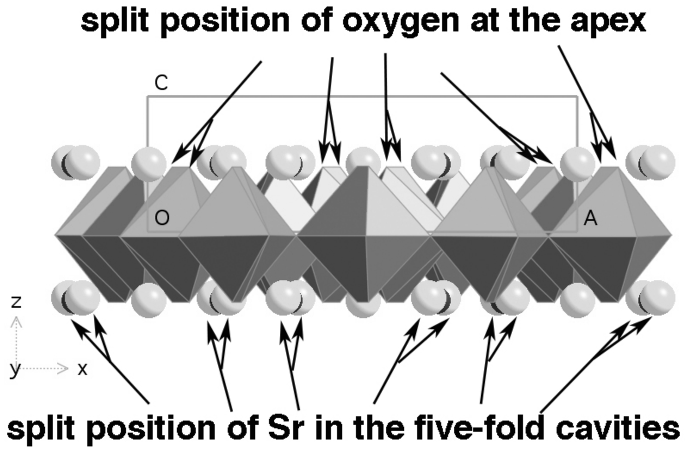

Figure 1.2: SBN unit cell view along the a or b axis

1.2.2 Growth of single crystals

The growth of SBN single crystals is relatively easy for the only congruent melting composition SBN61[12](here and in the following the number after SBN indicate the Sr content, e.g. x=0.61→61). Crystals of 2-3 cm diameters are obtained[13, 14] for SBN50 as well. The crystals grow as cylinders and develop natural facets. The direction of growth occurs regularly along the polar axis. Since SBN has a unique polar axis, problems of 90°C twins growth do not occur. However other problems are encountered:[15]

- because of the high melting temperature (1500°C), volatilization and oxidation-reduction problems are common.
- the low thermal conductivity makes it difficult to keep the temperature uniform during cooling
- distribution of Sr and Ba in the five and four fold tunnels is strongly sensitive to cooling rate variation and causes striations
- striations are very difficult to suppress in doped crystals

Ce-doped SBN:60 have been developed with minimum or no striation.
A complete review of the chronological development of SBN in terms of crystals growth and applications, can be found in the paper of Neurgaonkar et al.[16]

1.2.3 Properties of SBN

Polarization in the tungsten bronze structure arises from the displacement, in the same direction, of all the metal atoms, from the nearest mean plane of oxygen atoms. This direction determines the ferroelectric polarization axis.[5] SBN is a uniaxial ferroelectric with the polarization along the four fold axis (c axis). In the ferroelectric phase Sr, Ba and Nb atoms are displaced along this axis, the Nb atoms giving the major contribution to polarization.[17] Above the ferroelectric phase transition temperature , in the paraelectric phase, Sr, Ba and 20% of Nb atoms move into the oxygen planes, while the other 80% are equally displaced above and below the oxygen planes.

The ferro to paraelectric phase transformation is of second order. The Curie temperature changes with the Sr content, varying from 60°C for SBN75 to 250°C for SBN25. The replacement of Ba by Sr leads to a relaxor behavior, firs appearing at Sr/Ba=1 and getting stronger for larger Sr/Ba ratio.[2,18] An additional phase transition between 60 K and 80 K has been found.[19] At this transition the crystal's symmetry changes from point group 4mm to m and the polar axis tilts away from the c direction of the tetragonal lattice to the a axis in the monoclinic lattice as temperature decreases.

1.2.3.1 Relaxor behavior

Relaxor ferroelectrics are a special group of ferroelectric materials. They are distinguished from classic ferroelectrics by the following properties:[20]

- a broad peak of the dielectric constant as a function of temperature
- a strong frequency dependence of the temperature at which the maximum of dielectric constant is reached
- the existence of polar regions at temperatures well above the maximum of the dielectric constant

The peak of dielectric constant in relaxor ferroelectrics does not correspond to a structural phase transition as it does in conventional ferroelectrics. The intrinsic compositional disorder of relaxor crystal structure is considered to be responsible for the existence of randomly distributed polar regions at temperatures above the dielectric maximum.[21,22] Experimental evidence of such polar regions has been firstly given by optical measurements on Lead Magnesium Niobate and Lead Zirconium Niobate.[23] Because of the uniaxial nature, the relaxor behavior of SBN has been interpreted in terms of the Ising model.[4,20,24] The random distribution of Sr and Ba cations in the case of pure SBN and the addition of higher valence cations in the case of doped SBN, are assumed to be responsible for random fluctuation of the crystalline internal electric field. At high temperature these fluctuation stabilize dynamic polar nanodomains.

Lowering the temperature below T_{max} enhances the interaction between domains until a homogeneous ferroelectric state is reached.

The temperature dependence of polarization has been studied in SBN single crystal samples.[25–27] Its decay with temperature is not as sharp as expected for a second order phase transition. A non zero value of polarization is found above the temperature of the dielectric maximum; it becomes zero at a temperature which is independent from the composition. It has been found that, upon the application of an electric field above the apparent phase transition temperature, a preferential polarization state can be induced even if the field is removed before cooling trough the phase transition.[26] The material keeps memory of this state as is shown by asymmetric coercive field and fast aging of polarization upon cycling.

1.2.3.2 Dielectric properties

The reported data on dielectric properties of SBN single crystals, are in good agreement to each other.[1,2,28] Not the same situation is found for polycrystalline SBN.[29–31]

Extensive work on dielectric and optical characterization of single crystals has been done for different composition and doping. In polycrystalline bulk samples, relaxor behavior has been found in all the composition. The temperature of the maximum of dielectric constant as well as other properties is strongly dependent on sintering conditions. Such differences in measured values can be attributed to the different heat treatment histories of the material, which is thought to affect the Sr site distribution.[30]

In thin films this behavior is further complicated by leakage.

Dielectric constant ϵ_{33}/ϵ_0	400
Dielectric loss tanδ	0.003
Pyroelectric coefficient (300K) ($10^{-2}\mu C/cm^2$)	6.0
Spontaneous polarization (300K) ($\mu C/cm^2$)	36.0
Curie temperature T_c (K)	394

Table 1.1: Some properties of SBN50 single crystals at room temperature.

Crystal	ϵ_r	spont. pol $\mu C/cm^2$	$T_m(1kHz)$
SBN73	8200	33.1	57
SBN67	1800	33.6	67
SBN60	610	34.4	80
SBN48	380	36	116
SBN25	180	39.5	196

Table 1.2: Room temperature dielectric properties of SBN single crystals along the c axis and temperature of the dielectric constant maximum T$_m$.

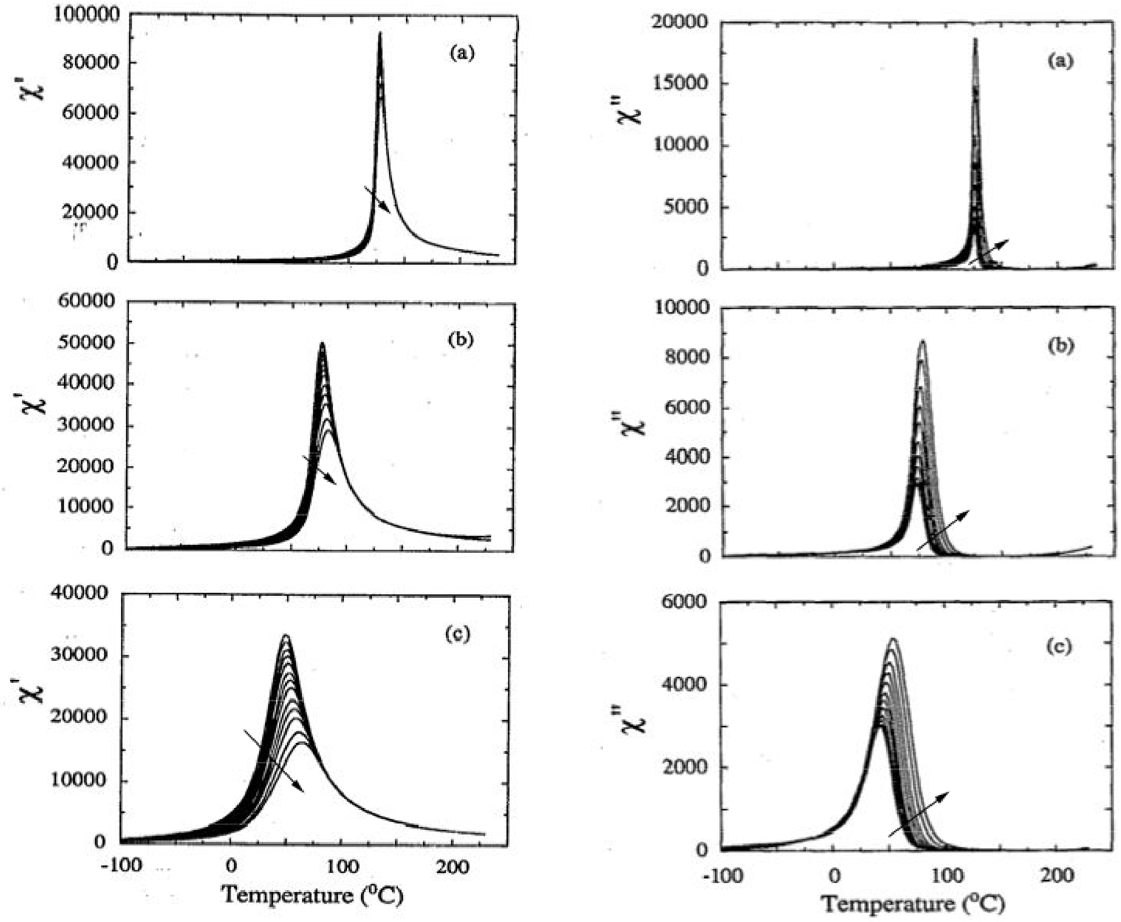

a) b)

Figure 1.3: Real and imaginary part of dielectric constant (here indicated by $\chi\prime$ and χ'' respectively) as a function of temperature and frequencies (the arrows indicate increasing freq.) for various Sr content: a)0.5, b)0.6, c)0.75 at% Sr.[28]

1.2.3.3 Superstructures

Physical properties of SBN are expected to depend on the disorder in the TTB structure, i.e. in the partially unoccupied sites. Depending on heat treatment, some ordering and creation of superstructure has been observed.[32] However a precise relationship between specific unusual properties and structure details has not been established yet. A hierarchy of domain states has been observed using TEM and selected area electron-diffraction for SBN50.[11] At $-75°C$, a structural transformation has been reported in SBN50.[33] Lower-temperature phase transformations have been reported by birefringent studies[34] and Raman spectroscopy[35] at $-100°C$, by structural studies at $-160°C$,[36] and by dielectric constant measurements at$-260°C$.[37]

The behavior of dielectric losses expressed as tanδ (see fig.1.5), has been investigated for SBN50, SBN60 and SBN75.[38] Besides the anomaly related to the ferroelectric phase transition, a second anomaly in the temperature range -150 to $-50°C$ is observed. This low temperature anomaly has been associated with an incommensurate structure appearing at this temperature.[38] It has been observed that a bias field applied along the c-axis suppresses the peak of tanδ at the ferroelectric phase transition (Fig. 1.4).

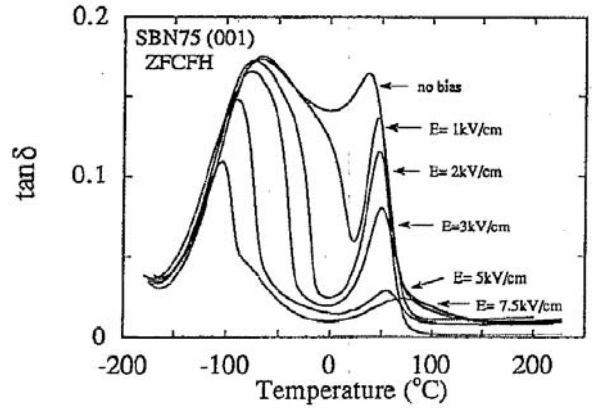

Figure 1.4: 10^4Hz phase component (tanδ) of the dielectric response for SBN 75/25 as a function of temperature, under various electrical biases.[38]

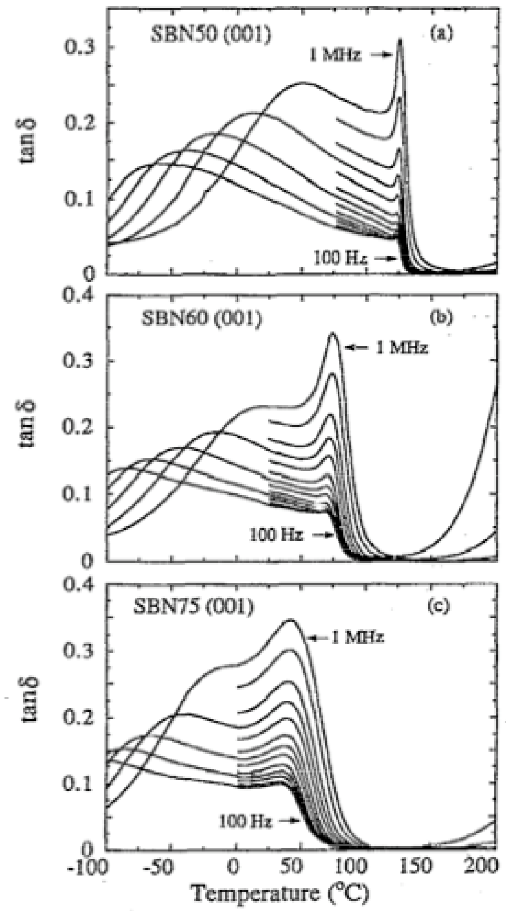

Figure 1.5: Phase component (tanδ) of the dielectric response as a function of temperature and frequency for various SBN compositions: a)SBN50, b)SBN60, c)SBN75.[38]

1.2.3.4 Optical properties

Most of the work on SBN, both single crystals and thin films, targets at optical properties and possible applications. The birefringence of SBN can be changed by application of an electric field. Two effects are obtained: a linear electrooptic effect and an electrooptic memory effect. In a poled crystal the remanent polarization is accompanied by a remanent birefringence that can be switched by a voltage pulse. Using the memory effect, volume holographic storage can be realized. SBN crystals have excellent linear electrooptic properties with low half-wave voltages and very high electrooptic coefficient r_{33}. For example, r_{33} can vary from 400 to 1350 pm/V for compositions ranging from SBN:60 to SBN:75, which is 10–40 times r_{33} for congruently grown lithium niobate (30 pm/V), the industry standard. Illumination of a photorefractive crystal with an inhomogeneous light pattern yields refractive-index modulation, which in SBN75 composition and the doped SBN60, is large compared to other photorefractive materials. Doping SBN61 with Ce is noticeably effective in improving the photorefractive properties[39]

1.2.3.5 Pyroelectric properties

SBN shows strong pyroelectric effect and single crystals have a large pyroelectric coefficient at room temperature. Properties as function of composition and temperature have been extensively studies by Glass.[2] Using the pyroelectric effect in SBN, infrared detectors have been fabricated. The room temperature characteristic of these detectors can be improved by changing the ration Sr/Ba or by doping by Pb or La. Even a thin plate of SBN has a high absorption capacity in the infrared region above $10\mu m$, no infrared absorption layer is needed. The main shortcoming of SBN is that its dielectric constant is too high for application at high frequencies. Thus, SBN thin-film detectors are used for small area, low-frequency detectors.

Composition	pyro. coeff.$10^2 \mu C/m^2 K$
SBN25	3.0
SBN46	4.3
SBN48	6.5
SBN54	8.0
SBN60	8.5
SBN67	11.0
SBN73	28.0
SBN75	31.0

Table 1.3: Pyroelectric coefficients of SBN single crystals at room temperature.

1.2.3.6 Piezoelectric properties

Piezoelectric properties have not been extensively investigated in SBN. Surface acoustic waves have been studied in SBN50 and SBN60 single crystals[1, 40–42] Reported d_{33} coefficients are listed in table 1.4. As in the case of optical properties, doping enhances piezoelectric response.[1]

	d_{33} pC/N
SBN75	670
SBN60	180
SBN50	110
SBN60:La	650

Table 1.4: Piezoelectric coefficients of SBN single crystals at room temperature.

1.2.3.7 Effect of doping

Doping has qualitatively the same effect as increasing the Sr/Ba ratio, it enhances the relaxor behavior. The addition of rare-earth metal in SBN61 single crystals is accompanied by an increase in the permittivity at room temperature, which is caused by a decrease in the phase transition temperature and a smearing of the transition itself. The increase in dielectric constant at room temperature is accompanied by an increase in other parameters as piezoelectric coefficient and linear electrooptic coefficient.[43]

As shown in Table 1.5, the influence of the rare-earth metals on the transition temperature is much more efficient than the change in Sr/Ba ratio: the difference of 35° between SBN75 and SBN61, can be obtained by doping with 1-2%at. of the rare-earth metal.

The nature of the profound effect of doping has been analyzed in the case of Ce. It has been shown that the cation predominantly occurs in the charged state +3 and, most likely, replaces Sr, i.e. it can occupy both the pentagonal and squared tunnels, leading to an increased disorder.

Similar effects have been achieved by the introduction of transition metal impurities like Cr and Ni[44,45]

Crystal	dopant in wt%	T_{max} ($°C$) (1kHz)
SBN75		48
SBN61		83
SBN61:Tm_2O_3	2.0	54-56
SBN61:Nd_2O_3	1.0	58-60
SBN61:La_2O_3	1.0	61
SBN61:CeO_2	0.4	63
SBN61:CeO_2	1.6	27-30
SBN61:La+Ce	1+0.01	35-37
SBN61:Yb_2O_3	2.6	62
SBN61:Tb_2O_3	1.0	70

Table 1.5: Influence of dopants on the phase transition temperature.

1.2.4 Thermodynamics of ferroelectrics

The Landau-Ginzburg-Devonshire (LGD) theory provides phenomenological description of phase transitions. The state function usually used to describe the system is the Gibbs potential, a Legendre transformation of internal energy U:

$$G(T, X_i, P) \quad = \quad U(S, x_i, P) - TS - X_i x_i \tag{1.1}$$

where T is the temperature and S is the entropy. $X_i x_i$ is the work done on the system by mechanical forces with: stress X_i and strain x_i. In order to obtain the stable state of the system the Gibss energy is expanded into even Taylor series in P, the so defined G reaches the minimum at constant stress and temperature.

$$G = G_0 + \frac{\alpha}{2}P^2 + \frac{\beta}{4}P^4 + \frac{\gamma}{6}P^6 \tag{1.2}$$

By the minimization of the Gibbs elastic energy, the following properties of ferroelectric materials are found:

- the existence of a phase transition at a given temperature
- the appearance of a spontaneous polarization as well as of hysteresis below the transition temperature
- the existence of anomalies in the dielectric constant and in other thermodynamic quantities at the transition temperature

Two different kind phase transition are possible depending on the sign of the coefficient β: in transition of the first order ($\beta < 0$) the order parameter of the system has a discontinuity at the critical temperature, i.e. its value makes a jump at this temperature. In second order transition ($\beta > 0$) the there is no abrupt change in the value of the order parameter which, in this case, is a continuous function of temperature. Looking for stable state with finite polarization asks for γ to be positive.

Electric field E and dielectric stiffness ϵ^{-1} are calculated as:

$$\frac{\partial G}{\partial P} = E \quad = \quad (\alpha P + \beta P^3 + \gamma P^5) \tag{1.3}$$

$$\frac{\partial^2 G}{\partial P^2} = \epsilon^{-1} \quad = \quad (\alpha + \beta P^2 + \gamma P^4) \tag{1.4}$$

In the case of a second order phase transition, terms up to power of 4 are considered in the expansion of the Gibbs free energy. The paraelectric phase corresponds to:

$$
\begin{aligned}
P &= 0 \\
\epsilon^{-1} &= \alpha = \alpha_0(T - T_0) \qquad (1.5) \\
\text{for} T &> T_0
\end{aligned}
$$

Equation 1.5 is the Curie-Weiss law for ferroelectrics. The Curie temperature T_0 is identical to the critical temperature in case of second order phase transitions.

Below the critical temperature T_0, P becomes different from zero,

$$P^2 = \frac{\alpha}{\beta} = \frac{\alpha_0(T_0 - T)}{\beta} \qquad (1.6)$$

and the dielectric stiffness is:

$$\epsilon^{-1} = 2\alpha_0(T_0 - T) \qquad (1.7)$$

1.2.4.1 Effect of stress

External stresses X_i have a strong influence on the phase transition because there is a coupling between the order parameter and the elastic properties of the material.[46]

The external stress X_i enters the Gibbs elastic energy as:

$$
\begin{aligned}
G_1 &= G_0 + \frac{\alpha}{2}P^2 + \frac{\beta}{4}P^4 + \frac{\gamma}{6}P^6 \\
&- \frac{1}{2}s_{11}^D(X_1^2 + X_2^2) - \frac{1}{2}s_{33}^D(X_3^2) - \frac{1}{2}s_{12}^D(X_1X_2) - \frac{1}{2}s_{13}^D(X_1 + X_2)X_3 \\
&- Q_{33}X_3P^2 - Q_{13}(X_1 + X_2)P^2
\end{aligned}
$$

with s_{ij} elastic compliances and Q_{ij} electrostrictive coefficients (the case of uniaxial ferroelectric, with $P = P_3$, is considered). The expression for the dielectric constant in the paraelectric phase becomes:

$$
\begin{aligned}
P &= 0 \qquad (1.8) \\
\alpha &= \alpha_0(T - T_0) \qquad (1.9) \\
\epsilon^{-1} &= \alpha_0(T - (T_0 + \frac{1}{\alpha_0}2Q_{13}(X_1 + X_2))) \qquad (1.10)
\end{aligned}
$$

Critical temperature and polarization are affected by such stresses.[46]

1.2.4.2 LGD theory applied to SBN

Interpretation of measured properties in the framework of the LDG theory has been attempted.[28,47,48] Detailed fitting of measurements has been performed for SBN60 single crystals.[47] The dielectric stiffness has been found to follow a linear Curie-Weiss law both above and below T_0. Data from the paraelectric phase give a Curie constant value (C=1/($\epsilon_0\alpha_0$)) of $4.1 \times 10^{5\circ}C$ and $T_0 = 75°C$. In the ferroelectric phase the Curie constant is $4.5 \times 10^{4}\circ C$ and $T_0 = 69°C$. The phase transition is considered to be of near second order and the difference between the critical and the Curie temperature is attributed to the relaxor behavior. From pyroelectric measurement it is found that the Gibbs energy should be expanded to at least the eight order, and coefficients of terms up to the sixth should be considered as function of temperature. Equivalent behavior has been found in other SBN composition, in doped crystals and other tungsten bronzes ferroelectrics.[3]

1.3 SBN thin films

Thin films of SBN have been deposited by various techniques such as: sol-gel process,[49,50] metal-organic chemical vapor deposition,[51,52] plasma enhanced CVD, RF magnetron sputtering,[53,54] PLD[55–57] and a combination of PLD and sol-gel.[58]

Different Sr:Ba content and different doping elements have been chosen in order to enhance specific properties necessary for particular applications. Doping is particularly effective in improving optical and pyroelectric properties.[44,59,60]

A sharp interface between film and semiconductor substrate is fundamental for ferroelectric gate transistors. Directly grown on Si wafer, SBN diffuses in to the substrate leading to the formation of a SiO_2 layer at the interface. This interfacial layer strongly degrades the dielectric properties of the metal-insulator-semiconductor structure.[61] Growth on SiO_2/Si substrate has been investigated for the fabrication of wave guides, SBN diffusion in SiO_2 posing serious problems. A thin MgO layer has been successfully used as diffusion barrier.[62,63]

The high crystallization temperatures, of 700° or higher, which is common to all deposition methods, make the choice for a suitable bottom electrode a difficult task. There are very few materials that can withstand such temperatures without losing mechanical stability or reacting with the SBN film. Platinum as well as conducting oxides thin film, such as RuO_2, $SrRuO_3$, YBCO and $LaNiO_3$ could not pass successfully the test.[54,56]

Epitaxial growth of SBN thin films is desirable to optimize film properties for any application, and is of particular importance for optical applications. It has been obtained by different deposition methods[50,51,55,64–68] on different substrates. The most commonly studied substrate is (100)oriented MgO single crystal. Not only the low lattice mismatch with SBN (001) (about 1.2 %), but its refractive index (n=1.735), much lower then the SBN one ($n_o = 2.31$ $n_e = 2.281$), makes of it a perfect substrate for optical applications. (100)oriented single crystal of $SrTiO_3$ has a bigger lattice mismatch with SBN (001)(about 5%). However, as it can be made conductive by doping and therefore used as an electrode, it is preferable for electrical characterizations. SBN epitaxial growth has been obtained as well on multilayer structures like $LaNiO_3/CeO_2/YSZ/Si(100)$.[68]

1.3.1 Dielectric properties

SBN50 deposited on Pt/Si(100) by PLD have been found with transition temperature at 80°C, 40° lower than the single crystal value.[61] Xu et al.[50] report transition temperature 290°C for SBN60, whereas the single crystals have transition at 80°C. P-E hysteresis loops measured on SBNx thin film deposited by sol-gel on Pt/MgO, with polar axis perpendicular to the film plane, show polarization remanence and coercive field values increasing with increasing Sr content, the maximum value is $P_r = 30(\mu C/cm^2)$ at x=75.[49] This trend is not consistent with properties measured for bulk single crystals. In Table1.6 thin film properties found in literature are summarized .

Properties of thin films are remarkably different from bulk properties. In addition the measured values strongly depend on experimental condition. This is an indication of how much SBN film is sensitive to growth condition and substrate properties. Compared to bulk processing, the processing temperature of a thin film is very low. As this parameter has a strong influence on the intrinsic disorder in the structure, it is probably responsible for the great variability of results reported.

ref.	comp.	synthesis	ϵ_r	loss	$P_r(\mu C/cm^2)$	$E_c(kV/cm)$
[69]	SBN30	sol-gel	-	-	5.1	1.2
[70]	SBN30	PLD	1200	-	12.8	3.1
[71]	SBN30	sol-gel	600	0.05	2	3
[57]	SBN30	PLD	-	-	3.1	1.28
[62]	SBN50	PLD	-	-	26	20
[72]	SBN50	organic gel	221	_	8.17	16.9
[61]	SBN50	PLD	200	_	_	_
[56]	SBN50	PLD	_	_	0.1	51
[73]	SBN50	sol-gel	79		1.9	180
[74]	SBN50	PLD	210	-	-	-
[49]	SBN60	sol-gel		_	25	70
[50]	SBN60	sol-gel	-	-	10	30
[60]	SBN75	organic gel	700	0.1	_	_
[75]	SBN75	polimeric resin	-	_	1.1	50.5

Table 1.6: Room temperature dielectric properties of SBN thin films obtained by different methods.

1.3.2 Thermodynamics of epitaxial film

In thin films, the substrate exerts a two dimensional clamping that induces stresses. The effect of clamping and misfit strain has been interpreted in the framework of the LGD theory.[46,76] In the case of a uniaxial ferroelectric, the phase transformation temperature has been found to vary linearly with the misfit strain, it is increased by compressive stress and decreased by tensile stress. Compression thus stabilized the ferroelectric phase at temperature higher than the temperature of the phase transition in the bulk material. The phase transition can be changed from first to second order and the spontaneous polarization can vary significantly.

The estimation of the misfit strain should take into account the effect of stress relaxation with increasing film thickness. The formation of misfit dislocations above a critical thickness[77] is efficient to release the strain and thus reduces the effect of epitaxial growth on the electric properties of the film.

In order to take into account the effect of internal stresses due to epitaxy the Gibbs elastic energy (1.10) has to be modified by the following Legendre transformation:[46,76]

$$G^f = G_1 + x_1 X_1 + x_2 X_2 \tag{1.11}$$

where x_i and X_i are the in plane strain and stress induced by the substrate respectively. Shear stress is zero in the case of isotropic thermal expansion coefficients of the substrate. In case of in plane isotropy of the film $x_m = x_1 = x_2$. The shift in the transition temperature depends linearly on the strain as:[76]

$$\Delta T(x_m) = \frac{4}{\alpha_0} \frac{Q_{13}}{s_{11} + s_{12}} x_m \tag{1.12}$$

This is for the case of uniaxial ferroelectric with out of the film plane orientation of the polarization axis.

1.4 Thesis outline

As evidenced by the literature review of section 1.3, a detailed characterization of SBN film's ferroelectric properties, comparable to the work done on single crystals , is still missing. The first step to fill this gap is to get knowledge in processing, in order to establish a route for the realization of films with reproducible properties. In the present work the growth of SBN thin film by PLD is studied.

In **chapter II** are introduced:

- the working principles of pulsed laser deposition (PLD)
- the deposition systems used in this work
- the methods used for the structural characterization of the deposited films

Chapter III is devoted to the structural characterization of films grown on substrates relevant for integration in semiconductor technology. Special attention is devoted to the choice of the substrate that we wanted to act as bottom electrode. The goal is to grow highly (001) oriented films. The first choice is a standard platinum electrode grown on a silicon wafer, normally used for devices based on $PbZrTiO_3$ (PZT). Iridium electrodes will be considered as it is a good barrier against oxygen diffusion. Because of its importance for integration in microelectronic circuit, direct growth on silicon (100) will be studied as well.

Chapter IV presents the results obtained for the epitaxial growth of SBN.
The theory of epitaxial growth, relevant to our case, is summarized. The STO single crystal's properties are then introduced, together with the preparation techniques of the surface employed to control the epitaxy. Finally, the epitaxial growth of SBN is described and discussed.

The subject of **Chapter V** is the functional characterization of SBN thin films. Materials compatibility there becomes an issue of great importance. Ferroelectric properties of the obtained samples (the system film-substrate) will be studied with special attention paid to the phase transition, and compared to single crystal properties.
The first part describes the effect of contamination. Dielectric properties are measured

as function of temperature and the results will be interpreted in terms of the Landau-Ginzburg-Devonshire theory. The second part is dedicated to epitaxial films on STO substrates. The problem of conduction is addressed by the use of AFM measurements. The dielectric properties are compared with literature data on single crystals.

Chapter 2

Experimental

2.1 Pulsed Laser Deposition

Pulsed laser deposition (PLD) is a physical method of thin film deposition where a pulsed laser beam, of wavelength in the UV range, is employed to ablate a target composed of the desired thin film material. PLD attracted much attention over the last 20 years, as it enables fabrication of multi-component stoichiometric films from a single target.[78–80]

The experimental PLD setup (fig. 2.1) consists of a vacuum chamber containing targets and substrate holders. The chamber is equipped with a UV transparent window. Outside the chamber, a UV transparent lens focuses the laser beam onto the target surface. The use of additional optical elements, such as mirrors and beam splitters, depends on the system complexity. Much care has to be taken to the fact that each element reduces the intensity of the beam. The evaporation power source, i.e. the laser, is decoupled from the vacuum system. This makes the technique very flexible.

The useful range of laser wavelengths for thin-film growth by PLD lies between 200 nm and 400 nm. Most materials used for deposition work exhibit strong absorption in this spectral region. With an appropriate choice of the laser, any material can be ablated congruently. In addition, the growth can be carried out in a pressure of any kind of gas, reactive or not.

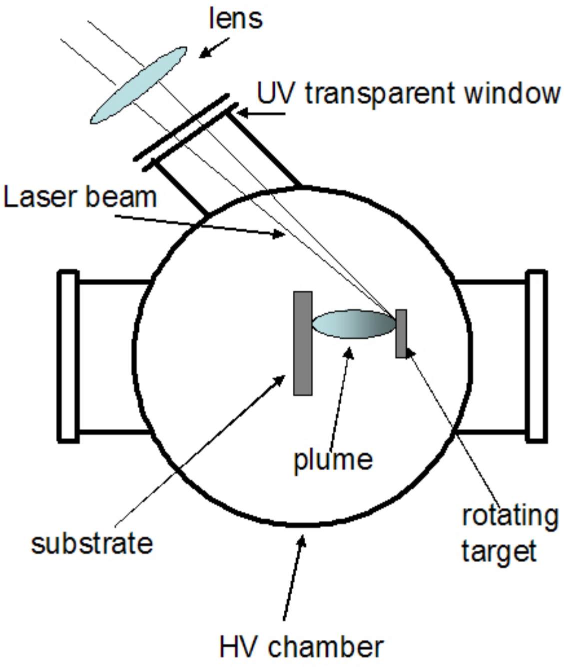

Figure 2.1: Schematic of a generic PLD deposition system.

The laser target interaction is a very complex physical phenomenon.[81] It depends on laser characteristics and optical, topological and thermodynamic properties of the target.[82] Upon absorption from a solid surface, the electromagnetic energy of the laser beam is converted first in electronic excitation and then in thermal, chemical and mechanical energy, that causes evaporation. From the point of view of film formation, the important fact is that ablation takes place in a time interval short enough to suppress the dissipation of excitation energy beyond the actually ablated volume. In this way, the damage of the remaining target is minimized and segregation of the different components largely avoided.

Targets, usually in disk shape, are normally rotated and scanned with respect to the laser beam in order to suppress surface roughening. As a consequence the density of particles of material in the plume is minimized (fig.2.2b). It is important that the target is not suffering modification during ablation, both structurally and chemically. Such modifications would change the further interaction with the laser beam (light absorption and heat conduction).[83]

The most commonly used targets are ceramics ones. Dense small-grained targets are preferable because single-crystalline or coarse-grain-polycrystalline ones are damaged by thermal shock after few pulses and particle ejection becomes more likely. Dense ceramics adsorb the radiation better and have lower thermal conductivity thanks to grain boundaries. Both properties enhance a local material-radiation interaction.

The evaporated species consist of energetic evaporants congruent with the target (atoms, molecules, electrons, ions, clusters). Together they constitute what is called the plume. After irradiation, the plume rapidly expands into the vacuum in a jet that remains anyhow narrow allowing for small area deposition only.[84,85] This is the most important obstacle for the application of PLD in industrial production. However, possible evolutions of PLD that would allow for large scale deposition have been proposed.[86] The angular distribution of the produced plasma is strongly forward directed and is described by a $cos^n\theta$ law, where θ is the angle with the surface normal.[87] The exponential increases with laser fluence and spot size, leading to a narrowing of the plume, for a $1.5 \times 3.5mm$ spot size $n \approx 10$.

The ablated species have energies between 10 and more than 100 eV, depending on the material. The bombardment of the growing film by such energetic particles acts on its properties and can have a positive or negative effects on morphology, stoichiometry, and microstructure.[88] Even though the ablation is congruent, due to differences in transport of different species or in sticking or desorption coefficients, the film deposited can be non-stoichiometric.[89] The presence of particles in the deposited film is characteristic of laser ablation. They can be classified in: clusters formed in the vapor phase, solidified melt drops coming from the melted surface (about $1\mu m$), solid grains (up to 10 microns) ejected from the surface because of thermal stress.[90,91]

2.1.1 The ablation process

Above a threshold laser fluence (the fluence is defined as the laser pulse energy per unit area at the target), a luminous plume of material is ejected normal to the target surface.

The rapid ablation rate, the stoichiometric transfer and the forward directed plume may be explained by models in which subsurface heating of the target occurs. The cause can be either the laser beam itself or the recoil pressure of the material evaporated in the initial part of the laser pulse. In the subsurface heating model, the laser beam is considered as a heat source on the target surface. Upon irradiation, the temperature throughout the target increases due to the absorption of the laser light. The front surface of the target begins to evaporate almost immediately, the heat of vaporization required being supplied from a layer immediately below the front surface. In this way the surface evaporation provides a cooling mechanism. This can lead to temperatures below the surface of the target which are higher than the temperature of the evaporating surface. The evaporation occurring at the surface extracts heat from a depth equal to the thermal diffusion length $L = (2D\tau)^{1/2}$ where D is the thermal diffusivity and τ the pulse length.[92] If the optical penetration depth is larger than L, it is clear that a region below the surface continues to be heated by the laser pulse. If the temperature achieved in this subsurface layer is high enough to result in vaporization, then the underlying material will explode out from the target, taking the surface layers with it and forming a highly directed plume of ablated material above the target. The high speed of material removal explains the congruent nature of the ablation process since there is no time for segregation. In addition, the occurrence of droplets of previously molten material on the surface of the film is explained.[93]

2.1.2 The plume

Studies of the plume included spectroscopic, photographic and theoretical analysis. The plume has two notable features (Fig. 2.2a)).

- It is directed perpendicular to the target surface.
- It is brightly colored.

By analogy with the well known flame tests it may be assumed that the colors arise from the electronic excitation of different spectroscopic species within the plume. For

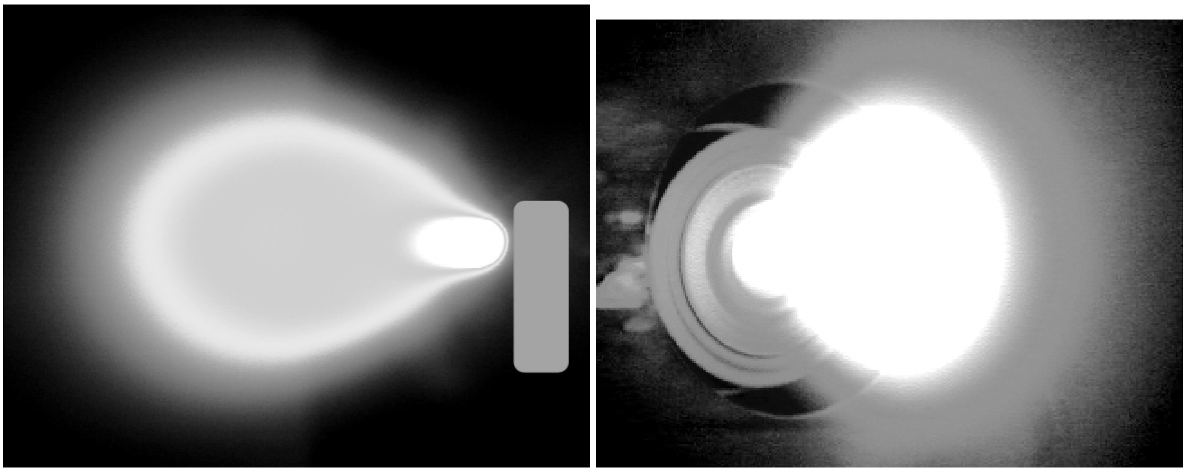

a) b)

Figure 2.2: Image of the plume: a) profile view. The brighter zone narrower and forward directed is visible close to the target, then the plume start the 3-D expansion, b) at the target surface the traces are visible, in form of circles, caused by the laser pulses.

example, green for the ablation of copper, silvery blue for iron rich compounds, and blue with red outer edges for the ablation of YBCO in oxygen.

Pressure gradients within the plume are greatest normal to the surface of the target so that the constituents of the plume have the greatest velocities in this direction. Time of flight studies of the plume just above the ablation threshold have recorded ionic velocities of order of 4 m/s, corresponding to energies in the 25-50 eV range.[94] This leads to the forward directional characteristic of the ablation process. Theoretical analysis predicts that, due to collisions within the plume, the velocities of species within the plume should display a mass dependence weaker than the thermal dependence (where velocity is inversely proportional to the square root of the mass) . The initial expansion of the plasma away from the target is one dimensional for a distance comparable with the laser spot diameter. In this dense region the plasma is heated by absorption of the laser beam to temperatures of several thousand degrees. Beyond this heating zone the plasma expands three dimensionally. At the involved temperatures, ionization due to collisions is expected to be negligible and so the laser beam must be the dominant source of ionization.

When the electron density in the plasma is less than a certain critical density, the plasma absorbs some of the incoming laser radiation, the critical density is higher the shorter the wavelength. Above the critical density there is strong reflection of the incoming radiation.[92] For long laser pulses a periodic process may occur in which the laser produces plasma which grows denser and hotter as the pulse continues, eventually shielding the target and thus suppressing plasma production; the density and temperature of the plasma just above the target decreases due to expansion and then the ablation continues. It has been suggested that absorption of the laser beam at the front of the plume may shield the target and the rear of the plume, allowing larger particles such as clusters to be stabilized.[92]

2.1.3 Deposition parameters

In a pulsed laser deposition system the adjustable parameters are: energy per laser pulse, pulses frequency, target substrate distance, substrate temperature, background gas pressure. The control of such parameters can be more or less critical for the quality of the film.

The energy of the laser pulse has to be high enough to induce ablation of the target but not so high to induce particle ejection, once the threshold for ablation passed, further increase of energy does not have significative effects on deposition rate. However, the effective power density at the target surface depend on the focalization of the beam, the optical path is thus a very important element of the deposition system.

Pulse frequency determine the deposition rate, a high deposition rate is desirable but can lead to a film full of structural defects. Defects can be avoided and crystallization improved if the time between laser pulses is equal to or greater than the time required for crystallization to occur.

The kinetic energy of the arriving species is controlled by the target substrate distance and by gas pressure. A big distance can have influence on the chemical uniformity as well, since segregation can occur within the plume if the travelling distance is enough.

The energy necessary to grow a film with a certain structure (amorphous, polycrystalline, epitaxial...) comes from both the kinetic energy of the incoming particles and the substrate temperature. The latter has to be adjusted depending on both deposited material and substrate, and is a parameter with the strongest influence on the crystallization of the film.

In the case of oxide thin films, an oxygen pressure, of the order of one mbar, is needed to avoid oxygen vacancies. Such pressure can be reduce by using a more reactive gas, like ozone. A high background pressure limits the expansion of the plume, reduces the kinetic energy of the flux, and concentrate the deposition on a smaller area.

2.1.4 SBN by PLD

An excimer laser is the usual energy source for ablation, 248nm wavelength (KrF) laser is more common than 193nm and 308nm. A Nd:YAG laser has been used as well.[57] In table 2.1.4 the deposition parameters from literature are summarized.

Epitaxial growth requires low deposition rates and actually better quality films on MgO have been obtained at 5Hz than at 10Hz pulse repetition rate . Oxygen pressure does not have a strong influence on crystallization, post annealing is always necessary to recover oxygen vacancies. The substrate temperature is in the interval $700 - 760°$ C, these values are common to other deposition techniques.

2.2 Deposition system

Two different deposition system where used to grow the films of this work. Both where equipped with an excimer laser: one with a KrF laser producing a beam with 248 nm wavelength, and the other with a ArF laser producing a beam with 193 nm wavelength. Pulse length is 20 ns in both cases.

As oxides have better absorption at wavelength longer than 200 nm, a 30% higher deposition rate and a brighter plume, is obtained with the KrF laser. No differences

Ref	wlngth	freq	pulse enrg. dens.	O_2	substrate	sub.temp
	nm	Hz	J/cm^2	$mbar$		$^\circ C$
[95]	193	1-10	0.5-1	3	STO	700
[65]	248	5	3	pulses	MgO	700
[96]	308	10	1.8	0.4-0.02	MgO	700-760
[55]	248	5	3.7	10^{-2}	MgO	675-700
[68]	248	7	1.5	0.026	LNO	775
[97]	248	5	3.8	10^{-1}	SBN	525- 760
[98]		50	3	0.0159	MgO	760
[59,99]	248	5-20	2.2	0.13	MgO	700
[62]	248	3-5	7	0.3-1	SiO_2	700
[56]	308	5	2.5		Pt/Si, SRO/Si	>720
[63]	248	5	3.2	0.2-0.8	MgO/Si	700
[61]	308	5	2.5		Si, Pt/Si	720

Table 2.1: Deposition parameters for SBN thin films obtained by PLD.

have been observed in the deposition process nor in the properties of the films obtained in the two different systems. The pulse repetition rate can be varied in the range 1 to 10 Hz with the energy per pulse in the range 100 to 600mJ.

A similar optical path for the laser beam, is common to both systems. The beam, produced by the laser with a section of $40 \times 30mm$, is deviated by 45° mirrors and focused on the target in a spot of about $5mm^2$. Then it enters the vacuum chamber trough a UV transparent window (Fig. 2.3). All the optical elements (mirror, lens, window) are made of UV graded fused silica, transparent in the wavelength range 185-2100 nm, the mirrors have a coating that assures 95% reflection at 45°. Because of the lens dimension (same of the beam), small misalignment of the mirror and residual absorption of the medium, about 30% of laser power is lost before the target.

The first deposition system (Fig. 2.4) was constructed as part of this thesis work. It consists of a vacuum chamber evacuated by a turbo molecular pump, the background

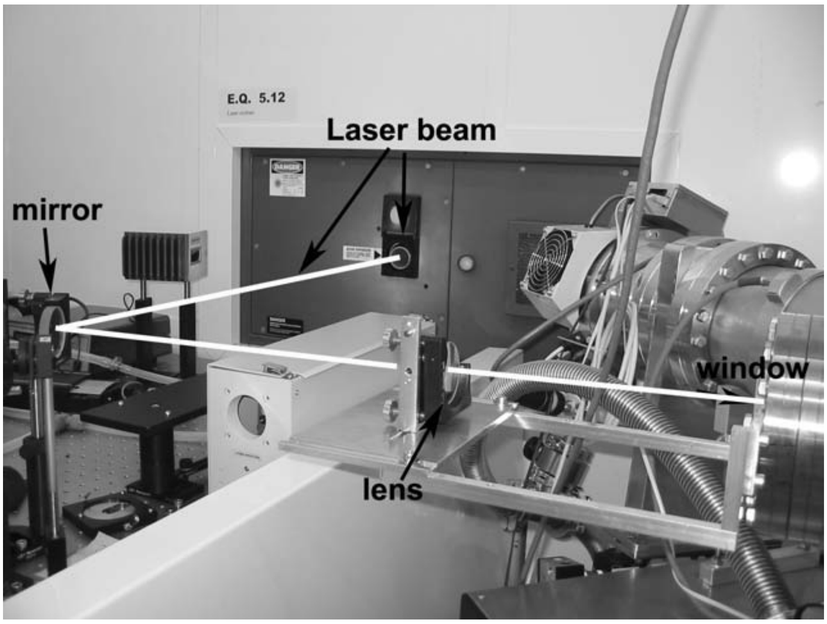

Figure 2.3: Laser beam optical path.

pressure before deposition is lower than 10^{-7} torr, suitable for deposition of oxides, is reached in two hours. Due to the relatively high deposition rate, typically a few Å per second, base pressure in the range $10^{-7} \div 10^{-8}$ are sufficient for PLD. At such pressure, contaminants from atmosphere arrive at the substrate with a rate of one to two orders of magnitude lower than the film deposition rate. A turbo-molecular pump is then a good choice since it avoids hydrocarbon contamination and allows for a fast evacuation of the chamber.

The chamber is vented with nitrogen each time a substrate or a target has to be introduced, than evacuation starts from ambient pressure. For this purpose, a system of butterfly valve allows a direct connection of the chamber with the backing pump. When the humidity level in the chamber is too high and deteriorates the vacuum, the chamber is baked. A system of heating tapes is installed for this purpose. Care has been taken for the temperature not to exceed 120°C where viton sealing is employed. During deposition the target undergoes a rotational movement assuring the exposure of a new portion of surface at each laser pulse and the uniform ablation of the whole target surface. As explained before, this procedure is essential in order to avoid pro-

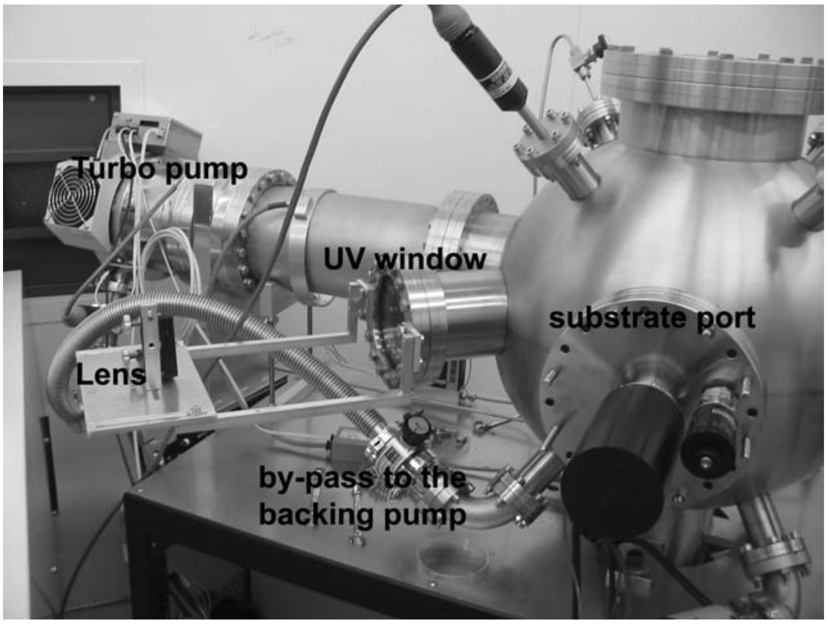

Figure 2.4: Picture of the homemade PLD deposition system.

duction of particles and incongruent ablation. After one hour of ablation of the target, erosion traces are well visible and the surface has to be polished then conditioned by a few hundred pulses prior starting deposition.

Substrates are glued to the heater with silver paint that assures a good thermal contact as well (Fig. 2.5). A difference of about 100°C has been found between glued and clamped substrate temperature (the latter being lower). The heater, as well as the target holder, is a commercially available one from Neocera. The heater is specifically designed to be oxygen compatible up to 950°C, a shutter provides the necessary protection during the pre-ablation of the target. We modified both target and substrate holder in order to fit our chamber, bigger than the standard. With such modification the target substrate distance can be adjusted from a minimum of 30mm to a maximum of about 200mm. An Eurotherm temperature controller is used to program heating and cooling ramps and to keep temperature constant during deposition.

A gate valve separate the chamber from the turbomolecular pump, it controls the pumping speed by varying the area of the aperture connecting the chamber and the pump. Oxygen can be introduced in the chamber and the pressure adjusted to the

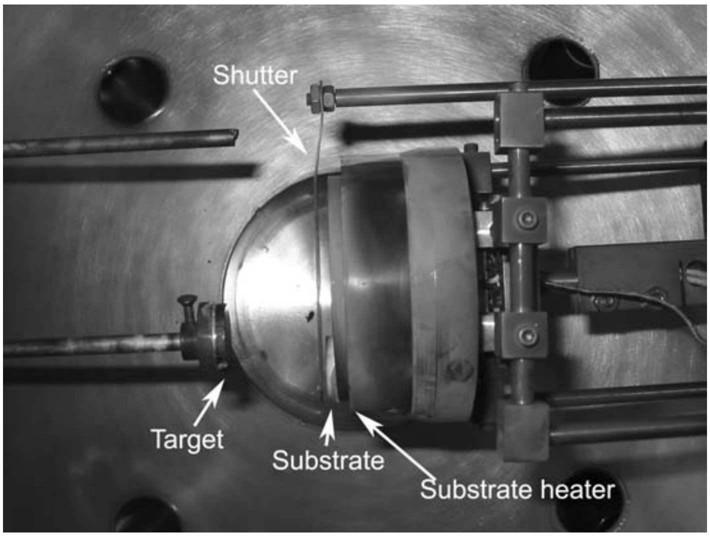

Figure 2.5: Pictures of the interior of the deposition chamber. The target is visible in front of the substrate heater, where a substrate is glued. The interposed shutter protects the substrate surface from contamination in the first phase of the deposition.

desired value in the range of 1 mtorr to 1torr, using a flux meter and a needle valve; the pressure being measured by a Baratron gauge.

A deposition rate of 4nm per minute is obtained at a target-substrate distance of 90mm, with thickness variation of ±25 nm over a $1cm^2$ area.

The second deposition system is a commercial multipurpose system with: a PLD chamber for thin film growth, AFM/STM chamber and XPS chamber. Each chamber is equipped with a turbo-molecular pump and communicates with a central one trough a gate valve. The central chamber serves as transfer and storage unit and is equipped with an ion-pump. Substrate and target as well as AFM/STM tips are introduced in the system trough a load-lock that reduces the pumping time and helps to preserve the ultra high vacuum necessary for STM measurements.

The PLD system is similar to the previously described one. It has in addition a RHEED facility to monitor the film growth in situ and make use of the KrF laser. The target undergoes a roto-translational movement that allows for a uniform ablation of the target and reduces damage of the surface. As a consequence the need to polish it is highly reduced. The substrates are glued or clamped on mobile substrate holders that can be transferred from the load-lock to any other chamber for processing and measurement, or stored in the central one. The heater of the PLD has a thermocouple on which the substrate holder is mounted for a better control of temperature. However a difference of about 50° C has been found between the temperature measured in the two system. The nominal growth temperature needed in this second system is higher.

2.3 Structural and compositional analysis

The formation of the TTB crystal structure for both ceramic and thin films has been verified by $\theta - 2\theta$ X-ray diffraction measurements with Cuα radiation. Thin film epitaxial growth and relation with the substrate is studied with X-ray diffraction pole figures and contact mode AFM topographic measurements. Details of grain growth, film-substrate interface and grain-grain interface where analyzed by TEM observations. Single crystal substrate surface has been characterized by contact mode AFM and reflection high energy electron diffraction (RHEED).
Stoichiometry of both target and films has been checked by X-Ray photoelectron spectroscopy (XPS), details on composition fluctuation in the films investigated by energy dispersive X-Ray analysis (EDX).

2.3.1 XPS basic principles

From a sample irradiated with X-rays of known energy, $h\nu$, core electrons of binding energy $E_b < h\nu$ are ejected. These electrons have a kinetic energy E_k which can be measured in the spectrometer and is given by:

$$E_k = h\nu - E_b - \Phi_{sp} \tag{2.1}$$

where Φ_{sp} is the spectrometer work function, the combination of the sample work function and the work function induce by the analyzer. Since we can compensate for the work function term electronically it can be eliminated, leaving:

$$E_k = h\nu - E_b \tag{2.2}$$

Thus the measured kinetic energy of the ejected electrons is used to calculate the binding energy of the electrons.

The surface sensitivity of electron spectroscopies is due to the low inelastic mean-free path, λ_m, of the electrons within the sample. For XPS, the main region of interest relates to electron energies from 100 to 1200eV, which give rise to a λ_m value of 0.5-2.0 nm. The actual escape depth of the photoelectrons depends on the direction in which they are traveling within the solid: electrons emitted perpendicular to the surface will arise from the maximum escape depth whereas electrons emitted nearly parallel to the surface will be purely from the outermost surface layers.

The essential components necessary for performing XPS consist of an X-ray source, an electron analyzer and an electron detector-multiplier, all maintained under ultra-high vacuum.

An XPS spectrum is generated by plotting the measured photoelectron intensity as a function of the binding energy. The resulting series of peaks, superimposed on a background caused by Bremstrahlung radiation, are characteristic for each element. The energies E_b are a direct representation of the atomic orbital energies. Binding energy variation due to chemical bonding with different elements produce what is called chemical shift, this way different oxidation states of an element can be identified by the presence of different peaks with a definite energy shift. Quantitative analysis of composition is performed by determining the area under the peaks and applying previously-determined sensitivity factors specific of each element or compound.[100]

2.3.2 Energy Dispersive X-Ray Spectrometry

When electrons interact with matter X-rays will be generated. If the energy of the incident electrons is high enough to eject inner shell electrons then characteristic energy loss electrons will be generated and characteristic x-rays will be emitted from the ionized atoms as an outer shell electron falls into the inner shell vacancy. A variety of characteristic energy X-ray is generated as the various displaced inner shell electrons are replaced by the various outer shell electrons. The relative probability of generating X-ray of the various possible energies from a given element is controlled by the incident electron energy and by the number of different possible way by which the ionized atom can return to its ground state. The ionization cross section for any event is given by empirical equations that give good agreement for the characteristic emission of any element. Energy dispersive X-Ray spectrometers can be built in electron microscopes, X-ray are generated by the incident electron beam within a volume similar to that for the transmitted electrons. Peaks at energies characteristic of the elements within that volume can be identified and the concentration can be calculated. Thus the composition of the sample and eventual fluctuation can be determined for comparison with the image coming from the transmitted electrons.[101]

2.3.3 RHEED

Investigation of periodic structures by diffraction technique (X-rays or electrons) give information about symmetry in the reciprocal lattice. The pattern formed by the diffracted beams can be explained in terms of conservation of energy and momentum plus a reciprocal lattice vector. The condition to have diffraction are expressed by the Bragg' law. For a three dimensional system the reciprocal lattice vectors have three components and specify a point in the reciprocal lattice. The generated diffraction patterns of a 3-D periodic structure is then constituted by spots, as in the case of Transmission Electron Microscopy.

A graphical representation of the diffraction condition in the reciprocal lattice is the Ewald sphere construction. Given a reciprocal lattice, a vector $\mathbf{k}$, equal to the incident radiation wave vector, is drawn to terminate at the origin of the reciprocal lattice. A sphere is constructed about the beginning of the vector $\mathbf{k}$ with radius k. For any point at which this sphere passes trough a reciprocal lattice point, a line to this point from the centre of the sphere represents a diffracted beam. For diffraction process involving

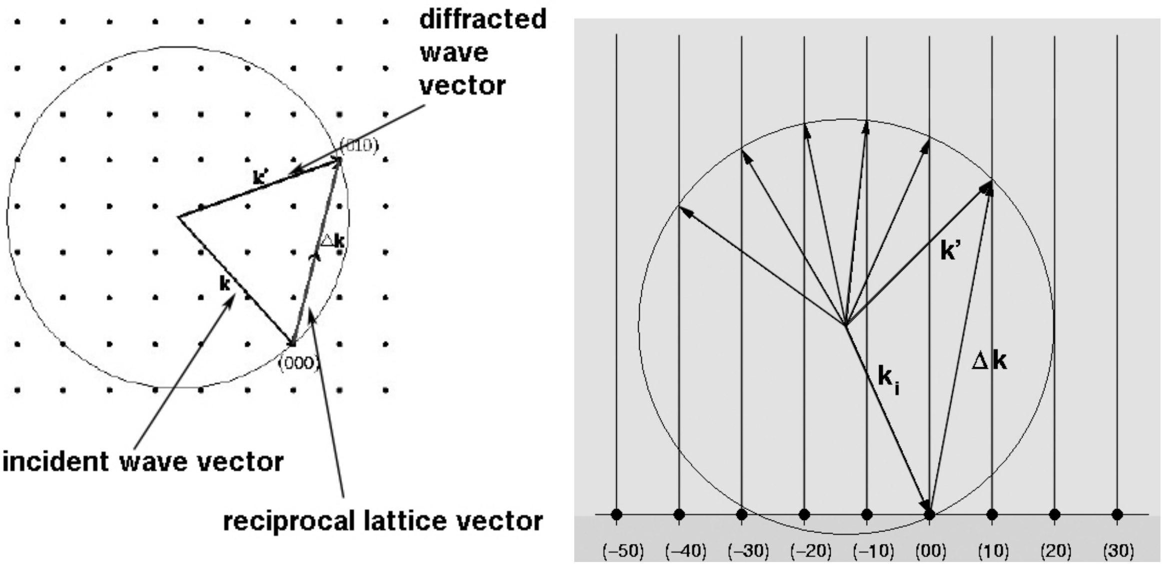

a) b)

Figure 2.6: Ewald construction for diffraction experiments for: a)bulk sensitivity, b) surface sensitivity. In the first case the reciprocal lattice is constituted by points, in the second by rods. In both cases diffraction occurs for the reciprocal lattice elements crossed by the Ewald sphere.

only the surface, i.e. a two dimensionally periodic system, only the parallel to the surface components of the wave vector are conserved, thus the reciprocal lattice vectors have two components and specify a line. The Ewald sphere is constructed the same way and diffraction occurs for each crossed line.
Surface sensitivity of high energy electrons, i.e. low penetration in the sample, is obtained in RHEED technique by using grazing incidence. Because of the high energy of the incident radiation, the wave vector is big and so is the Ewald sphere radius compared to the spacing of the reciprocal lattice rods, the surface of such a wide sphere crosses the rods not in a point but rather in a segment. The resulting diffraction pattern is than constituted by strikes.

In a RHEED diffractometer a magnetically focused electron beam, of 5 to 30 keV, is directed at a glancing angle of about 1° at a single crystal in high vacuum. Diffracted electrons fall on a phosphor screen opposite to the electron source giving a typically streaked pattern.

If the surface is rough, transmission rather than reflection patterns are obtained. Due to the surface roughness, the beam can enter and diffract at 3-dimensional structures such as islands, steps, and ridges, and the streaks are replaced by points as in case of a 3d crystal reciprocal lattice. Roughness of order of an atomic layer can be detected.[100,102]

In epitaxial thin film growth, RHEED serves in a first step to analyze the growth substrate. The occurrence of a clear diffraction image (strikes or points) confirms the crystallinity of the surface. The information about strikes or point shapes tells in addition whether the surface is rough or flat. During growth of the film, RHEED allows to analyze film crystallinity, two or three-dimensional growth, and lattice parameters. In two-dimensional growth it can be used to control the number of deposited layers.

Chapter 3

Growth and structural characterization of SBN thin films on silicon based substrates

In this work ferroelectric thin films were grown on conductive substrates to fabricate parallel plate capacitors. In order to fully profit from the ferroelectric properties in such a configuration it is convenient to have the ferroelectric polarization axis perpendicular to the film plane. In the case of a uniaxial tetragonal material like SBN this means to grow the film with the polar (001) axis perpendicular to the film plane. For optimal properties, phase purity, density and surface smoothness of the film are properties of concern.

3.1 Targets

Ceramic targets of SBN50 were prepared by the conventional sintering method. High purity powders ($> 99.999\%$) of strontium and barium carbonate were mixed with niobium pentoxide in stoichiometric ratio. After 24h wet ball-milling in acetone with zirconia balls, the powders where dried and calcinated at 1100°C for 6h. The XRD measurements showed that, during calcination, a reaction took place and the powder was pure tetragonal tungsten bronze phase.

The SBN powder has been sieved through a mesh of 100 μm then pressed into pellets and sintered at 1350°C for 24h. The obtained ceramic showed an abnormal growth of grains up to 1mm. This material is too brittle to be ablated without production of particles that would strongly affect the film quality. The phenomenon of grain growth is documented in literature and arises from high calcination temperatures that are required for preparation through conventional solid-state reaction of the reactants.[103, 104] Direct sintering of the mixed powders (skipping the calcination step) at 1350°C results in a ceramic with smaller grains of more homogeneous size. The density was 90% of the theoretical value (5.368 $\frac{g}{cm^3}$). The X-ray diffraction spectrum is in accordance with the standard data for TTB structure (Fig. 3.1).

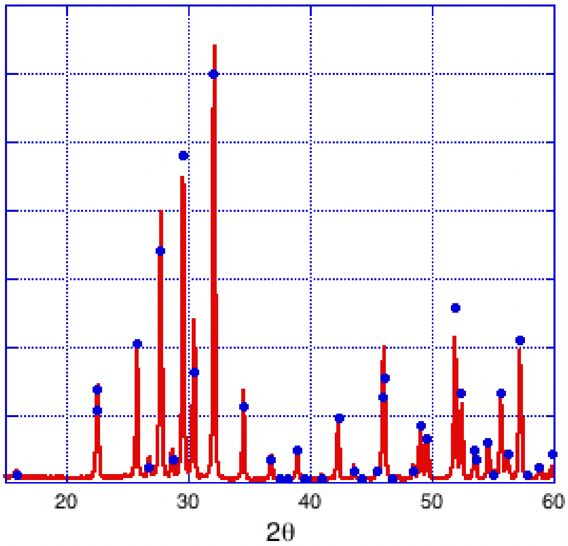

Figure 3.1: X-ray diffraction pattern of SBN50 ceramic target obtained by direct sintering: the dots represent the standard values

3.2 Effect of growth parameters on phase purity, crystalline orientation, and strain

SBN films have been deposited on SiO_2/Si, $Pt/SiO_2/Si$, $Ir/SiO_2/Si$, $IrO/SiO_2/Si$ and $SrTiO_3$ substrates. Deposition parameters were adjusted for each of them. The growth on $SrTiO_3$ single crystal substrates will be discussed in a dedicated chapter.

The SBN film grows crystalline on SiO_2/Si at $700°C$. An oxygen pressure of 10^{-2}mbar is necessary for a crystalline growth, at 10^{-3}mbar the resulting film is amorphous (Fig.3.2), in crystalline form the film is strongly (001) oriented (Fig.3.3b)). Increasing the deposition temperature to 750°C yields the appearance of peaks at 28.8° and 29.7° which do not belong to the TTB structure (Fig.3.4). The establishment of (001) orientation on amorphous SiO_2 indicates that (001) is the natural growth facet and thin film orientation in absence of dominating interface energies.

Growth on Si(100) single crystal substrates gives results similar to those on SiO_2/Si. This was expected as an interlayer of SiO_2 is most likely to form during deposition in a reactive oxygen atmosphere(Fig.3.5. See later in the chapter for detailed analysis of the SBN/Si interface).

Crystallization of SBN on $Pt/SiO_2/Si$ (Fig.3.6) is obtained at 720°C (at 700°C the layer is amorphous, Fig.3.3). Increasing the deposition temperature to 740°C gives a (001) oriented film.

Even though Ir thin films have the same structure and lattice parameters as Pt thin films, SBN grown on $Ir/SiO_2/Si$ was never oriented, independently from the substrate temperature and the oxygen pressure during deposition. The same result has been obtained from SBN grown on $IrO/SiO_2/Si$. Therefore, we conclude that the Ir surface oxidizes at temperature and oxygen pressure used in processing(Figs.3.7,3.8). IrO_2 has a rutile structure, XRD of SBN/Ir sampled do not show the corresponding diffraction peaks, modification of Ir should be limited to a thin surface layer.

At $750°C$ Ir has a higher oxygen affinity compared to Pt, the bonding strength with SBN is stronger in this case and influences the film growth. Because of the chemical stability of (111) oriented Pt, on such a substrate SBN is free to follow it natural growth along $< 001 >$ direction (see the literature on single crystal growth[16]). Pt does not oxidize, moreover it bonds only weakly to oxides. As a consequence, interface energy is weak. In addition there is no obvious orientation of SBN to fit the hexagonal surface of Pt(111).

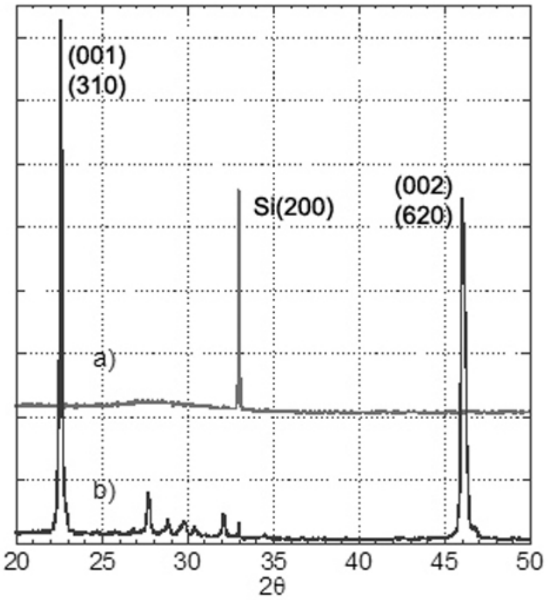

Figure 3.2: XRD $\theta-2\theta$ diffractions from SBN50 deposited at 750°C 250 mJ 10Hz on SiO_2/Si substrates with oxygen pressure: a)10^{-3} mbar and b)10^{-2} mbar. 10^{-2} mbar of oxygen are necessary to crystallize the film.

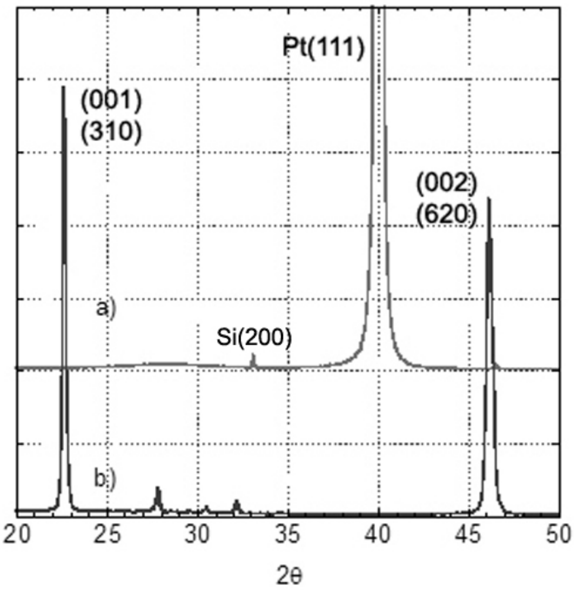

Figure 3.3: XRD $\theta-2\theta$ diffractions from SBN50 deposited at 700°C with 10^{-2} mbar of oxygen 250 mJ 10Hz, on a)$Pt/Ti/SiO_2$ and b)SiO_2/Si substrates. While in the case Pt/SiO_2 this temperature is not enough for SBN to crystallize, the deposition on SiO_2 is well crystallized and preferentially oriented (001).

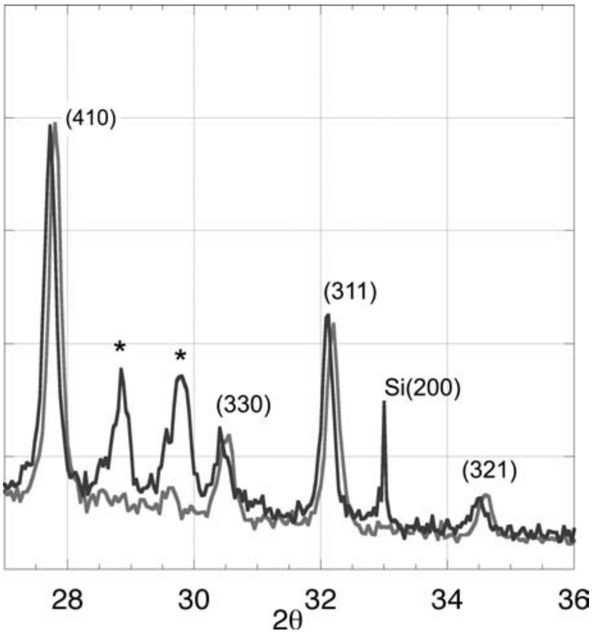

Figure 3.4: XRD $\theta - 2\theta$ diffractions from SBN50/SiO$_2$ deposited at 700°C and 750°C: at 750°C two peaks (indicated with $*$) appear that can not be attributed to the TTB structure.

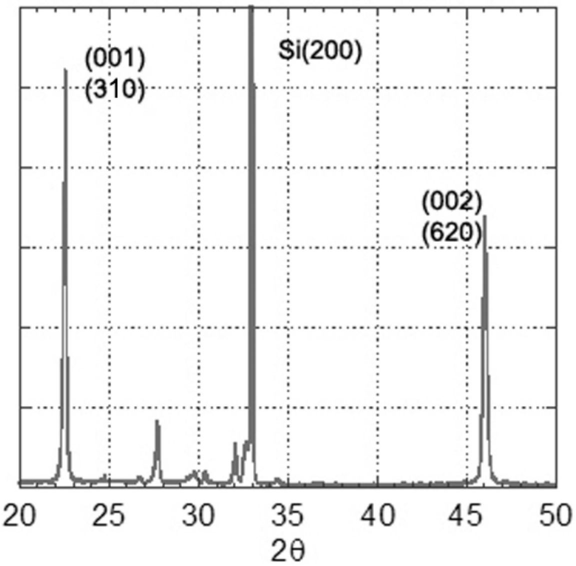

Figure 3.5: XRD $\theta - 2\theta$ diffractions from SBN50 deposited at 740°C 250 mJ 10Hz and oxygen pressure 10^{-2} mbar on Si(100) substrate. The result is the same as found for deposition on SiO$_2$.

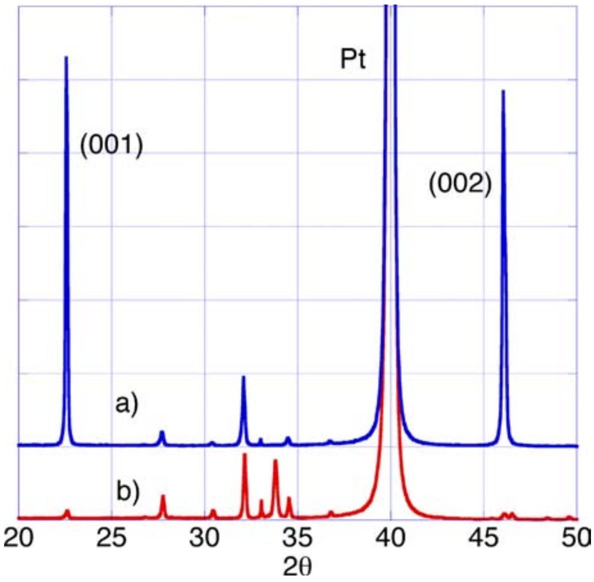

Figure 3.6: XRD $\theta - 2\theta$ diffractions from SBN50 deposited at 250 mJ 10Hz and oxygen pressure 10^{-2} mbar on Pt/SiO_2/Si substrate: a)740°C, at this temperature the film is (001) oriented, b) 720°C, at this temperature the film start to crystallize but no preferential orientation is observed.

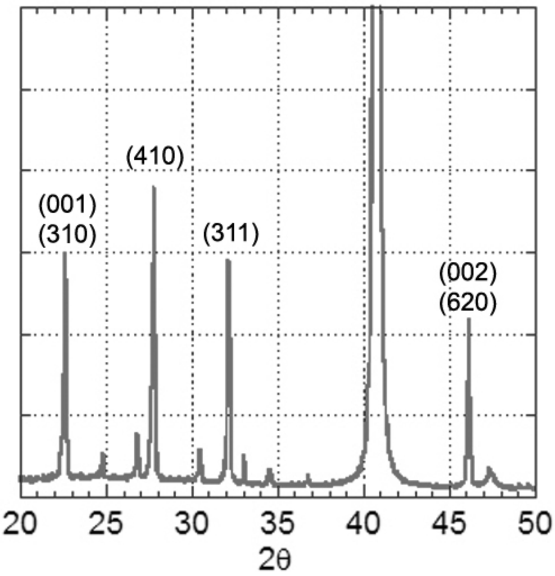

Figure 3.7: XRD $\theta - 2\theta$ diffractions from SBN50 deposited at 740°C 250 mJ 10Hz and oxygen pressure 10^{-2} mbar on Ir/SiO$_2$/Si substrate. No preferential orientation was obtained on this substrate.

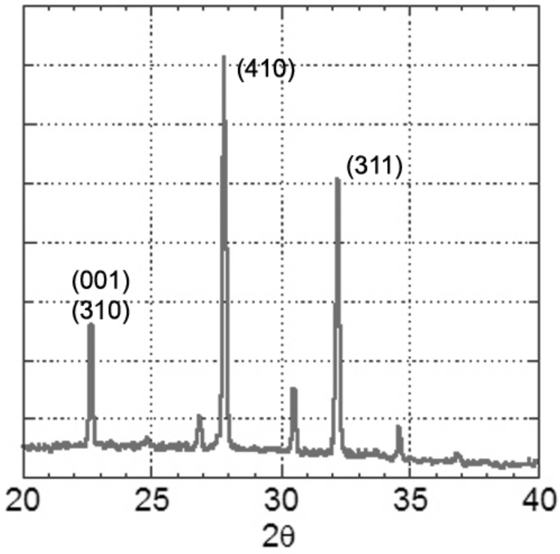

Figure 3.8: SBN50 deposited at 740°C 250 mJ 10Hz and oxygen pressure 10^{-2} mbar on $IrO_2/SiO_2/Si$ substrate. The film obtained has the same X ray spectrum of SBN grown on Ir films suggesting that the Ir surface actually oxidizes during deposition.

The energy per laser pulse does not influence the quality of the deposition. Below 200 mJ, the plume becomes too small and unstable, while above 400 mJ the laser gas lifetime is drastically diminished. Therefore, the working energies have been chosen in the interval 200-400 mJ.

The target-substrate distance has been varied in the range 50-90mm. Thickness uniformity is strongly influenced by the distance and revealed by variation of film color with thickness. With target-substrate distance of 85mm and average thickness of 500nm, a variation of ± 50nm on a surface of $1cm^2$ has been measured. Deposition rate is proportional to the pulse repetition rate and, at 85mm target substrate distance, a rate of 0.5nm/pulse is obtained.

The film quality strongly depends on the substrate-plume distance more than on the absolute distance from the substrate to the target. The plume dimension depends on the background pressure of oxygen. If the substrate is too close to the plume edge, the film contains unidentified second phases. With increasing distance, pure TTB phase is obtained.

After deposition, the film is cooled to room temperature at a rate inferior to 7.5°C/min in 1torr of oxygen. Annealing in oxygen reduces oxygen vacancy concentration and will be discussed in the chapter on dielectric properties.

In summary, the laser parameters and the substrate-target distance have a slight influence on the SBN growth. Once the substrate temperature, oxygen pressure and distance from the plume to the substrate are in the appropriate range for the formation of the TTB structure, it is possible to play with them in order to have a higher deposition rate or a greater uniformity in the film thickness. On the contrary, the substrate temperature plays a leading role in the film growth. After arrival on the substrate, a certain mobility is necessary for the deposited atoms to organize in the TTB structure. The existence of a threshold temperature to grow film with a well defined crystalline structure clearly suggests that this mobility is provided by the substrate temperature rather than by kinetic energy of the plasma plume. This is well understandable given the large diffusion distance needed to establish one unit cell and the short hopping distance due to kinetic energy, which is not more than two next neighbor distances on average. The large unit cell leads, in addition, to a considerable activation energy G^* for nucleation. Only thermal energy helps to overcome the Boltzman factor $\exp(-G^*/kT)$.

All the X-ray diffraction patterns show peaks shifted by about 0.1° toward higher values, corresponding to a out-of plane strain S_3 of 0.5%, and indicating a positive strain acting in the film plane. The thermal expansion mismatch indeed leads to a tensile stress in the film. Such a strain, S_3, is calculated as:

$$S_3 = -(c_{13}/c_{33})(S_1 + S_2) \tag{3.1}$$

$$S_1 = S_2 = (\alpha_{SBN} - \alpha_{Si})\Delta T \tag{3.2}$$

where S_1 and S_2 are the in-plane strain along the SBN a and b axis, α_{SBN} and $\alpha_{Si}$the thermal expansion, c_{13} and c_{33} the elastic stiffness of SBN (see Tab.3.1). In-plane tensile strain of about 0.6% have been calculated considering the difference in thermal expansion of SBN and Si (see sec.5.2.2.4), this correspond to a out of plane strain of

α_{SBN}	$15 \cdot 10^{-6} K^{-1}$
α_{Si}	$3 \cdot 10^{-6} K^{-1}$
c_{13}	$0.355 \diamond 10^{11} Nm^-2$
c_{33}	$1.166 \diamond 10^{11} Nm^-2$

Table 3.1: Parameters used to calculate the strain in the SBN films in eq.3.2.

about 0.4%. A variation in stoichiometry cannot account the large strain observed. S_1 changes only by 0.3% for a 25% error in composition. In the next section it will be shown that the composition is quite correct. The films were always found free from particles, independently of the deposition parameters. This favorable condition has to be attributed to the high density of the target and to the low thermal conductivity of the material itself.

Substrate temperature	$> 720°$
Oxygen pressure	$> 10^{-2} mbar$
Target substrate distance	50-90mm with 0.2mbar of oxygen
Energy per laser pulse	200-400mJ
Laser pulse repetition rate	1-10 Hz

Table 3.2: Deposition parameters for SBN thin films.

3.3 SBN50 grown on Pt/Ta

Platinum bottom electrodes for SBN deposition were prepared by sputtering on SiO_2/Si wafers. 100 nm thick, (111) oriented films, are obtained at a temperature of 500°C with the use of different buffer layer. SBN films grown on Pt present the major problem of Pt film adhesion to the silicon substrate. The stability issue of metallic layers on SiO_2/Si is well known and different materials have been studied for their adhesion properties, Ti Ta and Zr being the most common in the case of Pt.[105,106] Often atoms migration and compound formation are associated with decreased Pt adhesion to the substrate. Among the different adhesion promoting procedures is the oxidation of the metal used as adhesion layer.

In our case the deposition temperature needed to obtain (001) oriented SBN (700°C) lead to the peel-off of 100nm thick Pt electrode, sputtered on Si/SiO_2 substrate using TiO_2 as adhesion layer. Better adhesion has been obtained in the case of Pt/Ta on SiN. Perfectly oriented SBN grows if, in the substrate processing, an annealing step at 700°C in oxygen is introduced after deposition of the first 50nm of Pt (see Fig:3.9).

Energy dispersive X-ray (EDX) analysis of the cross section of such processed Pt electrodes, after SBN deposition at 740°C, shows Ta diffusion trough the Pt layer (Fig. 3.10 spectra 1 to 3 and 5 to7). The interface with SBN is irregular and inter-diffusion with the electrode occurs (Fig. 3.11, cf. spectra 1 and 4). Despite good adhesion behavior, the roughness of the SBN/Pt interface indicates that the SBN deposition process is damaging the electrode.

The SBN50 film is dense and constituted of columnar grains running through the film. Oblique grain boundaries and irregular growth was observed where Pt, Ta and SBN interdiffuse, Fig. 3.12.

The EDX measurement shows that Pt and Ta diffuse at most 10nm in to the SBN50, forming an amorphous phase. The film composition is richer in Ba than Sr while Nb content is consistent with TTB structure, fluctuation are present both perpendicularly and along the film plane. Sr seems to accumulate in the amorphous layer at the interface with the electrode where the ratio Sr/Ba is measured to be 1.69 while in the film it varies from 0.5 to 0.75. Nb fluctuation are much smaller, the ratio (Sr+Ba)/Nb varies from 0.3 to 0.45 (Fig.3.13).

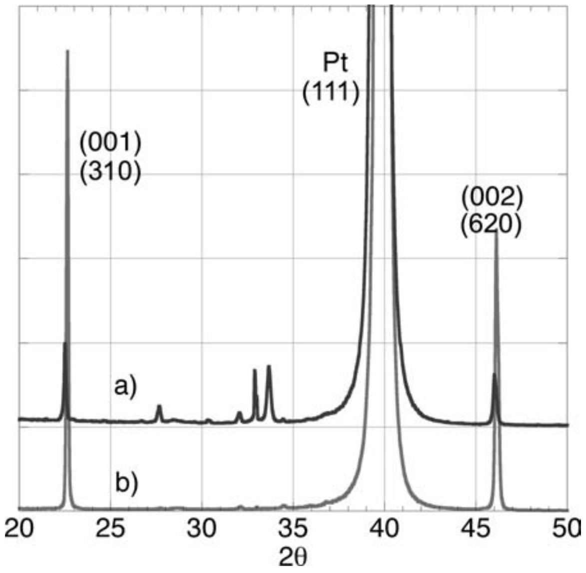

Figure 3.9: XRD $\theta-2\theta$ diffractions from SBN50 deposited at 740°C 250 mJ 10Hz and oxygen pressure 10^{-2} mbar on: a) Pt/Ta/SiO_2/Si, b)$Pt/Ta/SiO_2/Si$ annealed in oxygen (700°C) as intermediate step during the deposition of the Pt layer.

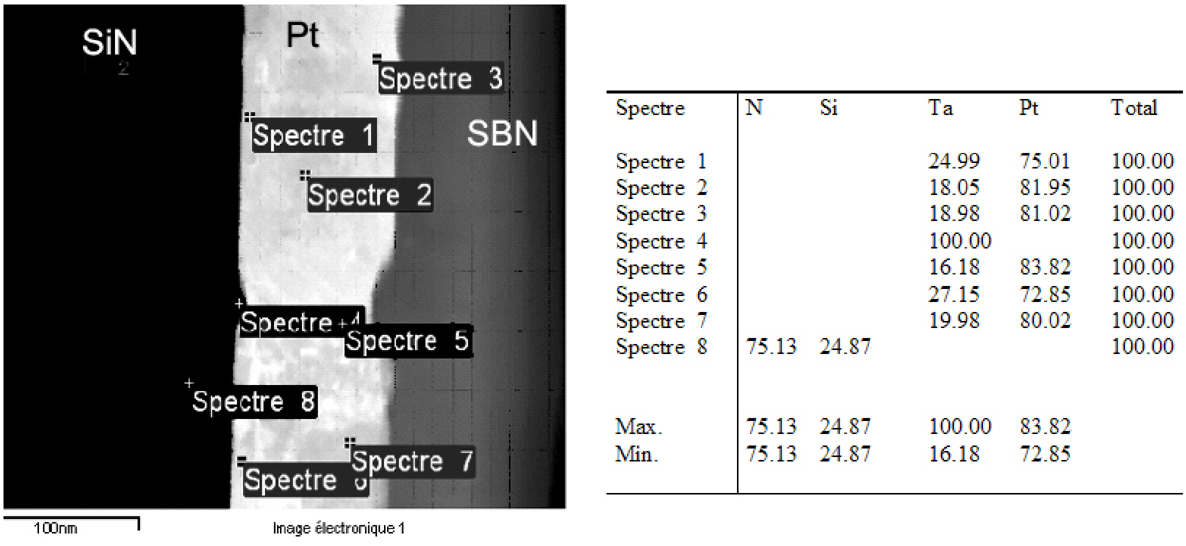

Spectre	N	Si	Ta	Pt	Total
Spectre 1			24.99	75.01	100.00
Spectre 2			18.05	81.95	100.00
Spectre 3			18.98	81.02	100.00
Spectre 4			100.00		100.00
Spectre 5			16.18	83.82	100.00
Spectre 6			27.15	72.85	100.00
Spectre 7			19.98	80.02	100.00
Spectre 8	75.13	24.87			100.00
Max.	75.13	24.87	100.00	83.82	
Min.	75.13	24.87	16.18	72.85	

a) b)

Figure 3.10: Cross section TEM micrograph and chemical analysis (EDX) of oxidized Pt/Ta grown on SiN. Ta is diffusing trough the whole Pt layer up to the surface, irregularities are visible at the interface with SiN.

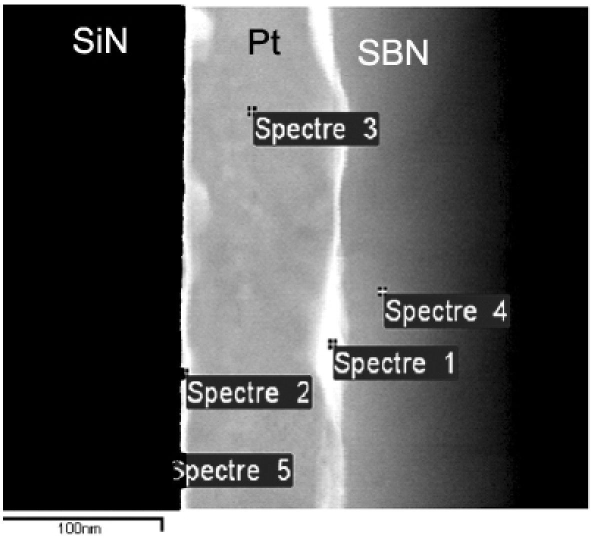

a)

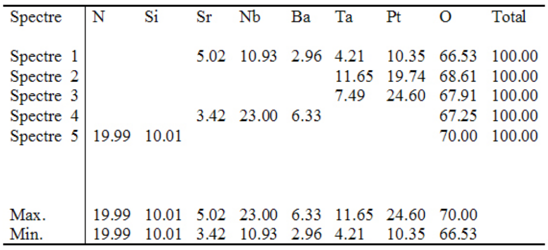

Spectre	N	Si	Sr	Nb	Ba	Ta	Pt	O	Total
Spectre 1			5.02	10.93	2.96	4.21	10.35	66.53	100.00
Spectre 2						11.65	19.74	68.61	100.00
Spectre 3						7.49	24.60	67.91	100.00
Spectre 4			3.42	23.00	6.33			67.25	100.00
Spectre 5	19.99	10.01						70.00	100.00
Max.	19.99	10.01	5.02	23.00	6.33	11.65	24.60	70.00	
Min.	19.99	10.01	3.42	10.93	2.96	4.21	10.35	66.53	

b)

Figure 3.11: Cross section TEM micrograph and chemical analysis (EDX) of oxidized Ta-Pt grown on SiN and the interface with the SBN film. Here, in the first layer, about 10nm thick, Pt and Ta are diffused into the SBN film (spectrum 1). At larger distance from the substrate the SBN is not contaminated any more.

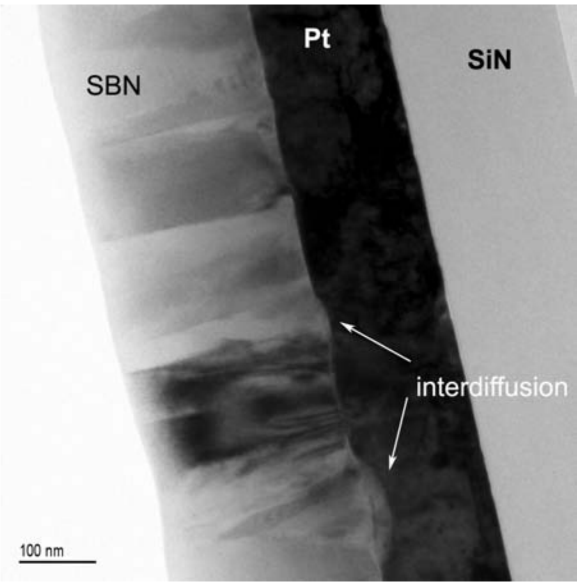

Figure 3.12: Cross-section TEM micrograph of SBN grown on oxidized Pt/Ta/SiN. The film grows mostly in columns perpendicular to the substrate but, where there are defects in the platinum layer, the growth is disturbed. Where interdiffusion zones are formed at the interface, the SBN grains grow with a different morphology . This suggest that there is a different growth mode taking place in the interdiffusion zones.

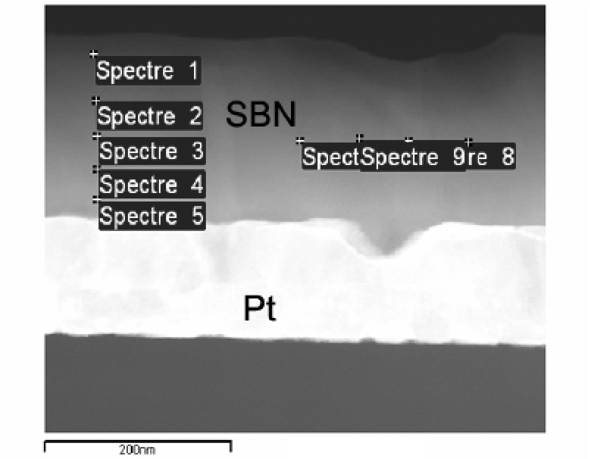

a)

Spectre	Sr	Nb	Ba	O	Total
Spectre 1	2.48	24.76	4.20	68.57	100.00
Spectre 2	3.70	23.26	5.60	67.44	100.00
Spectre 3	3.96	22.93	5.90	67.20	100.00
Spectre 4	4.45	22.63	5.95	66.98	100.00
Spectre 5	4.31	22.82	5.75	67.12	100.00
Spectre 6	4.26	23.02	5.46	67.26	100.00
Spectre 7	3.46	23.39	5.61	67.54	100.00
Spectre 8	3.15	23.48	5.76	67.61	100.00
Spectre 9	2.92	23.55	5.86	67.66	100.00
Max.	4.45	24.76	5.95	68.57	
Min.	2.48	22.63	4.20	66.98	

b)

Figure 3.13: Cross section TEM micrograph and chemical analysis of SBN grown on oxidized Ta-Pt electrode. SBN composition is not uniform and the interface is richer in Sr.

3.4 SBN50 grown on Si(100)

A substrate of (001) oriented Si is treated in HF 1% diluted in demineralized water for 1 min in order to remove the native oxide. After this treatment the substrate is rinsed in demineralized water, dried with nitrogen and promptly introduced in the vacuum chamber where the pressure reaches 10^{-6} torr in few minutes. To minimize the formation of SiO_2 at the Si-SBN interface, the temperature was increased to 720° in vacuum. Deposition started with a few laser pulse without oxygen and then continued in 10^{-2} torr of oxygen.

The obtained film is polycrystalline, (001) preferentially oriented (Fig.3.5). TEM images reveal a dense columnar structure running trough the film cross-section (Fig. 3.14) growing on an amorphous 5nm thick layer at the interface Si-SBN (Figs. 3.14, 3.15, 3.16). Such a layer has a sharp interface with both substrate and film and is most probably due to diffusion of oxygen into the substrate. EDX chemical analysis (Fig.3.17) reveal that the layer is rich in Si and Nb, the content of oxygen is extrapolated from charge balancing.

The formation enthalpy for the relevant oxides are reported in table 3.3. The accumulation of Nb at the interface is caused by the high enthalpy value corresponding to Nb oxide (twice the value for Si dioxide). At the same time we can suppose the formation of Nb oxide rather than NbSi, possible as well. We conclude that the first layers deposited in high vacuum, do not constitute a valid barrier to the diffusion of oxygen into the silicon substrate.

The film growing on the amorphous interface is stoichiometric and the small fluctuation in composition are compatible with the measurement error evaluate in 1% (Fig.3.18).

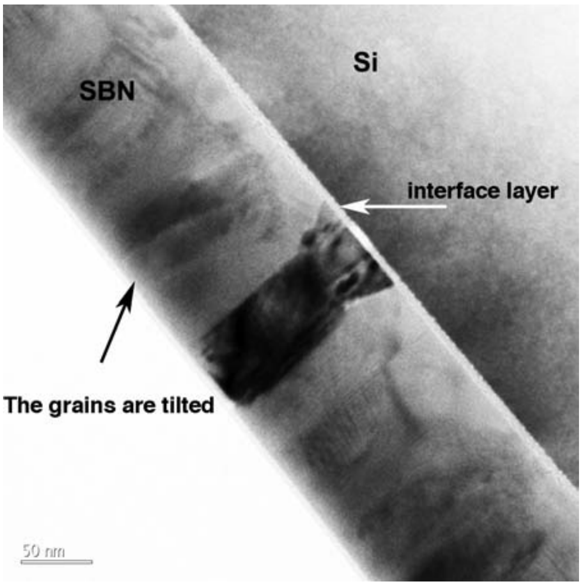

Figure 3.14: TEM cross-section micrograph of SBN grown on (100)Si. An interface layer is visible between the silicon substrate and he SBN film. The grains are growing inclined with respect to the plane normal and a certain degree of disorder is visible in the first 20 nm.

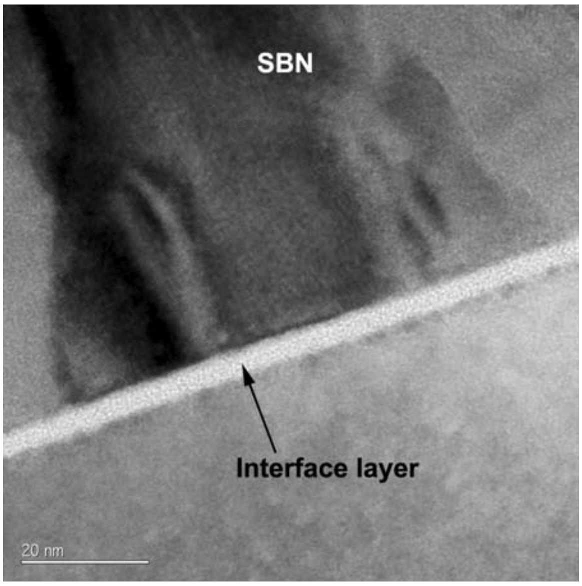

Figure 3.15: Detail of the previous picture clearly showing the presence of the interface layer between substrate and SBN film.

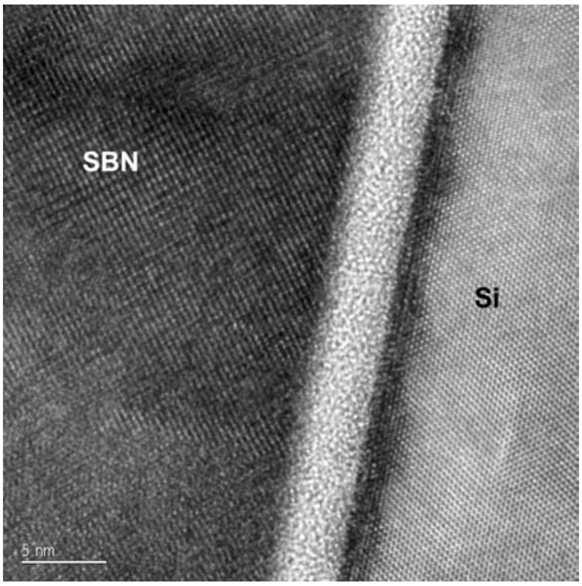

Figure 3.16: High resolution TEM image of SBN grown on Si(100): the 5 nm thick interface layer is amorphous.

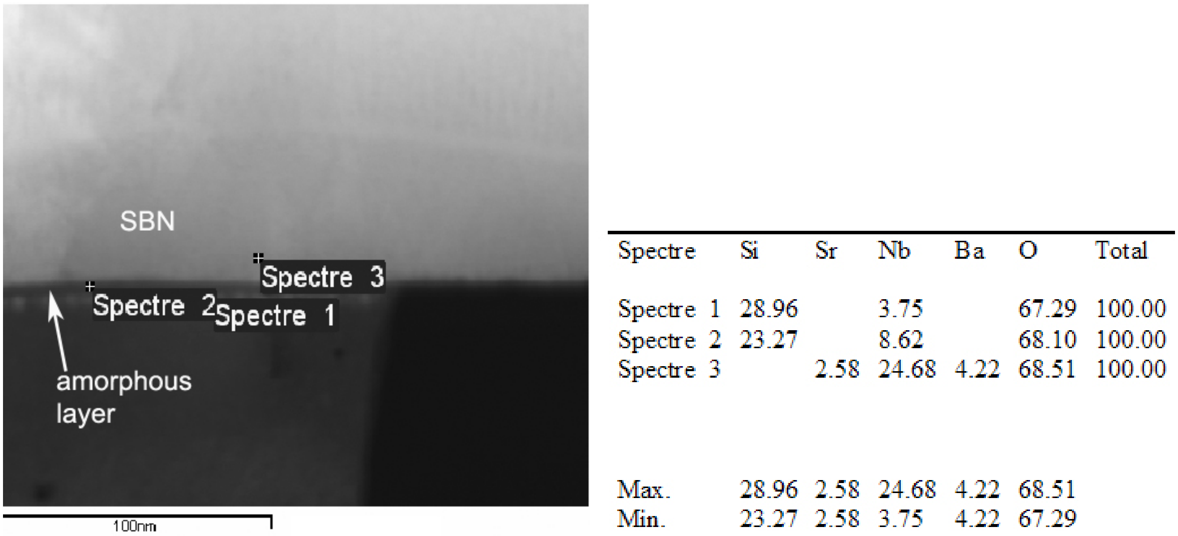

Spectre	Si	Sr	Nb	Ba	O	Total
Spectre 1	28.96		3.75		67.29	100.00
Spectre 2	23.27		8.62		68.10	100.00
Spectre 3		2.58	24.68	4.22	68.51	100.00
Max.	28.96	2.58	24.68	4.22	68.51	
Min.	23.27	2.58	3.75	4.22	67.29	

a) b)

Figure 3.17: TEM image and composition of the amorphous interlayer.

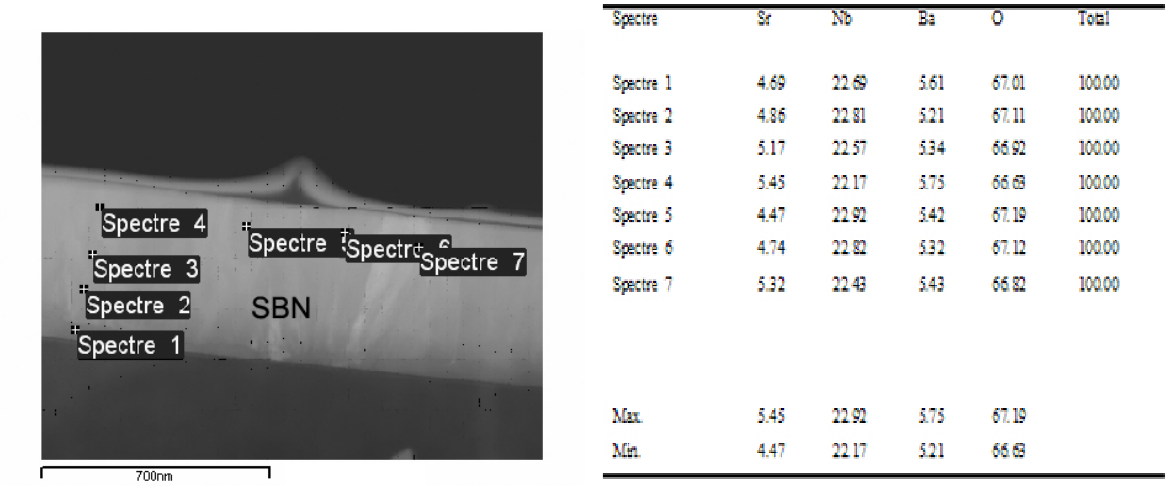

Spectre	Sr	Nb	Ba	O	Total
Spectre 1	4.69	22.69	5.61	67.01	100.00
Spectre 2	4.86	22.81	5.21	67.11	100.00
Spectre 3	5.17	22.57	5.34	66.92	100.00
Spectre 4	5.45	22.17	5.75	66.63	100.00
Spectre 5	4.47	22.92	5.42	67.19	100.00
Spectre 6	4.74	22.82	5.32	67.12	100.00
Spectre 7	5.32	22.43	5.43	66.82	100.00
Max.	5.45	22.92	5.75	67.19	
Min.	4.47	22.17	5.21	66.63	

a) b)

Figure 3.18: TEM image and composition (by EDX) of SBN film deposited on Si substrate.

	$\Delta H/O$
BaO	-992.1
SrO	-592
Nb_2O_5	-758.9
SiO_2	-455.5

Table 3.3: Enthalpy of formation of oxides

3.5 Conclusion

The TTB is a very complex structure. High substrate temperature, over the threshold value of $720°C$, is necessary for the impinging species to crystallize in such a structure. The other requirement is the presence of enough oxygen, at least $10^{-2} mbar$, in the deposition atmosphere.

At the deposition temperature, adhesion of Pt electrode to the SiO_2 substrate is a serious problem, only partially solved by a oxygen annealed Ta/SiN adhesion layer. The annealing step, introduced in the Pt electrode processing, improves Pt adhesion. A further Pt layer has to be deposited in order to have a clean surface for (001) orientation of SBN. Ir electrode is mechanically stable at such temperature but react with oxygen. Such a reactivity induce a strong bonding with SBN, the film growth is influenced and (001) orientation could not be attained. Amorphous, like $\mathrm{SiO_2}$, or chemically inert, like Pt, substrates do not influence the film growth. On this condition SBN is free to follow its natural crystal growth along the $< 001 >$ direction. SBN grown directly on Si single crystals, is accompanied by the formation of an amorphous oxide layer of about 5nm. The shift of X-ray peaks reveals a thermal strain of 0.8% in the plane of the film. This value is quite independent of the growth substrate (Pt, $\mathrm{SiO_2}$, Si) but depends mostly on the thermal mismatch with the silicon wafer. EDX analysis confirms a good 1:1 composition transfer from target to film.

Chapter 4

SBN on single crystal STO substrates: epitaxial growth

4.1 Epitaxial growth

Epitaxial growth is a specific type of film growth where a preferred orientation relationship exists between the film and substrate even if their crystal structures are different. These relationships are due to the existence of orientations with a low interfacial energy. Two important factors determining the interfacial energy are lattice mismatch and strength of chemical bonding between film and substrate atoms.[107] For sufficiently large bonding strength and sufficiently small misfit, the first mono layers of the deposited film adopt the periodicity of the substrate. The film is strained by the following value known as misfit strain:[108–110]

$$m = \frac{a_s - a_f}{a_f}$$

where a_f and a_s are the unstrained atomic spacing of film and substrate along some direction relevant in the epitaxial geometry considered. The tendency for epitaxial growth increases with decreasing misfit but this is not a sufficient condition. Strong bonding with the substrate induces epitaxy unless the misfit is so large that creation of the film crystal structure is impossible even with the introduction of dislocations. The misfit strain results in an elastic energy in the film, which increases proportional

to the film thickness. Above a critical thickness dislocations are introduced to release this elastic stress (see sect. 4.1.1).
In the equilibrium theory of epitaxial growth, three growth modes are traditionally distinguished:[111]

- layer by layer, where each atomic layer is completed before the next is started (Frank-van der Merve[112]).
- three dimensional or islands formation[113](Volmer-Weber).
- a combination of the previous, beginning layer by layer and changing to islands after a few layers[114](Stranski-Krastanov).

The particular growth mode for a given system depends on the interface energies and on the lattice mismatch. In lattice-matched systems, the growth mode is governed by the interface and surface energies only. In the Frank-Van der Merve mode (FM), the sum of film surface energy γ_f plus the interface energy γ_{fs} is lower than the substrate surface energy γ_s. A two dimensional layer covering the whole substrate is then more stable than a three dimensional crystalline island and the film is said to perfectly wet the substrate. The opposite happens in the Volmer-Weber growth mode (VW). In this case the energy due to the creation of the interface is higher than the surface energy of the substrate and film. Wetting is energetically unfavorable and thus the film-substrate interface is minimized by islands growth. In the framework of the wetting theory, the following criterion discriminate between layer and island growth[115,116] :

$$\gamma_s > \gamma_f + \gamma_{fs}, \quad \textbf{Frank-van der Merwe} \tag{4.1}$$

$$\gamma_s < \gamma_f + \gamma_{fs}, \quad \textbf{Volmer-Weber} \tag{4.2}$$

The presence of misfit and its accommodation has an influence on the surface and volume energies.[77,115,117] A change in $\gamma_{fs} + \gamma_f$ alone may drive a transition from the FM to the VW growth mode. For a strained epilayer with small interface energy, initial growth may occur layer-by-layer, but a thicker layer has a large strain energy and can lower its energy by forming isolated islands in which strain is relaxed. Thus the Stranski-Krastanov (SK) growth mode occurs.

4.1.1 Misfit accommodation

A theory to explain how two lattices accommodate their misfit has first been introduced by Frank and van der Merwe.[112]

The mechanism of misfit accommodation of the film on the substrate depends on: the misfit values, the elastic properties of the film, the bond strength with the substrate, the film thickness and the temperature. There exists a limiting value of misfit and a critical thickness, below which the film is stable without creation of dislocations. In this case the misfit is accommodated by strain only. For thick films misfit dislocations are always present unless lack of energy limits their formation. It is important to notice that the generation of dislocations is an activated process, i.e. a certain amount of energy is necessary. It is thus possible that, even if the presence of a dislocation would decrease the overall energy of the system, the energy available is not enough to overcome the barrier for its formation. In this case the growth of a continuous layer is not possible and the growth proceeds in a three dimensional mode with island formation, this is the SK mode discussed previously.

The critical thickness t_c, above which the film will develop dislocations to relax the misfit stress, has been calculated by Matthews[118,119] as:

$$t_c = \frac{b}{8\pi(1+\nu)m} \ln\left(\frac{t_c}{|b|} + 1\right) \tag{4.3}$$

where m is the misfit strain, b is the Burger's vector of the dislocation and ν the Poisson's ratio. The Burger's vector lies in the plane of the interface and is perpendicular to the dislocation line. The validity of the theory has been confirmed by studies on Si-based and Ge-based materials.[120–122]

4.1.2 Volmer-Weber growth mode

The Volmer-Weber (V-W) growth mode applies to both epitaxial and non epitaxial growth mode; films initially grow by the nucleation of discrete islands of different crystallographic orientation (or no crystallinity at all in the case of amorphous solids).

Upon additional deposition, the existing islands enlarge, and new islands may nucleate, until a continuous percolating network is achieved. The film continues to grow until the substrate is covered, followed by additional film thickening. Both during and after deposition, the film can undergo defect introduction and annihilation, grain growth, recrystallization. All these process can generate stress within the film.

Study of the stress evolution during growth have been performed for various films.[123, 124]

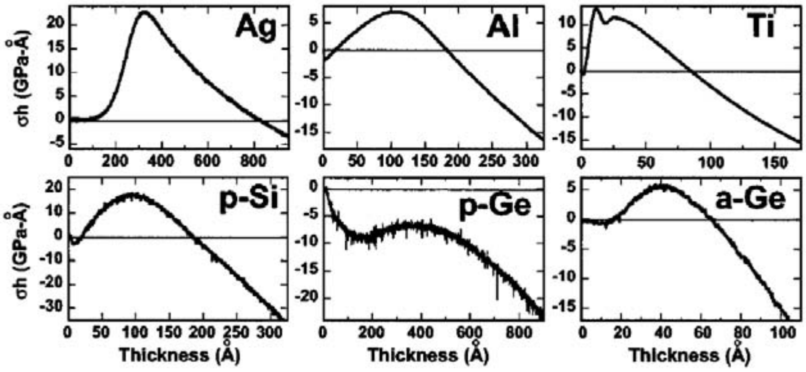

Figure 4.1: Stress-thickness vs stress during deposition of Ag, Al, Ti, polycrystalline Si, polycrystalline Ge, amorphous Ge. The substrate is SiO_2; no misfit strain can be defined in this case and stress is due to growth phenomena related to surface and interface energies. Positive values of stress thickness correspond to mean tensile stress, while negative values correspond to mean compressive stress.

It is generally observed that the stress evolves from compressive to tensile and back to compressive, as shown in fig.4.1 from ref.[124] In this study the substrate is amorphous and no misfit strain can be defined, the stress is due to growth phenomena related to surface and interface energies and has been directly correlated with the microstructural evolution.[124] The initial compressive stress occurs in the discrete islands stage of growth, while the rapid rise of tensile stress correlates with the onset of island coalescence and grain boundary formation. The peak in tensile stress occurs when the film becomes fully continuous, and in the final compressive stage the continuous film is thickening. When the deposition flux is interrupted in the final compressive-stress regime, a rapid relaxation of the stress occurs.[125]

The free surface of a solid particle is known to be stressed.[126] Surface stress in solids arises because the atoms of a solid in the vicinity of the surface have a bonding environment different from that of the atoms in the interior. As a result, the surface atoms will in general have an equilibrium interatomic distance different from the bulk value. Therefore the bulk of the solid can be thought of as applying a stress on the surface atoms in order to keep them in atomic register with the underlying lattice. The equilibrium atomic distance of the particle surface depends on its size and increase with it. During the early stages of V-W growth a particle is not tightly bonded to the substrate and can freely adjust its surface atoms according to the size, balancing internal and surface stress. When the particle becomes rigidly bonded to the substrate, its lattice parameter at the interface with the substrate is frozen and can not follow the growth any more. The difference between the lattice parameter corresponding to the island rigidly bonded to the substrate and the lattice parameter that it would have if it were free to adjust to its new equilibrium size, creates a misfit strain. Associated with this misfit strain is a biaxial stress that becomes increasingly compressive as the islands grows.[127] This prediction explains the initial compressive stress frequently observed prior coalescence.

Stress turns over to tensile at island coalescence, when the reduction of free surface and creation of grain boundary brings about a reduction in energy. In this case two islands can be driven to coalesce at the expense of some elastic energy originating the tensile stress. Different model have been proposed to describe the evolution of stress at coalescence,[128–131] in which material mobility and grain growth influence the magnitude of tensile stress developed.

A mechanisms responsible for the generation of the post continuity compressive stress in the film is the surface stress described earlier for the discrete islands stage. In this phase is the increase in thickness that first release the tensile stress and turns it back in to compressive. Another mechanism has been found to be responsible for compressive stress,[131–133] this is the incorporation of excess atoms in grains boundaries during deposition.

4.2 STO substrate surface

It is well known that a surface layer exists in perovskite of ABO_3 type which shows different properties compared to the bulk.[134,135] The existence of new phases is related to the chemical instability of $\mathrm{ABO_3}$ crystals in environments of low or high partial pressure of oxygen and is not restricted to the outer atomic layer of the surface which is in direct contact with the atmosphere. This reconstruction of the surface region already starts at room temperature and is particularly fast at elevated temperatures.[134] It is related to the existence of extended defects in perovskite of $\mathrm{ABO_3}$ type which serve as fast diffusion paths for O and AO complexes.[136]

STO (Fig.4.2) is a metal oxide with the cubic perovskite structure of lattice parameter 0.39 nm. Along the [100] direction, the unit cell of STO is a repeated stacking of individual titanium oxide and strontium oxide layers. The termination of any atomically flat (100) surface must be either titanium and oxygen (fig.4.3a) or strontium and oxygen (fig.4.3b). Cleaving or cutting, though, give a resultant surface with an

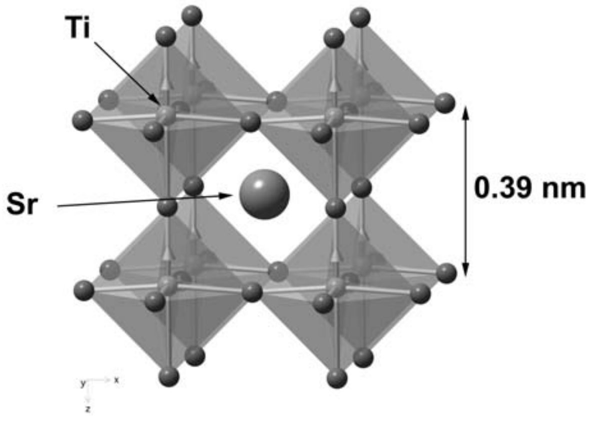

Figure 4.2: Perovskite structure of $SrTiO_3$ (STO): Sr and Ti atoms are indicated together with the lattice parameter of the cubic cell.

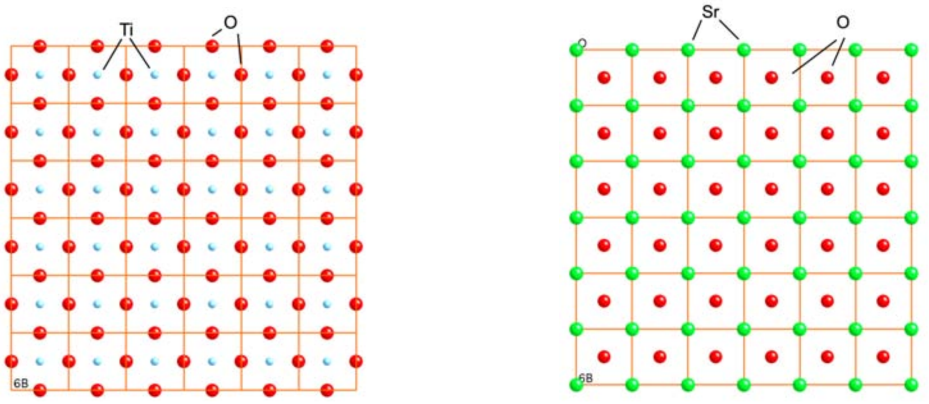

a) b)

Figure 4.3: a) SrO and b)TiO_2 planes of the STO structure.

equal amount of the two termination. Clean surfaces of single crystal substrates are usually prepared by flashing at a high temperature for a short time in ultra-high vacuum (UHV). High temperature treatment of multi-elementary compounds may induce decomposition and non stoichiometry. In the case of STO, thermal treatments above 900° and low oxygen pressure, induce a Ti-rich surface phase of type TiO_x and loss of oxygen with time from such a formed surface. In oxidizing conditions segregation of Sr atoms at the surface is observed with formation and continuous accumulation of a SrO-rich layer. At temperature lower than 1000°C diffusion of the SrO in the bulk is not expected, just the formation of a monolayer at the surface. Thermal roughening and step bunching can occur as well.[134]

Kawasaki et al. and Koster et al.[137,138] have shown that the TiO_2-termination can be prepared by wet chemical etching. The more basic oxide SrO is selectively etched by a NH_4F buffered HF solution. The proper solution pH as well as the previous polishing and proper thermal treatment of the surface, determine the good result of the procedure. Dipping the surface in demineralized water prior etching, lead to the formation of an intermediate Sr-hydroxide and a reproducible, very good TiO_2 surface upon etching in a pH 5.5 solution. Subsequent annealing in the range $600° - 800°$ produces flat terraces and evaporates contaminants like carbon.

The lattice parameter of the two terminations is the same, meaning that any change in growth behavior can be interpreted in terms of a change in interfacial energy due to a change in the degree of chemical bonding across the interface. Surface reconstructions have been studied in the case of TiO_2-terminating surface and different configurations have been observed.[?]

The (111) layers in the bulk consist of Ti(4+) and SrO3(4-) layers (Fig.4.4). Such highly charged layers cannot be stable at the surface. One expects a reconstruction to reduce the large dipole moment. Chemical or thermal treatment of the (111) surface did not lead to a noticeable influence on SBN.

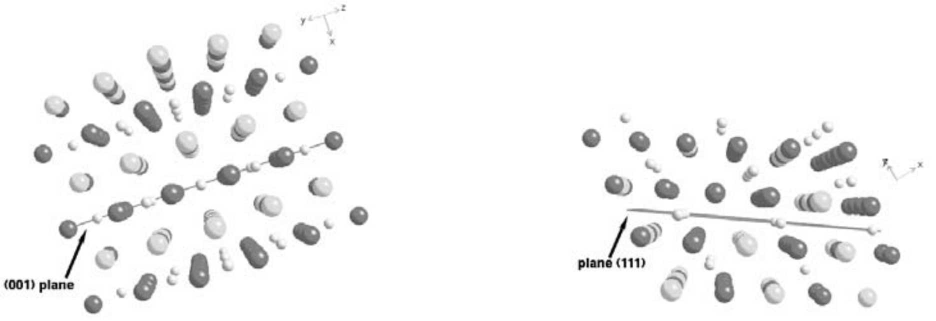

a) b)

Figure 4.4: STO crystal showing: a)the (100), and b)the (111) plane. In both cases there are Ti rich layers alternated to Sr rich layers.

4.3 Growth of SBN

4.3.1 Substrate preparation and deposition parameters

SBN thin films have been grown on STO (100)oriented single crystals. The substrate has been utilized as received from the producer or treated in BHF for one minute after being dipped in demineralized water for about 30 min, this process creates a TiO_2 terminating surface. In order to create a SrO surface some substrate have been annealed in oxygen for 5h at 950° after being etched. Terraces 200 nm wide with steps of 0.4 nm are clearly visible on non treated surfaces (fig.4.5). No defined diffraction pattern is produce in RHEED experiment, indicating a high degree of crystalline disorder. RHEED diffraction patterns from wet-etched surfaces (fig.4.6) show well defined bright spots that become strikes upon heating (fig.4.7a)).

Films have been deposited at substrate temperature in the range $730-760$°C, in oxygen atmosphere of 200-400 mTorr, with target substrate distance 50-90 mm, laser pulse repetition rate 1-10Hz and 200-400mJ per pulse. Crystalline films have been obtained in the whole range of used condition, the degree of crystallization and ordering increase with increasing temperature and is less sensitive to the other parameters. RHEED fraction patterns are spotty-like (fig.4.7b)) indicating a high degree of roughness.

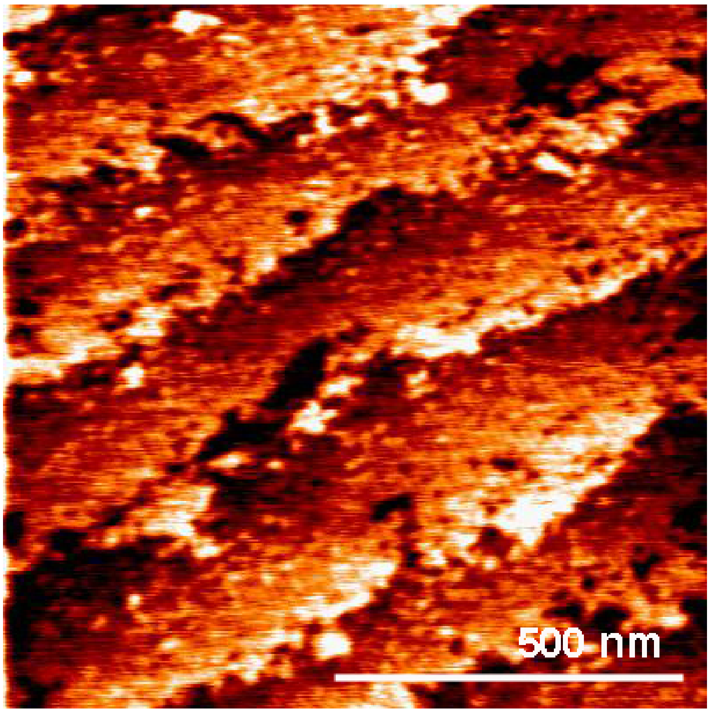

Figure 4.5: AFM image (contact mode in vacuum) of non treated STO surface. The terraces are about 200 nm wide, the step height is 0.4 nm compatible with the unit cell dimension.

4.3.2 Phenomenology of growth

Preparation of the STO substrate with chemical an thermal treatment of has a strong influence on the growth of SBN films and their surface morphology . Films grown on

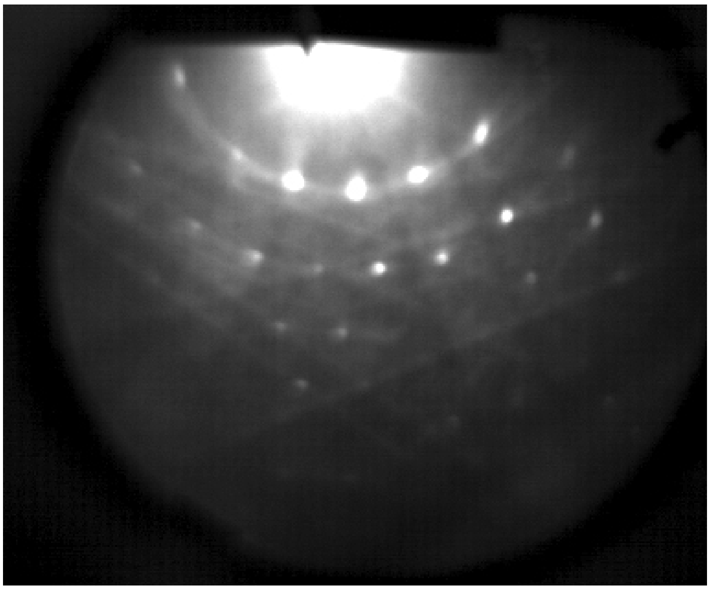

Figure 4.6: RHEED diffraction pattern from etched surface of STO at room temperature: bright and well defined spots indicate a rough surface.

non-treated or treated substrates are clearly distinguishable as evident in the AFM images: fig.4.9 corresponds to the non treated case and fig.4.10 to the etched case. The image 4.11 was taken from the etched sample after annealing at $T = 950°$.

$\theta - 2\theta$ X-ray diffraction patterns of SBN grown on both treated or non treated STO surfaces (fig.4.8) have a strong peak at $2\theta = 22.5$. Two different planes give diffraction at this angle, (001) at 22.49 and (310) at 22.519,with a difference in 2θ of only 0.03°. Because of measurements resolution and peak width it is impossible to determine which of the two is actually present or if the film is a mixture of the two orientations. From the ferroelectric point of view this two orientations are completely different as the polarization axis is perpendicular to the film plane in the first case and in the plane in the second case.

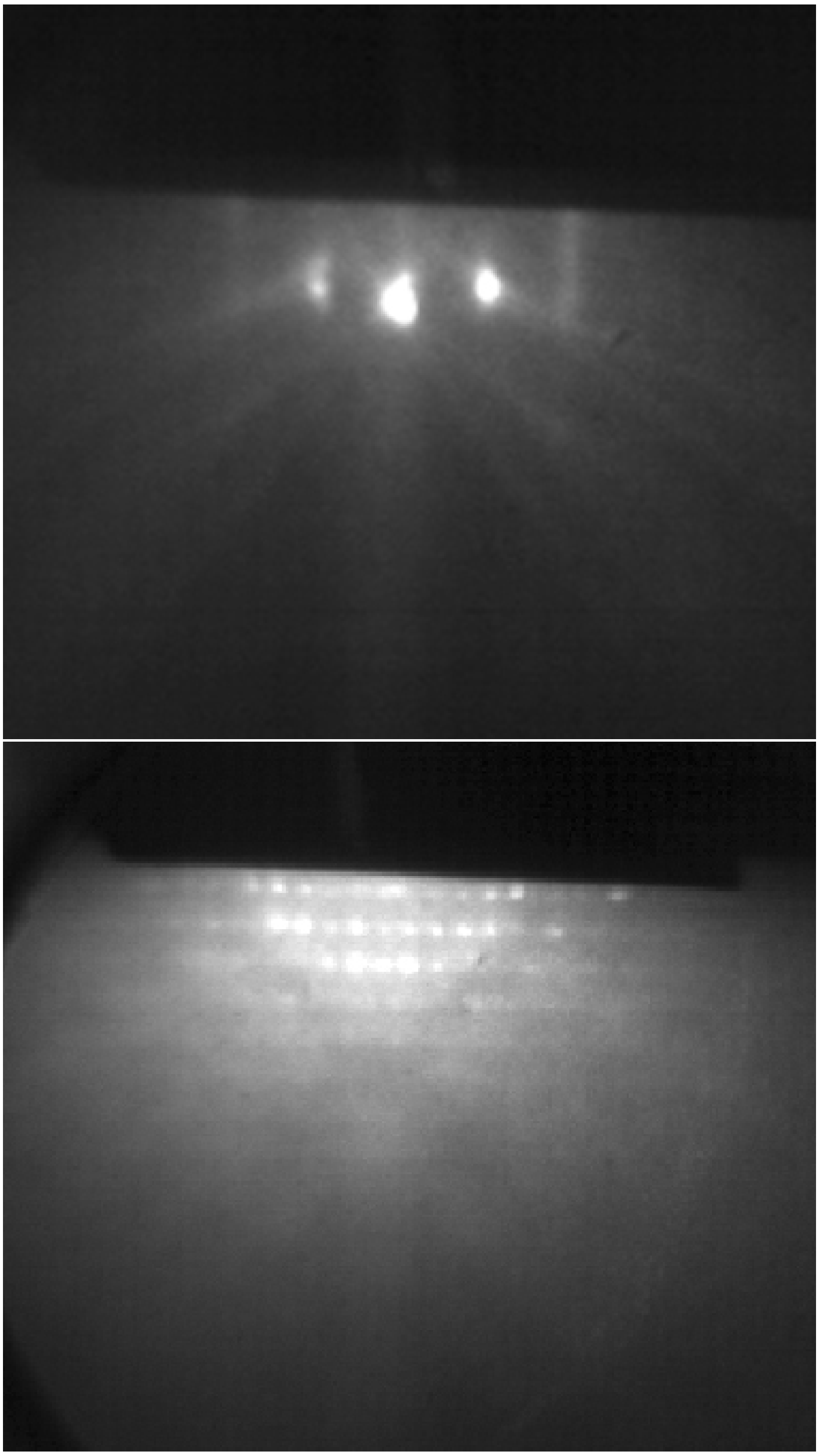

Figure 4.7: Rheed diffraction pattern from: (top) etched STO surface at 750°, (bottom) SBN film at room temperature. The STO surface, rough at room temperature, becomes smooth at deposition temperature. The SBN film is rough, this is confirmed by AFM measurements.

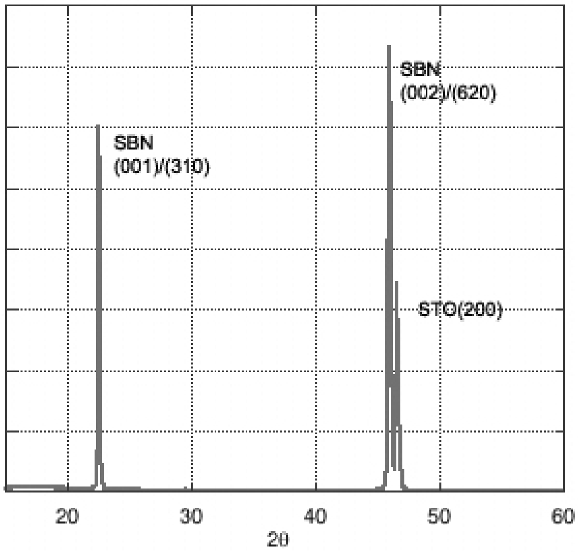

Figure 4.8: X-ray of SBN film grown on non-treated STO surface: 750°C, 300mJ per pulse, 10Hz, 80mm target-substrate distance.

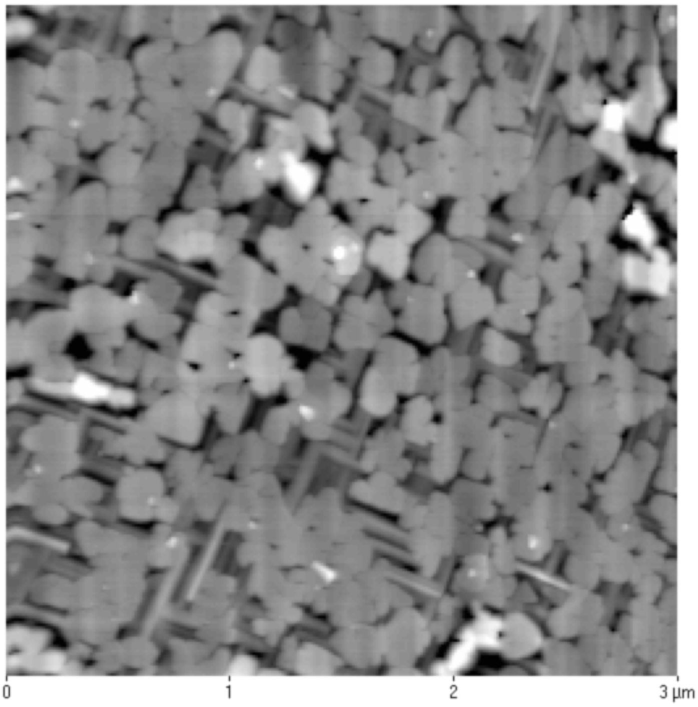

Figure 4.9: AFM image of SBN film grown on non-treated STO surface: 750°C, 300mJ per pulse, 10Hz, 80mm target-substrate distance. Columnar grains are the dominating feature, few rods are visible as well.

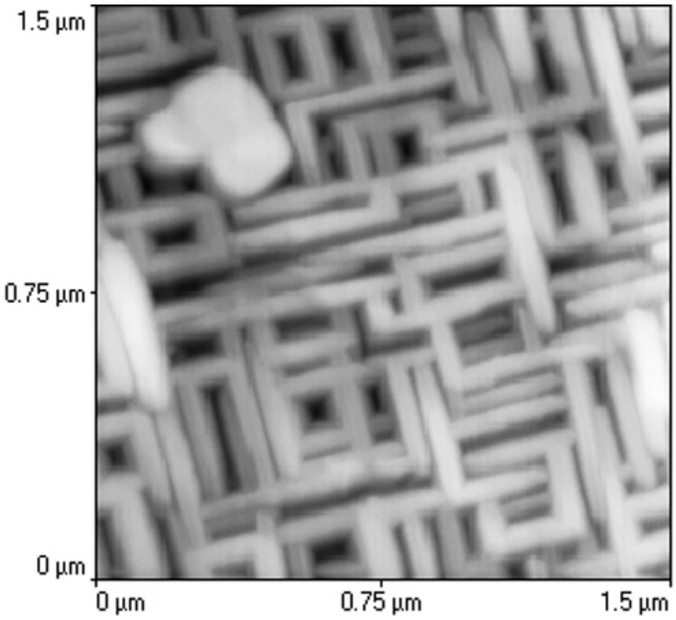

Figure 4.10: AFM image of SBN film grown on BHF etched STO surface: 750°C, 300mJ per pulse, 5Hz, 80mm target-substrate distance. Here the film grows in rod shaped grains, round grains are nevertheless present, due to imperfection in the TiO_2 termination of STO. The rods grow parallel to the STO axis, the round grain is rotated by about 18°.

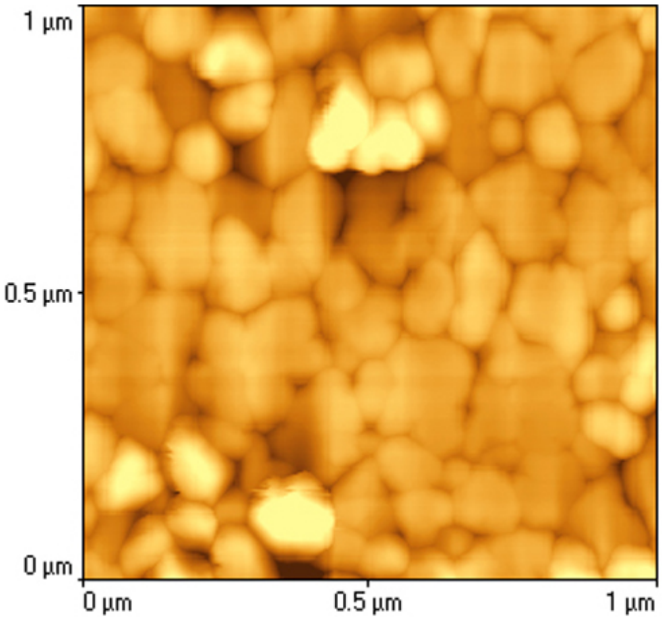

Figure 4.11: AFM image of SBN film grown on BHF etched and annealed STO surface: 750°C, 300mJ per pulse, 10Hz, 80mm target-substrate distance. In this case only the columnar growth is visible, grains are as wide as 300nm.

4.3.2.1 Growth on TiO_2 terminating substrate

When the STO surface is etched prior to the introduction in vacuum the SBN film grows in rod-like shaped grains. The rods, about 30-50 nm wide, have variable length of about a few hundred nm. They grow perpendicular to each other with the main axis along the STO [100] axes. The diffraction pattern of Fig. 4.12 shows that in these grains the (001) plane is perpendicular to the film. From the cross-section diffraction pattern a tilt of the SBN lattice with respect to the STO lattice is evident (fig.4.14). The [310] axis of SBN is oriented along the [100] axis of STO. The [001]-axis of SBN is consequently parallel to the [010] axis of STO. The a-axis of SBN is tilted around its c-axis to form and angle of $\pm 18, 43^\circ$ with respect to the [100] axis of STO. Such a tilt is shown in Fig.4.15.

The film grows in a dense morphology. A very specific feature is the growth direction of the grains. The grain boundaries include an angle of about 18° with the film normal, meaning that the grains grow along the [100] direction (fig.4.17).

$\theta - 2\theta$ X-ray diffraction pattern show a peak at 2θ=29.5, corresponding to (410) planes (fig.4.18). Such a peak is hardly distinguished from the background or dominating depending on deposition condition. The (410) orientation is more likely to grow when the energy provided to the system is lower, i.e. lower temperature, larger distance from the plume and fast deposition rate. Other peaks are present in the X-ray diffraction pattern in this case, indicating a disordered growth. From TEM study of the film substrate interface only (310) oriented grains are revealed. We conclude that the (410) orientation belongs to grains growing on top of the (310) ones.

The rods are densely distributed and quickly cover the whole substrate in a way that the surface resembles those of a thicker film, that is already the case of a 2 min long deposition corresponding to a thickness of about 20nm. If the growth is stopped, the sample cooled down and then reheated for a second run of one minute,thicker isolated rods are formed, fig.4.19. That is an indication of non equilibrium condition for the system that relax to a configuration of lower energy during the intermediate annealing step. During the second run the material grows preferentially on the preexisting SBN structures.

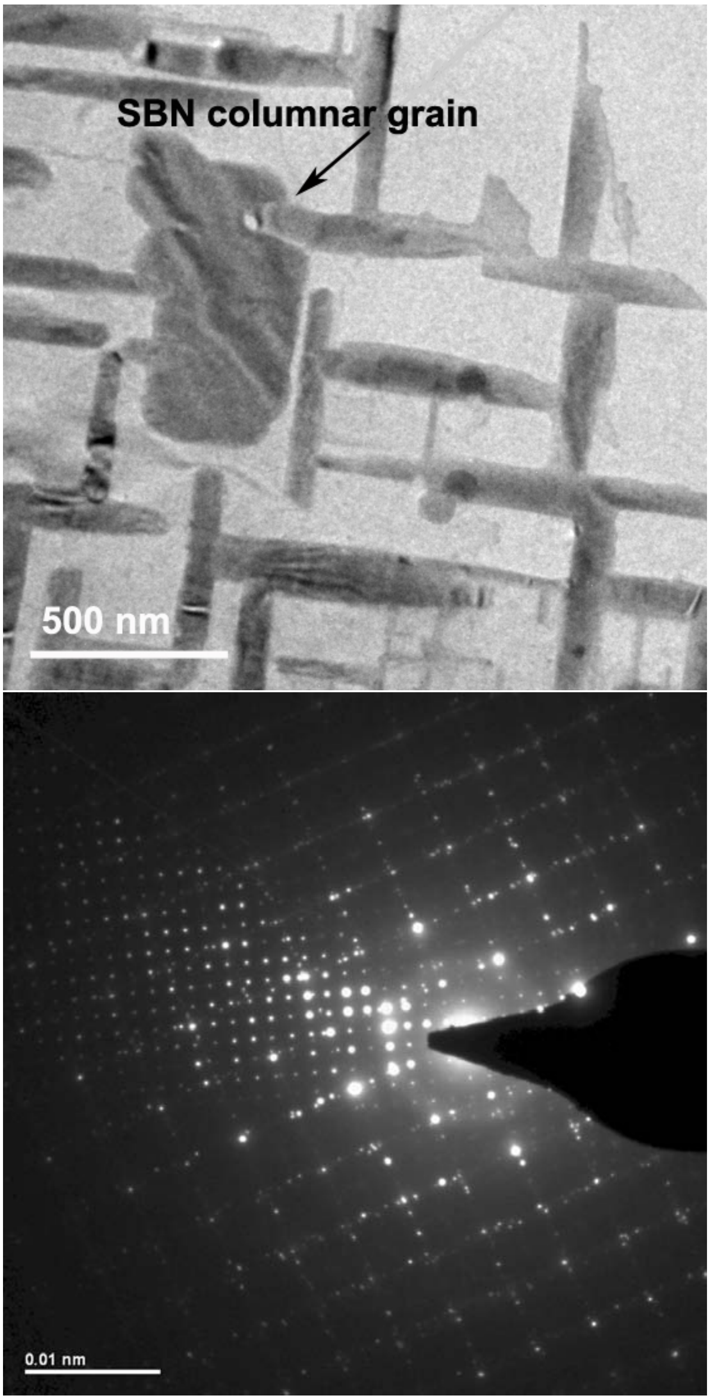

Figure 4.12: (top) Plane bright field micrograph and (bottom) diffraction pattern of a columnar and rod-like shaped grains: the columnar grain has the [001] axis perpendicular to the plane while rod-like grains have the same axis laying in the plane

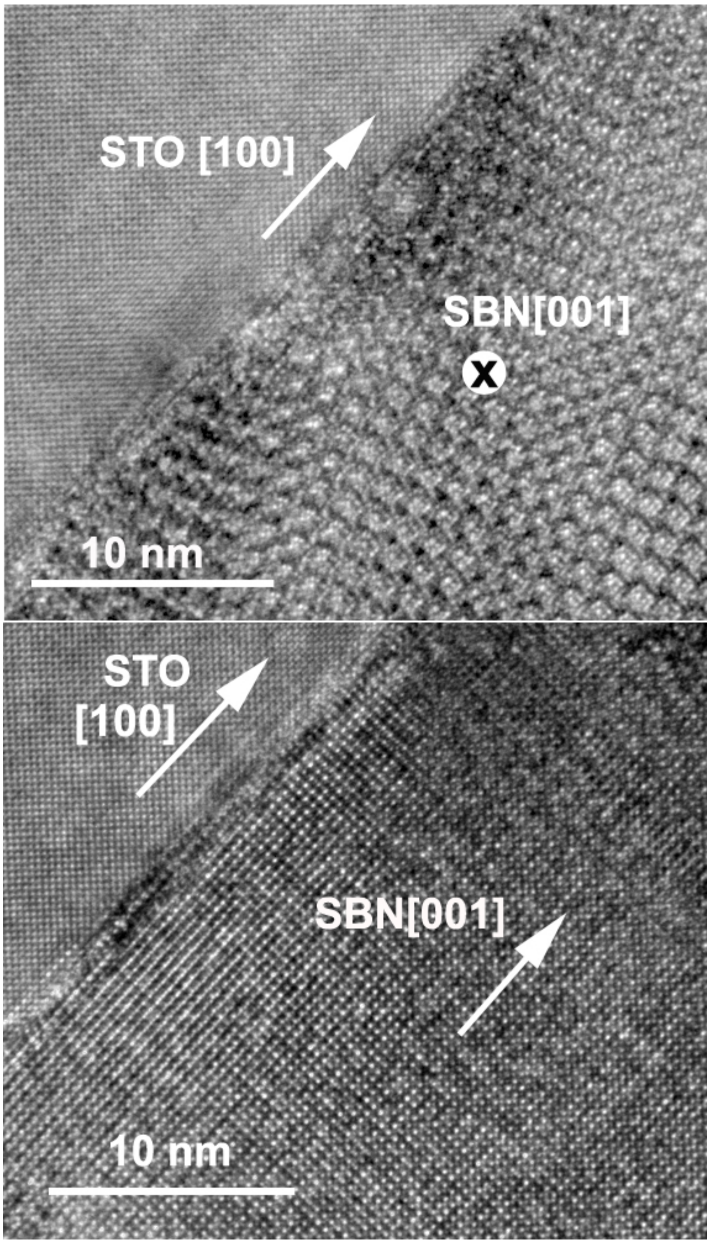

Figure 4.13: Cross-section high resolution micrographs of the interface between STO and two different SBN grains: in both images the STO[001] direction is laying in the plane of the film. The SBN [001]direction is out of section plane in the upper, and in the section plane in the lower image.

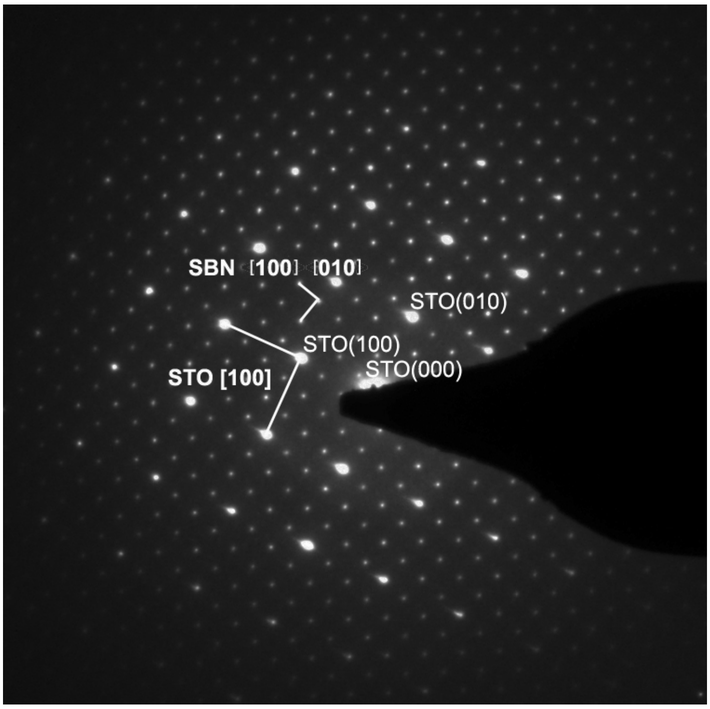

Figure 4.14: Diffraction image of a grain with [001] axis laying in the film plane: case of the top image in figure 4.13, spots from both film and substrate are visible.

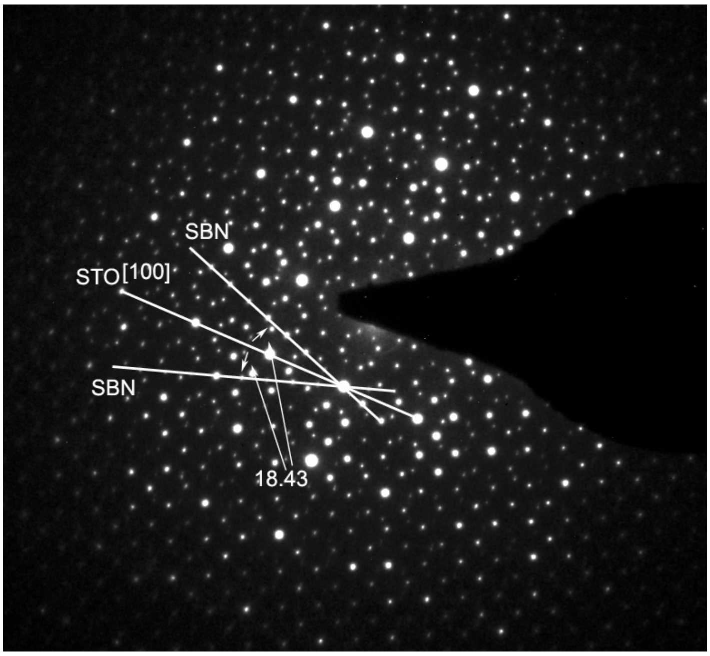

Figure 4.15: Cross sectional diffraction image of (310) oriented grains with [001] axis laying in the plane: spots from both film and substrate are visible. SBN(001) planes are tilted by ±18.43 respect STO (100) plane.

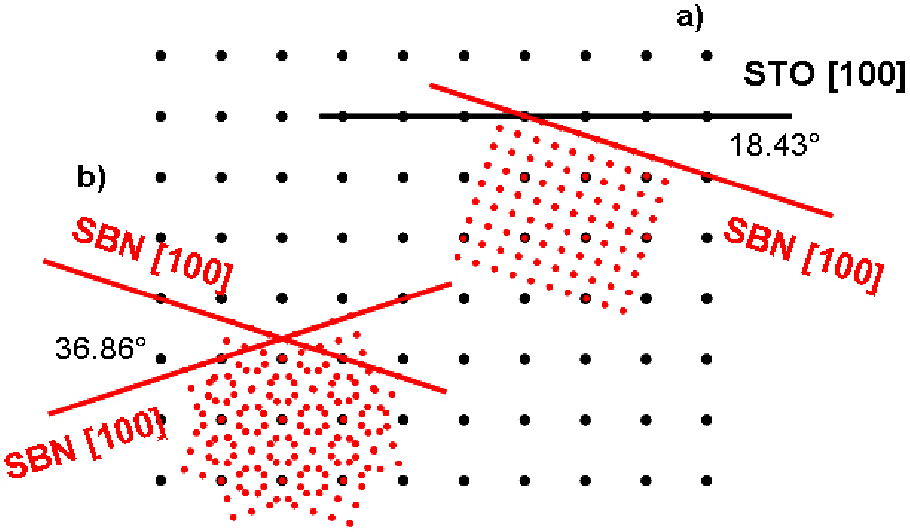

Figure 4.16: Interpretation of the diffraction images 4.14 in a), and 4.15 in b). In a) the STO reflection from the plane (100) are superimposed to the reflection from planes (001) of SBN and reveal the 18.43° rotation of the two lattice. In b) reflection of STO are superimposed to reflection from SBN(001) grains rotated by + or − 18.43° as for fig.4.15

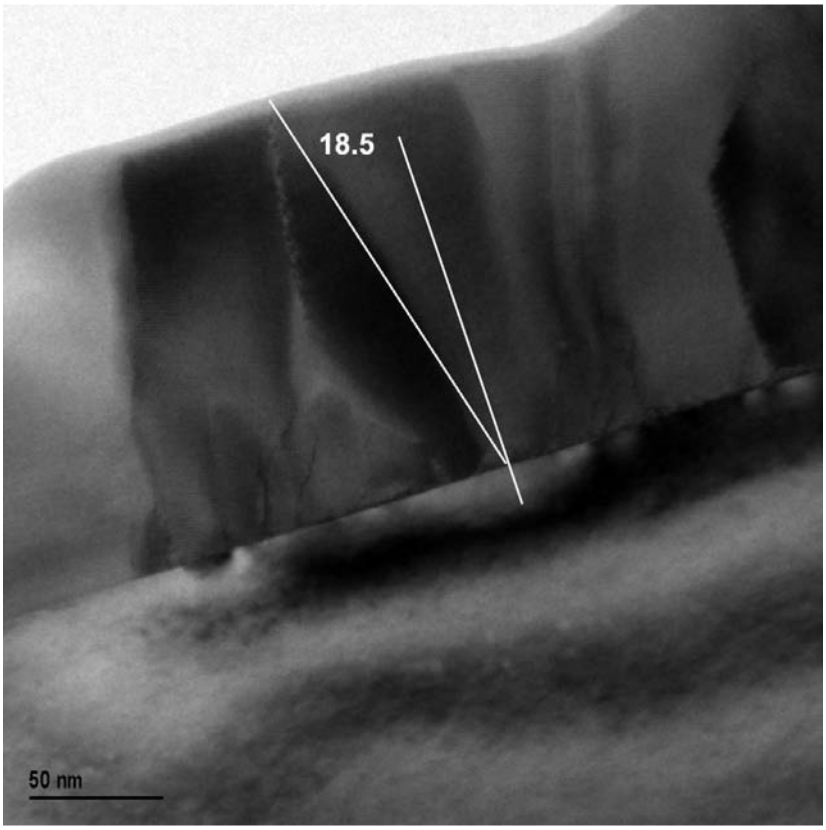

Figure 4.17: TEM micrograph of SBN film grown on wet-etched STO surface: tilted grains and irregularities are visible, the interface with the substrate looks stressed. The grain boundaries frequently show an oblique direction forming a 18° angle with the film normal. This indicates that grain boundaries are constituted by (010) planes.

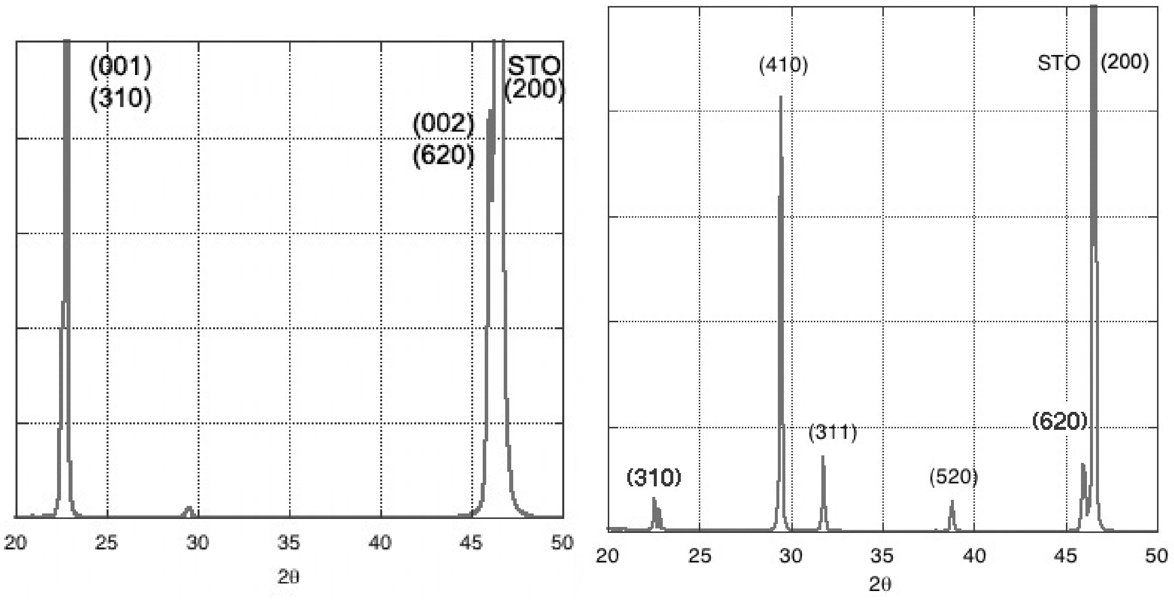

a) b)

Figure 4.18: $\theta - 2\theta$ X-ray diffraction pattern from films grown on etched STO substrate: a) 750°C, 300mJ per pulse, 5Hz, 75mm target-substrate distance b)750°C, 200mJ, 10Hz, 85mm target-substrate distance.

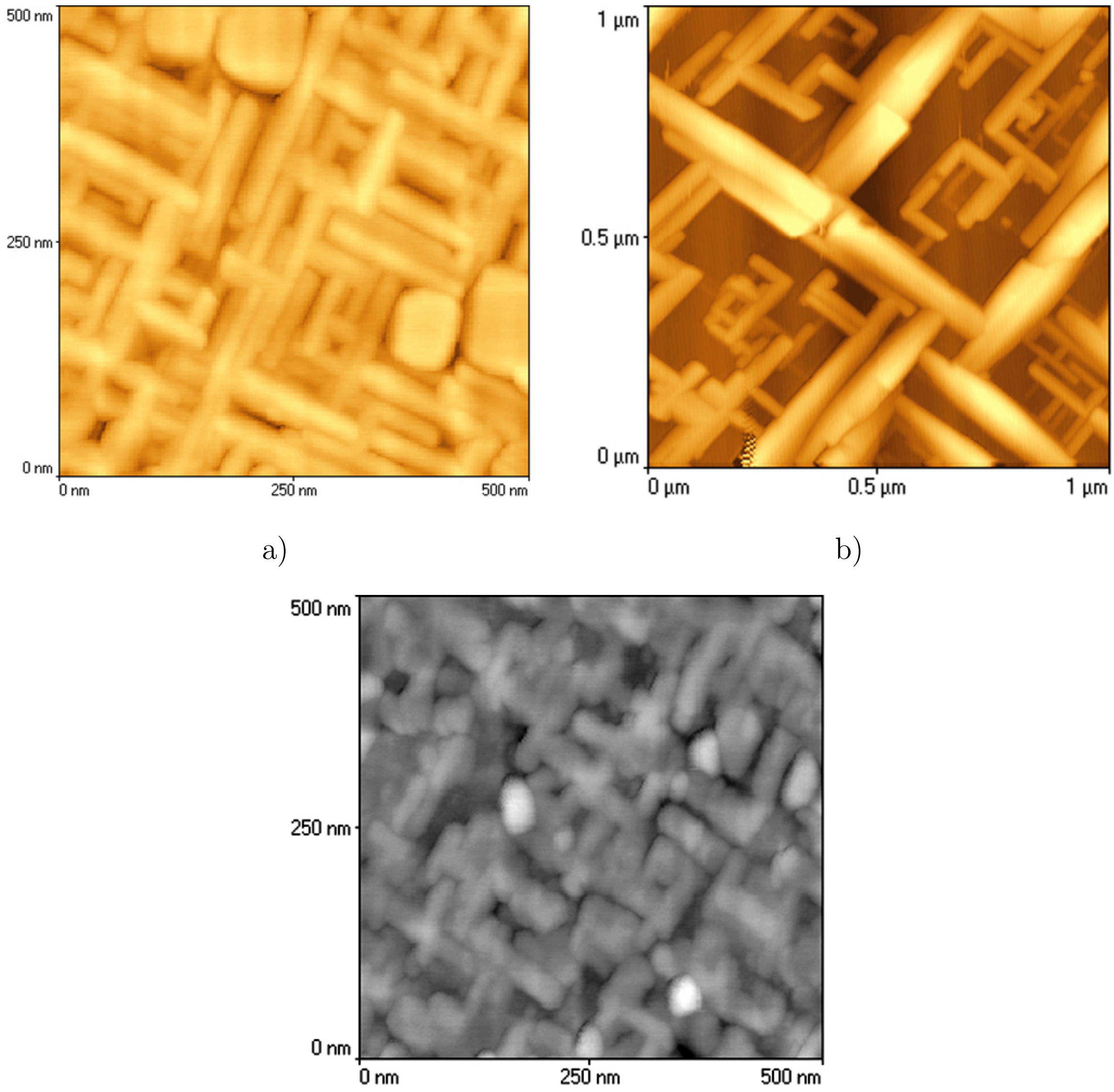

a) b)

c)

Figure 4.19: SBN on etched STO: 1 min deposition at 10Hz 300mJ 750°C. a) the surface is already densely covered by rods like the thicker films are, b) the film has been heated-up again to 750° and deposition continued for 1min more, c) 1 min deposition at 780°. In case b) rods are well separated and up to 50 nm thick, the annealing created a new distribution and the atoms deposited after annealing preferentially accumulated to the already existing grains.

4.3.2.2 SrO terminating substrate

On an oxygen annealed substrate SBN film grows in columnar grains of about 100nm diameter with the (001) plane parallel to the film plane. The SBN unit cell is rotated by 18.43° respect to the STO lattice (fig.4.12). The columns nucleate as independent units, then grow perpendicularly to the substrate up to the film surface, resulting in its average roughness of 6 nm. The interface with the substrate is sharp and the structure of the film is regular and dense,(fig.4.20).

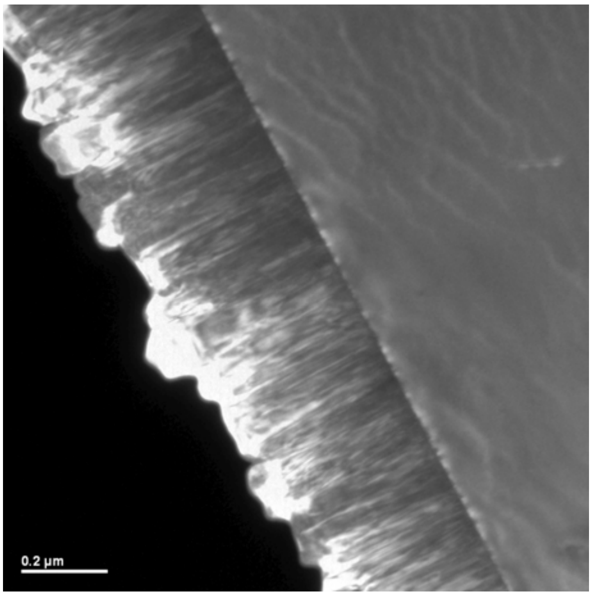

Figure 4.20: Dark field TEM image of SBN film grown on SrO surface: 750°C, 300mJ per pulse, 10Hz, 80mm target-substrate distance. A dense columnar structure is visible: columns are about 100nm wide and reach from the bottom to the top of the film.

4.3.2.3 Random STO surface

On a non treated STO substrate, the film grows mainly in columns like it does in the SrO terminating substrate. The growth starts with isolated round particles of about 100 nm diameter and a very few rods, some rods persist to the end of the growth process but other are covered by the expanding (001) oriented grains (fig.4.21). The structure is regular and dense and the interface with the substrate is sharp. Small

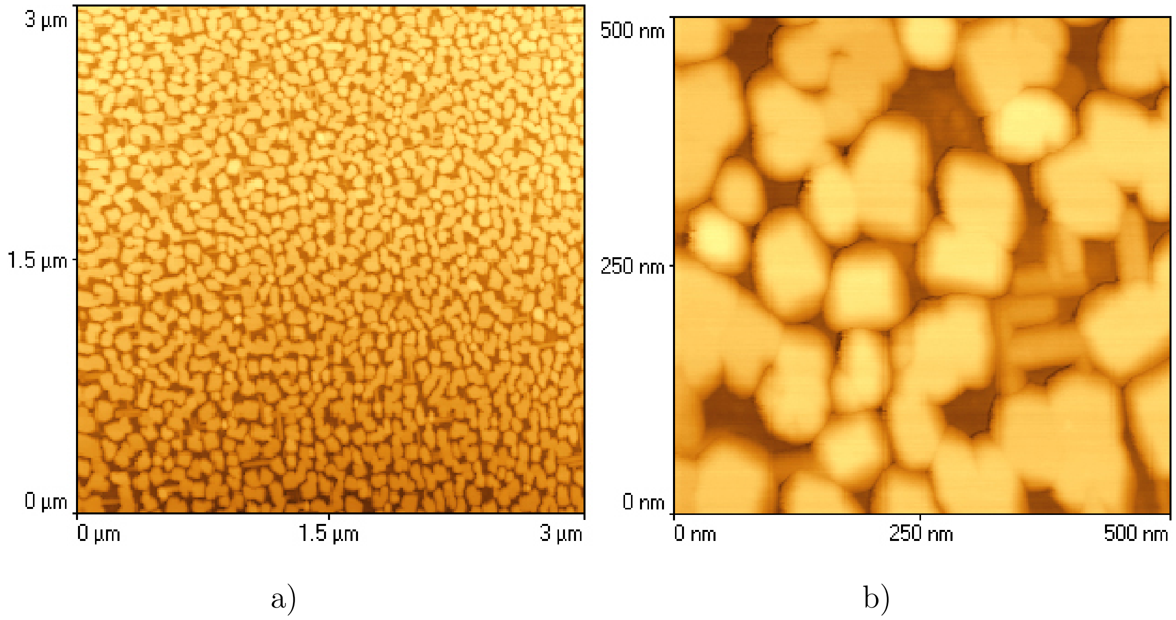

a) b)

Figure 4.21: Initial stage of growth on non treated STO substrate, 1min at 750° 10Hz pulse frequency: a) standing-alone columnar grains are uniformly distributed on the surface, b) rods are assembling occasionally.

(310) oriented grains grow at the interface and are buried by (001) oriented grains (see fig. 4.22).

The rod-shaped grains are present in quantities that differ from sample to sample but always as a minority. Such mixing of features is expected as the substrate surface is constituted of both termination at 50% in average, a great variability can be expected from sample to sample. In figs. 4.23 to 4.26, XRD pole figures obtained from (001) and (310) oriented films are shown (treated substrates). These measurements prove that the whole film grows with only one specific orientation and there is no mixing of the two. They confirm that the films grow globally in the same way as the TEM investigation has revealed. Calculated spectra are shown in figs 4.24 4.26, measured and calculated reflection are shown. Twin domains of ±18° and ±90°, around the [100] axis of STO, are formed by (001) and (310) in plane orientation respectively. In any case, for low deposition rates ($< 5/sec$), (001) and (310) are the only orientations obtained. No random nucleation is observed.

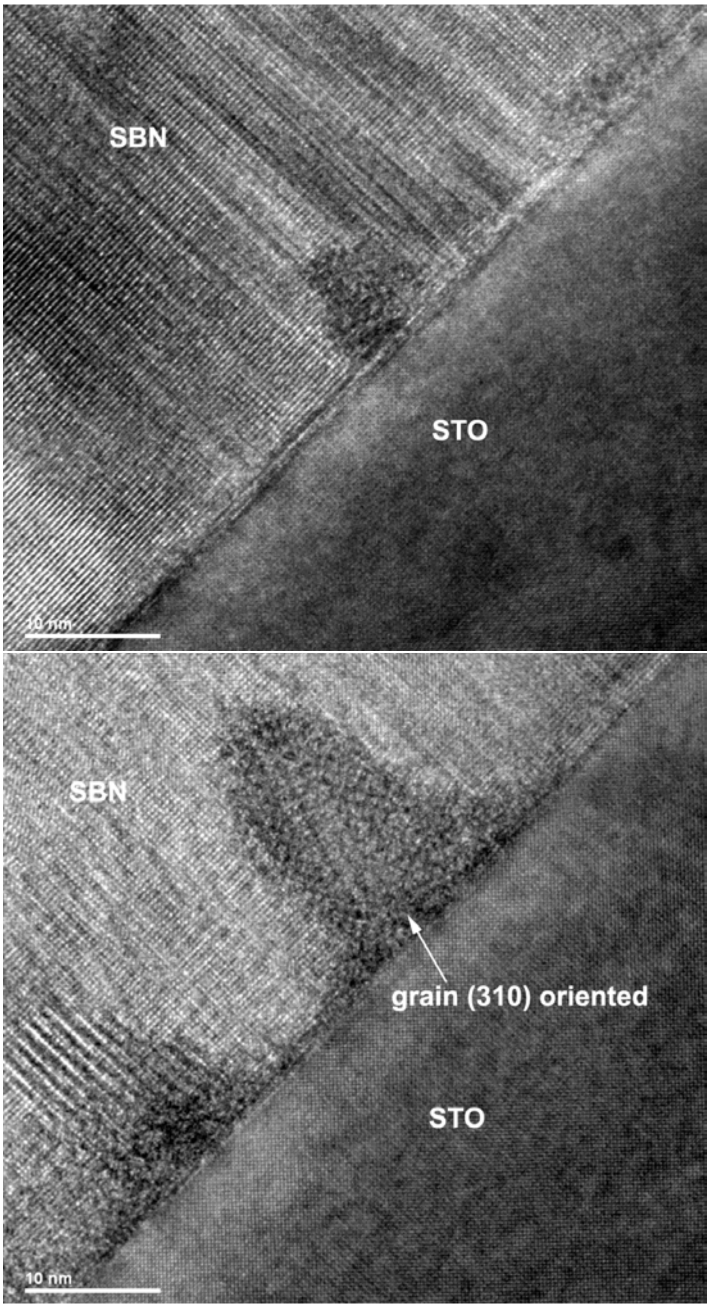

Figure 4.22: High resolution TEM image of SBN film grown on non-treated STO(100) surface Top image: (001)-oriented grains with a sharp interface with the substrate. Bottom image: (310)-oriented grains are observed at the interface with the substrate, their growth is limited by the surrounding (001) grains.

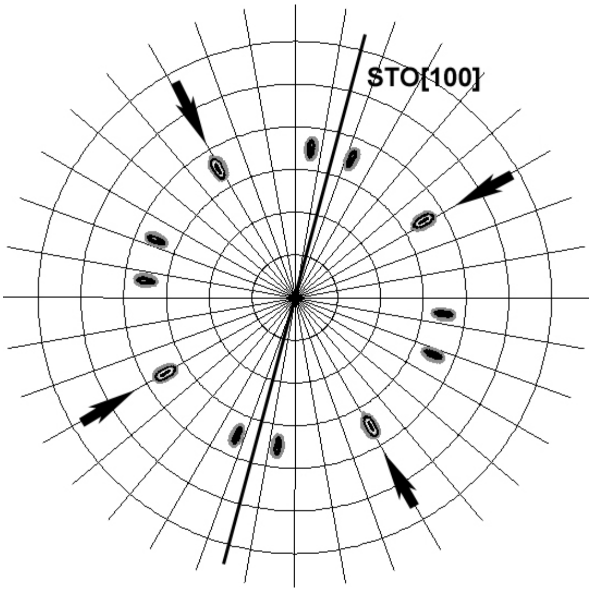

Figure 4.23: Pole figure of a SBN film grown on SrO terminated STO(100) substrate, obtained measuring the (211) SBN reflection . The arrows indicate the position of measured STO(211)reflection, from which the position of STO[100] axis (indicated by the line) has been calculated. Once the SBN spot identified, this gives us information about the relation of SBN with the STO substrate. In fig.4.24, the (211) SBN reflections are calculated for comparison.

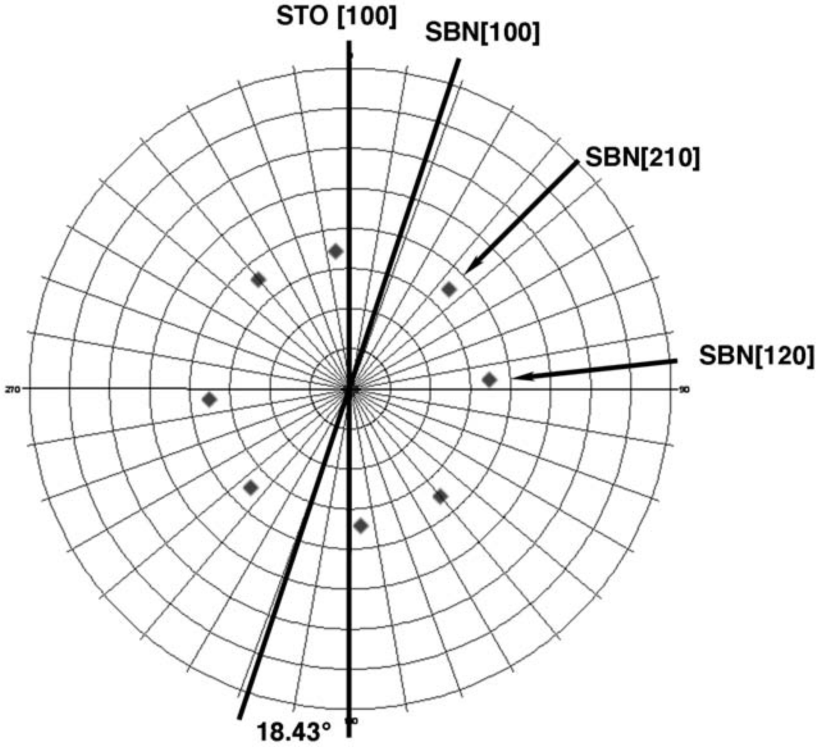

Figure 4.24: The calculated (211) reflection of (001)oriented SBN are indicated by the spots. The position of SBN[100] has been calculated and indicated by the line. The additional measured reflections of fig.4.23, are obtained by a rotation of 36.86° to the left of all the SBN spot. After such a rotation, this figure coincide with the measurement of fig.4.23 and show as the SBN lattice is rotated by 18.46° respect to STO.

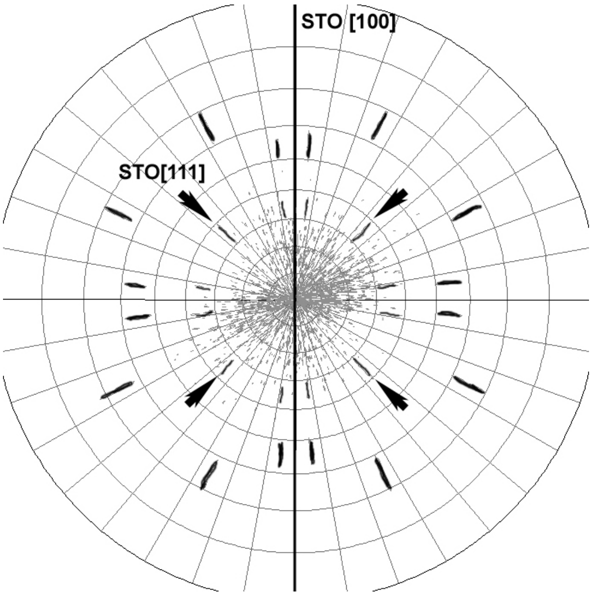

Figure 4.25: Pole figure of a film grown on etched STO(100) substrate, obtained measuring the (211) SBN reflection . The arrows indicate the position of measured STO(111)reflection and the line indicates the calculated position of STO[100]. Once the SBN spot identified, the relation of the film with the substrate can be determined. In fig.4.26 the reflection from SBN are calculated for the comparison.

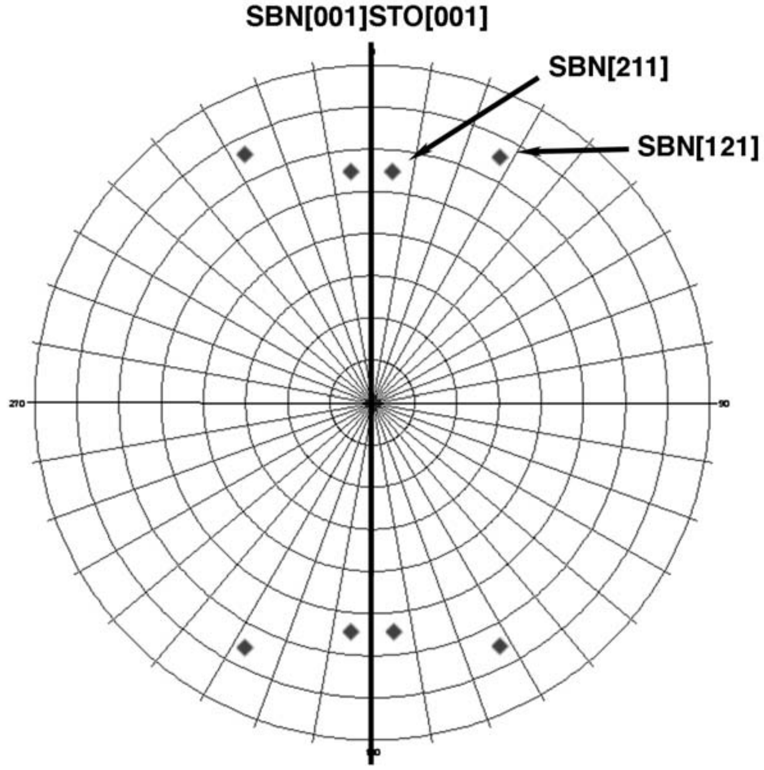

Figure 4.26: The calculated (211) reflections of (310) oriented SBN coincides with the measurement of fig.4.25 where the outer reflection are considered. The extra reflection are obtained by a rotation of 90°. The position of SBN[100] is indicated an coincides with the position of STO[100] derived from the measurement of fig.4.25

4.3.2.4 SBN on STO(111)

SBN on STO (111) grows with (421) planes parallel to the (111) plane of the substrate as shown by the X-ray diffraction measurement in fig.4.27. A Ti rich STO(111) surface, has been reported to form upon annealing at 950°C or more, in UHV.[139,140] Thermal behavior of the (111) surfaces is thus similar to the one of the (100) surface as reported in Sect.4.2. We do not expect any effect at the deposition condition. There are no studies, to our knowledge, about chemical etching of STO(111) surface. In our case, BHF etching of the substrate does not have an effect on the growing film, nor does the temperature of the substrate. The deposition conditions to obtain a crystalline film are found to be the same as for STO(100) substrate.

The wetting power of SBN is in this case strongly reduced, and islands as thick as 50-80 nm are formed after 1min of deposition, well before coalescence. The island grow in pyramids from 30 to 200 nm at the base (Fig.4.28a)). Such pyramids are composed of 30-50nm wide slices.

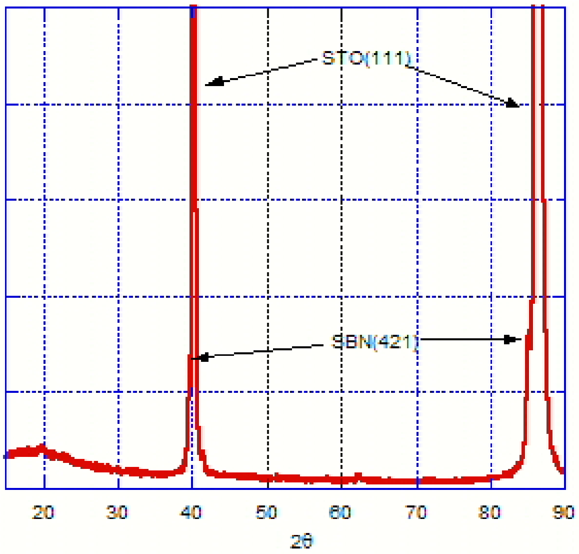

Figure 4.27: $\theta - 2\theta$ X-ray diffraction pattern of SBN grown on STO(111), the small peaks belong to the SBN film. Deposition conditions:750°C, 10Hz, 250mJ

A saw tooth profile of the surface is kept in thicker films (Fig. ??). This indicates that

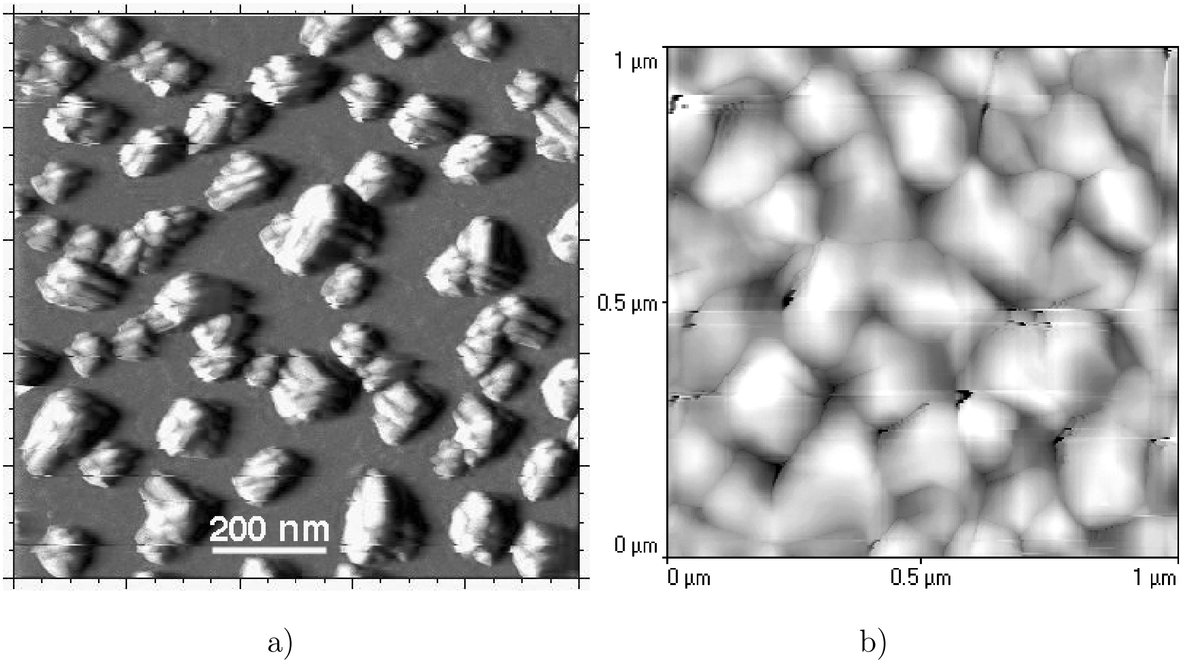

a) b)

Figure 4.28: AFM topographic image of SBN film grown on STO(111) substrate: a)1min deposition, b)60 min deposition

the substrate determine the orientation of the film but the growth of grains proceeds along a preferential orientation typical of SBN. Most probably this is the $< 001 >$ crystallographic direction. The grains height do not always span the entire thickness of the film and inclusion are visible. The growth, fig.4.29, seem to be less ordered than what seen in the case of STO(100) substrate.

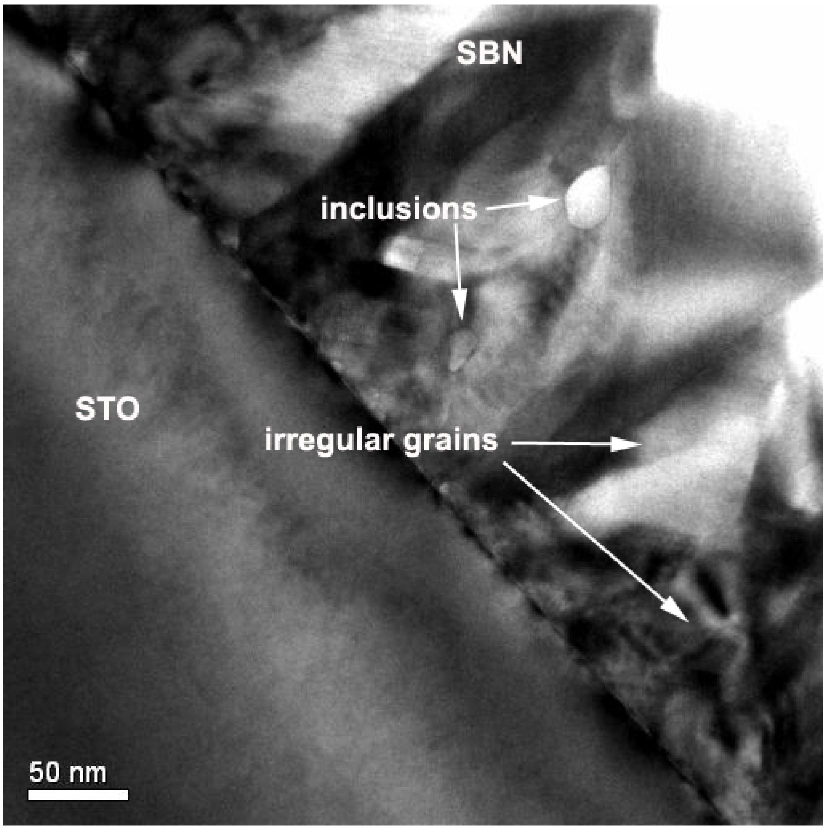

Figure 4.29: Bright field TEM image of SBN film grown on STO(111) surface: the interface is sharp and the structure is dense. The grains do not grow from the substrate through the whole section of the film and inclusions are visible.

4.4 Model of growth

4.4.1 State of the art

Epitaxial growth of SBN [001] oriented thin films has been obtained on following substrates: SBN(001) (homoepitaxy),[97] $LaNiO_3/CeO_2/YSZ/Si(100)$ multilayer (LNO (001) oriented),[68] MgO(100)[53,55,64,65,73] and STO(100)[67,95] single crystals. It is interesting to note that these epitaxial systems lead to the formation of SBN-related antiphase domains in the (001) plane. In the homoepitaxyal system composed of SBN61(001) oriented film grown on SBN75(001) single crystal, the film forms grains aligned with the substrate and grains rotated by ±28° around the substrate normal [001]. Grains with fourfold symmetry, rotated by ±18.43° with respect to the a-b axes of the substrate grow on LNO, MgO and STO single crystal. In the case of MgO(100) substrate, grains rotated of ±31° have been reported as well.[53,65] These extra orientation seems to be less probable and strongly influenced by the substrate surface preparation. Domain formation in all these epitaxial system has been interpreted by considering the interplay between processes that minimize lattice misfit and those that allows for balance of Coulomb's forces as the two lattices try to accommodate each other across the interface.

MgO is a particularly good substrate to grow (001) oriented SBN because of the low mismatch with SBN lattice. Considering three MgO unit cell (MgO a=0.42 nm SBN a=b=1.245 nm) it amounts to about 1.2 %. As discussed in ref.,[55] the poor alignments of the inner atoms of SBN unit cell with the MgO atoms, obtained in the configuration with parallel a axis, is substantially improved by a rotation of 18.4°, however, the lattice mismatch increases to about 6%. For a complete appreciation of lattice matching, the bonding strength has to be considered as well. In case of ionic crystals, the bonding strength is mainly governed by electrostatic interaction. SBN has a layered structure, fig.4.30, in the layer at $z = 0.5c$ concentrate oxygen and Sr Ba cations, the rotation of ±18.43°, make the oxygen atoms in this layer to coincide with the Mg cations of the substrate. The layer at $z = 0c$ contains Nb cations and oxygen and in this case upon rotation, are the oxygen anions that superimpose to Mg cations. Growth starting from

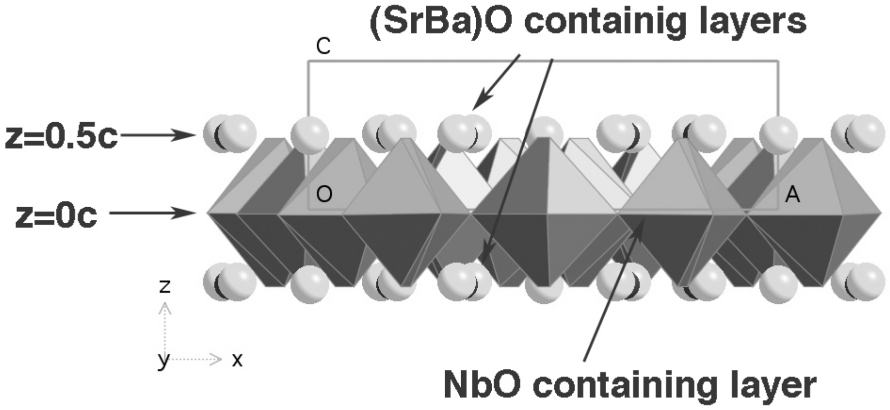

Figure 4.30: SBN unit cell: the layers at $z = 0c$ (NbO containing) and at $z = 0.5$c ((SrBa)O containing) are indicated.

this second layer, rotated by ±18.43°, should be favored from the electrostatic point of view and that would compensate for lattice mismatch.
Epitaxial growth of SBN(310) oriented film with rod shaped grains, on STO(100) single crystal, has been reported by Nishio et al.[69,71] but details of the epitaxial relationship have not been analyzed.

4.4.2 Discussion of our experimental results

The TTB unit cell of SBN is characterized by the following constitutive elements:

- a kernel with perovskite structure, whose lattice is rotate by 18.43° with respect to the a and b-axis of the SBN lattice, as indicated in fig.4.31.
- oxygen octahedra chains with the periodicity 0.395nm, along the c axis.
- a layered structure (fig. 4.30) with one (Sr,Ba)O layer and one NbO layer along the c-axis.

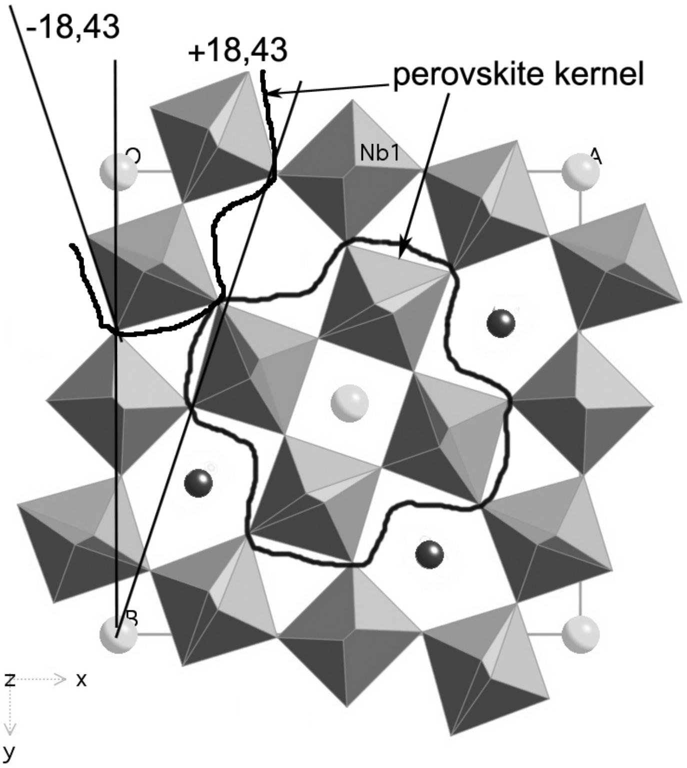

Figure 4.31: SBN unit cell: the perovskite kernel is indicated. These perovskite kernels can be divided in to two groups depending on how they are rotated with respect to the SBN lattice: one is rotate by 18.4° to the left, the other is rotate by 18.4° to the right. In the figure the first is indicted by the sign "-" the second by the sign "+".

In the case of (001) oriented SBN, the analysis of lattice matching reveals that in both growth modes (in plane and out of plane polar axis) the particular orientation realized, minimize the misfit between film and substrate. The misfit between SBN(001) and STO(100) is calculated comparing three unit cell of STO with one unit cell of SBN. In the case of parallel [100] axis, it is about 6.4%. The observed rotation of 18.4° reduces it to about 1%. For the SBN(310) oriented both the misfit along the c axis and perpendicularly to it (with the tilt of SBN$< 001 >$ by 18.4° and comparing three unit STO unit cell with one of SBN) are about 1%. Thus lattice mismatch minimization could explain by itself the growth orientation. It is important to notice that the perovskite kernels in the SBN structure, belong to two sub groups. Each of them is rotated of 18.43° to the left or to the right with respect to the a-b axis of the SBN unit cell, see fig. 4.31. The existence of the two in-plane grain orientation in the growth of SBN(001) oriented is due to the existence of such a structure and most likely the film growth starts from this kernel that perfectly fit on the perovskite structure of STO. What remains to be explained is the mechanism by which the two STO(100) surface terminations, SrO and TiO_2, determine the (001) and (310) orientation of SBN. As the two layer of STO have the same lattice parameter we expect a determinant role of charge balancing. Most likely the SrO surface is less demanding from the charge balance point of view and "allows" SBN to grow along its easy direction perpendicular to the film plane. In this case, the STO surface plays the role of the $z = 1/2$ plane and the $z = 0$ plane of SBN with the basis of the NbO octahedra is nucleating. A TiO_2 STO terminating surface has incomplete oxygen octahedra, such a configuration is not stable in oxygen atmosphere and high temperature, the condition during the deposition. We can thus expect SBN to complete the octahedra, and to add the A-site ions. Allowing for some distortion the (310) plane can form a continuous layer of octahedra (fig. 4.33, 4.32). The octahedra chains in the (310) plane and direction perpendicular to $< 001 >$ are indicated in Fig. 4.32. They repeat them selves each 39.37. This is about ten times the STO unit cell, with a misfit of 1%. After ten times the SBN periodicity in the (310) plane, i.e. a hundred time the STO unit cell, i.e. 393.7, the misfit film-substrate is 3.9. Thus misfit can be compensated by introducing one additional octahedra, edge dislocation, each 40nm. 40nm is the average width of one rod-grain in (310) oriented SBN films, see fig. 4.10. We conclude that such a dislocation is energetically unfavorable and SBN prefers to stop growing in this direction.

In the case of SBN grown on STO(111), the (421) SBN's plane that grows parallel to the substrate surface coincide with the (111) plane of the perovskite kernel of the SBN lattice (see Fig.4.34). The perovskite kernel is ruling the growth in this case as well as in the preceding ones and the SBN film nucleates as a continuation of the substrate structure.

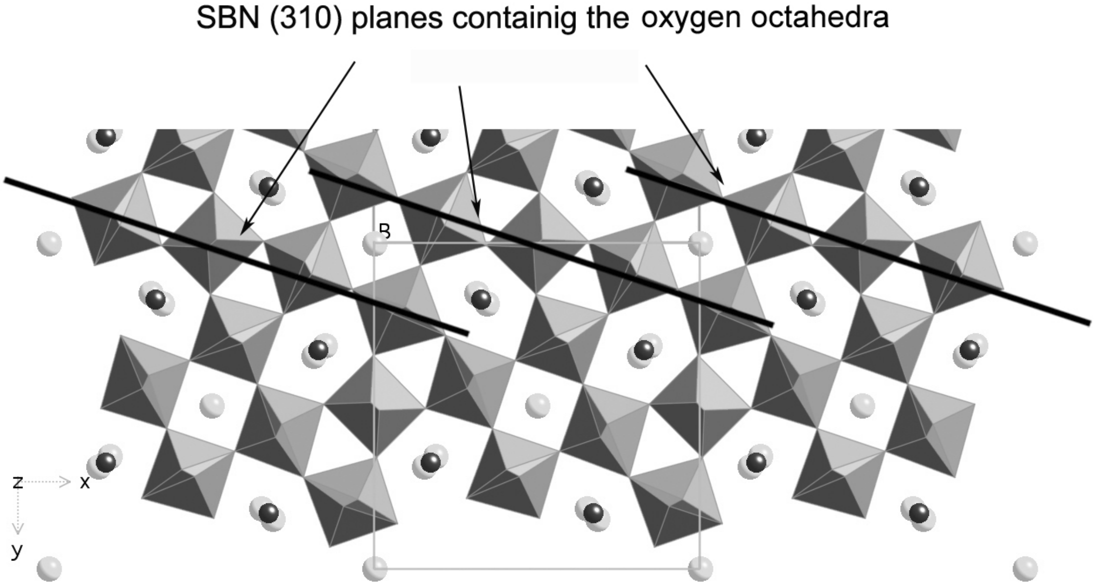

Figure 4.32: SBN (310) planes rich in oxygen octahedra. This plane are separated by one octahedra distance.

SBN growth on STO is clearly Wolmer-Weber type for all STO termination. High resolution TEM micrograph show as the TTB lattice of SBN accommodates on STO surface in a few atomic layers. Grain boundary start at the STO surface, no continuous layer, sign of Stranski-Krastanov growth, is visible. Defects in the film are mostly confined at the triple interface grain-grain-substrate, and due to irregularities in the STO surface.

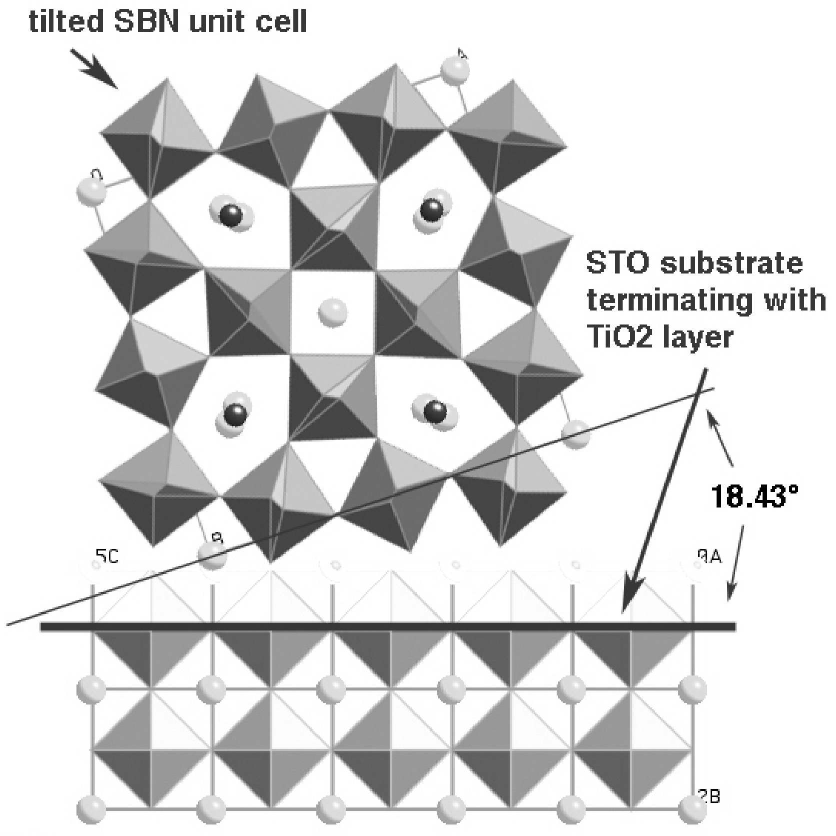

Figure 4.33: SBN unit cell growing (310) oriented on TiO_2 terminating STO substrate. The 18.43° tilt aligns the octahedra chains to the substrate surface. Allowing for some distortion of both substrate and film, the two crystals can join.

The parameter with the biggest influence on the film structure is temperature. At the temperature needed for the TTB structure formation, about 750°, atoms have a high mobility on the STO surface. This is confirmed by the growth of well spaced grains when enough time is given for them to coalesce (fig. 4.19). Diffusion distance is higher on STO(111) surface, here well defined and well spaced grains grow (421) oriented.
That means the bonding strength with the substrate is weaker than the internal TTB bonding, but strong enough to deeply condition the epitaxial relationship. The electrostatic energy is believed to be the driving force for the different orientations and oxygen octahedra as the building block unity. Would be interesting to verify if this can be considered as a general principle, testing the model on other complex oxides grown

on perovskite substrate.

It is known that SBN single crystals naturally grow along the [001] direction, the octahedra chains direction. This direction is clearly the preferred for the columnar grains of (001) oriented films. Following this tendency, rod shaped grains should grow with the [001] direction along the main axis of the grain. Unfortunately we could not give experimental evidence for this.

We have no experimental evidence that the slice shape of grains grown on (111)STO is due to growth along this direction either. However, there is only the natural anisotropy in the structure that can give rise to the platelets (slices).

The presence of one grain shape, corresponding to one orientation, on substrate where the other one is dominating, is due to imperfection of the substrate surface. In the case of non treated surface this is an expected effect because of the random presence of both STO terminations, for the wet-etched substrate the occurrence of (001) oriented grains can be due to a defective TiO_2 termination caused by imperfection in the etching process that should create the surface.

Is out of any doubt that the shape of the growing grains is determined by the STO surface. This gives evidence that it is possible to tailor grain shape and, more important, polar axis direction, by choosing the appropriate STO plane for their growth.

In order to improve the smoothness of films, atoms mobility should be suppressed, that has proven to be detrimental to the quality of epitaxy.

From results of this work together with literature results, it seems highly improbable that a monocrystalline SBN film could be obtained in heteroepitaxial growth.

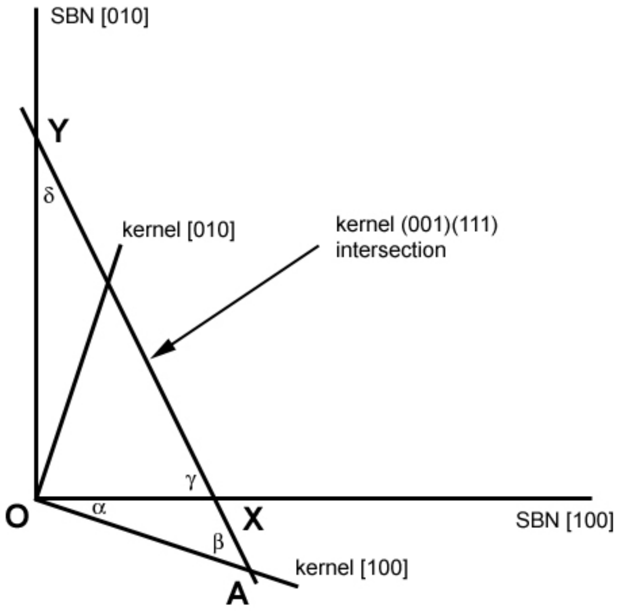

$$\beta = 45°$$

$$\alpha = 18.43°$$

$$\gamma = \alpha + \beta$$

$$\delta = 90° - \gamma$$

$$\overline{OX} = \overline{OA}\frac{sin\beta}{\sin(180° - \alpha - \beta)}$$

$$\overline{OY}/\overline{OX} = \frac{\sin\gamma}{\sin\delta} = 2$$

Figure 4.34: The referring system of the perovskite kernel contained in the SBN lattice, has the [001] axis coincident with the [001] axis of SBN and the [100][010] axis rotated by $18.43°C$ with respect to the SBN's [100][010] axis, as shown in the schema. The intersection of the kernel's (111) plane with the (001) plane is a line that crosses the the SBN's [100] and [010] axis in the points indicated by X and Y. The ratio of the two segments OY and OX is 2. If we take $\overline{OA}$=3.95 then $\overline{OX} = 3.12$, i.e. one quarter of the SBN lattice parameter along [100] direction. The plane (111) of the kernel is thus the (421) plane of the SBN lattice.

Chapter 5

Functional properties of SBN thin films

5.1 Electric characterization

5.1.1 Measurement procedures

5.1.1.1 Dielectric constant and phase transition

For most application of ferroelectric materials the dielectric constant and dielectric loss are important practical parameters that provide a lot of information about the mechanism of electric polarization. Dielectric constant and losses can be obtained from measurements of the impedance of a capacitor filled with the material under study. When an electric field $E(V/m)$ is applied to an insulating material, an electric dipole is induced. The polarization state is described by the dielectric polarization $P(C/m^2)$. Its change is a function of the electric field given by:

$$\delta P = (\varepsilon_r - 1)\varepsilon_0 E \tag{5.1}$$

with ε_0 dielectric constant of vacuum and ε_r the relative dielectric constant of the material. Ferroelectric materials are characterized by high values of dielectric constant with $\varepsilon_r \gg 1$, therefore the dielectric polarization can be approximated by:

$$\delta P = \varepsilon_r \varepsilon_0 E \tag{5.2}$$

When an alternating sinusoidal field $E(t,\omega) = E_0 \sin \omega t$ of angular frequency ω is applied to a lossy dielectric, the polarization response is delayed so that one distinguishes the in phase, $P = \varepsilon' E_0 \sin \omega t$, and out of phase, $P = \varepsilon" E_0 \cos \omega t$, component of the induced polarization. In this case the dielectric constant is conveniently expressed in complex notation, using the Euler relation:

$$\exp j\omega t = \cos \omega t + j \sin \omega t$$

$$\epsilon_r(\omega) = \epsilon'(\omega) - j\epsilon"(\omega) \tag{5.3}$$

$\epsilon'(\omega)$ is the real part of the dielectric constant and $\epsilon"(\omega)$ the imaginary part representing the dielectric loss. $\tan\delta = \epsilon'(\omega)/\epsilon"(\omega)$ is more often used to express the loss.
The behavior of a dielectric in electric field is completely described by ϵ' and $\epsilon"$ or $\tan\delta = \epsilon'/\epsilon"$.
Dielectric properties have been measured with a HP 4284A precision LCR meter, assuming the sample to be the equivalent of a capacitor and a resistor in parallel. A sinusoidal electric field of 40 V/m amplitude is applied to the sample in the frequency range 100Hz-1MHz. Capacitance values and losses, in the form of $\tan\delta$, were measured. From their behavior as function of temperature, anomalies are detected and the phase transition temperature identified. The variable temperature measurements, in the interval $-150°C$ $230°C$, were performed in a Delta Chamber 9023. The temperature was measured by Pt thermocouple. The measurement procedure was software controlled. Capacitance-voltage (CV) curves were measured with the same instrument and the same exciting field.

5.1.1.2 Hysteresis loops

The ferroelectric polarization is a two value function of the applied field represented by the hysteresis loop. Important values characterizing the hysteresis loop are:

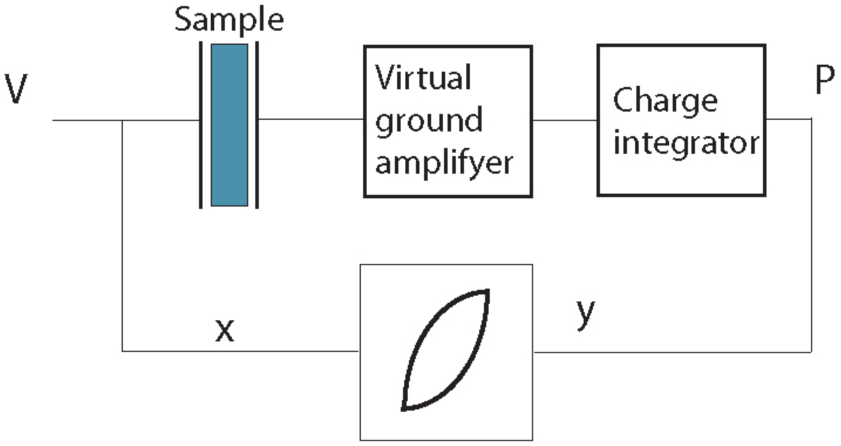

Figure 5.1: Diagram of the hysteresis loop measurement set-up

- the remanent polarization, left when the external electric field is reduced to zero
- the coercive field, necessary to bring the polarization to zero.

The existence of hysteresis, with two opposite values of remanent polarization, allows for the use of ferroelectric materials in memory applications. It is a bistable element that can be used to encode the 1 and 0 of Boolean algebra. The important parameters for memory applications are: the coercive field value, the remanent polarization value and their stability with time, temperature, and cycling.

Polarization hysteresis loops were measured applying an ac electric field of triangular waveform and 500 Hz frequency to the sample. The measurements were made in the virtual ground method: the electric field was applied to one electrode and the other one was connected to a virtual ground amplifier connected in turns to an integrator that collects the charges due to the variation of polarization of the sample. The integrated charges were plotted against the applied electric field.

5.1.1.3 Pyroelectric measurements

The pyroelectric effect is exhibited by all polar materials, thus by ferroelectrics as well, because the spontaneous polarization is a decreasing function of temperature. If the change in temperature is small and slow enough to keep the system at equilibrium, the pyroelectric coefficient is defined as:

$$p = \frac{\partial P_s}{\partial T}$$

and measured in $Cm^{-2}K^{-1}$. P_s is the component of remanent polarization perpendicular to the electrode planes, it can be measured by the variation of the charge density at the sample's surface.

Pyroelectric measurements were performed at 25° ÷ 27°C average temperature. Temperature variation where induced by a hot plate in triangular waveform of 10 mHz frequency and 1°C amplitude. Charges are collected at the electrodes, of area A, through a virtual ground amplifier with a calibrated resistor (R_f) in the feedback loop, and measured by a HP 3478A multimeter. The output voltage is related to the current i and to the pyroelectric coefficient p by the relation:

$$V = R_f i = R_f A p \frac{\partial T}{\partial t}$$

5.1.1.4 Atomic force microscopy

Single grain electric properties have been studied by piezoelectric force microscopy and conductive AFM. The measurement are performed in contact mode. A Pt-Ir coated AFM tip has been used as a mobile electrode to apply an electric field locally to the sample.

In conductive AFM, the force acting on the tip upon approaching the sample surface is used to control and maintain constant the tip-surface distance; the sample is grounded and a voltage is applied to the tip. Two different measurements are performed:

- a constant voltage is applied during the scan and both topography and current are measured at the same time.
- the surface is scanned to obtain a topographic image. From the information

obtained with this scan, specific sites at the surface are identified. Here, the tip is stopped and a voltage ramp applied. An I-V curve is then measured.

5.1.1.5 Piezoelectric effect

The piezoelectric effect is due to the bilinear coupling of elastic and electric variables.[141] Ferroelectric materials are a sub-class of piezoelectric materials and exhibit a linear dependence of the charge density at the surface on the applied stress. Hence, piezoelectric materials can be polarized by an applied stress. This is the direct piezoelectric effect. The linear relation between polarization **P** and stress **X** is written as:

$$P_i = d_{ijk} X_{jk}$$

where d_{ijk} is a third-rank tensor.
If an electric field is applied to a ferroelectric sample, it will deform. This is the converse piezoelectric effect. The linear relation between strain **x** and electric field **E** is written as:

$$x_{ij} = d_{kji} E_k$$

where d_{kji} is the same tensor as in the case of the direct effect.

Piezoelectric force microscopy is performed in contact mode. During the scan an ac voltage is applied to the tip or to the bottom electrode of the sample, while the other electrode is grounded. The piezoelectric sample deform in response to the electric excitation because of the converse piezoelectric effect. This induced vibration has the same frequency as the applied field and is transmitted to the AFM tip. In order to separate the piezoelectric response from other vibrations, the excitation frequency f_M is chosen well below the resonance of the AFM cantilever, and well above the scan frequency f_s. The latter condition decouples the piezoelectric response from the topographic response. In our experiment the electric excitation f_M has a frequency of 17kHz, a 1μ scan is performed in 2 sec. corresponding to a scan frequency f_s of 0.5 Hz. In this way, the probability of high frequency tip movement caused by topography, is strongly reduced. The piezoelectric signal from the tip is filtered by a lock-in amplifier, using the electric excitation frequency as reference, and the amplitude and phase are acquired. The amplitude gives information on the intensity of the piezoelectric effect, the phase gives information on the polarization direction. This method thus allows to visualize ferroelectric domains.

5.1.2 Sample preparation

500 nm thick SBN films have been prepared for electric characterization. A mask of positive photoresist was obtained by standard photolithography methods. Subsequently, a 100 nm thick film of gold or platinum was deposited by thermal evaporation in the first case and by sputtering in the second. Both depositions were performed at room temperature. Round top electrodes, with diameters in the range 10-200 μm were patterned by lift-off. An adhesion layer of 20 nm chromium was deposited before the gold. The platinum electrodes were annealed by RTA (rapid thermal annealing) at 500° for 5 min in oxygen to improve adhesion with the SBN film.

In order to contact the platinum bottom electrodes, the SBN film was etched to reach the metallic layer. For SBN films deposited on doped silicon and STO, the substrate acted as bottom electrode and the electric contact to the bottom of the sample is obtained by a layer of gold in the first case and gallium in the second. A schema of the capacitor is given in fig.5.2 while fig.5.3 is an image of the obtained electrodes.

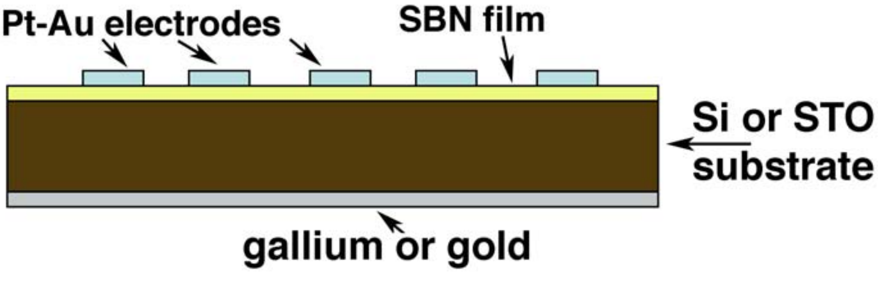

Figure 5.2: Schematic of the capacitors used for the electric measurements: gold or platinum are evaporated or sputtered on the SBN film trough a photoresist mask. The substrate, STO 1%Nb doped, act as electrode, the contact is effectuated trough a gallium layer.

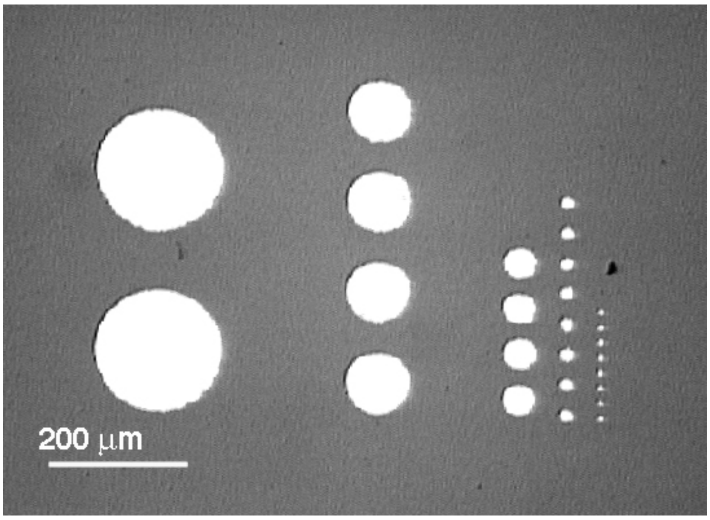

Figure 5.3: Electrodes obtained by photolithographic lift-off technique: diameters are 200, 100, 50, 20 and 10 μ m

5.2 Low purity SBN

5.2.1 Ceramic SBN50

A ceramic target has been fabricated by calcination and sintering, as described in Sect. 3.1, to obtain a sample with composition SBN50. The obtained density, 4.829 g/cm^3, is 90% of the theoretical one, the color is light brown. The measured $\theta - 2\theta$ X-ray spectrum is in agreement with the reference spectrum, fig.5.4, and has no apparent differences from the spectrum of an high purity sample, presented in Fig. 3.1. The composition has been double checked with XPS and X-ray fluorescence, both confirm the good composition within an error of 1% .

From dielectric constant measurements a phase transition is found around 0°C with a wide peak, about 160° FWHM, and frequency dispersion typical of relaxor behavior (fig.5.5). The maximum of dielectric constant is reached at a temperature about 120° lower than the one expected for SBN50 (see 1.3), the relative dielectric constant and loss at room temperature and 1kHz are respectively 2300 and 0.0023. As expected polarization as function of applied field does not have hysteresis at room temperature (Fig.5.6).

Despite the results of the chemical analysis we believe the ceramics contains impurities, the color is in fact totally different from those of subsequently sintered ceramic. The dielectric properties of deposited thin films support this hypothesis. Unfortunately we could not identify the source of contamination.

Lowering of the phase transition temperature is a phenomenon observed in SBN as well as in other relaxor ferroelectric materials, the cause can be found in different mechanisms. The effect of doping on SBN single crystals has been discussed in Sect.1.2.3.7 and summarized in Table 1.5. Lowering of the transition temperature is the common effect of doping, however the variation is usually much lower (a maximum of 50° for 1.6%wt Ce) than what we found in our ceramic. Differences in sintering temperature can be responsible for T_c variability as well,[29] but again in the order of few tenth of degree.

Effects of structural ordering and non stoichiometry on the relaxor-ferroelectric behavior has been studied for $Pb(Sc_{0.5}Ta_{0.5})O_3$[142] and $Pb(Sc_{0.5}Nb_{0.5})O_3$.[143] Non-stoichiometry in $Pb(Sc_{0.5}Ta_{0.5})O_3$, namely Pb vacancies, has a strong effect on dielectric properties and can lower the dielectric anomaly temperature of about 50° with respect to the stoichiometric ordered case.[142] These results confirm that, in general, the transition to a ferroelectric state is very sensitive to any disorder inducing factor. The reason of phase transition lowering in our case, remains an open question. However we believe it has to be found in multiple contamination coming from the low purity (98.5%) BaCO3 powder used for this sample. Contamination from this source are calculated to be 0.083%.

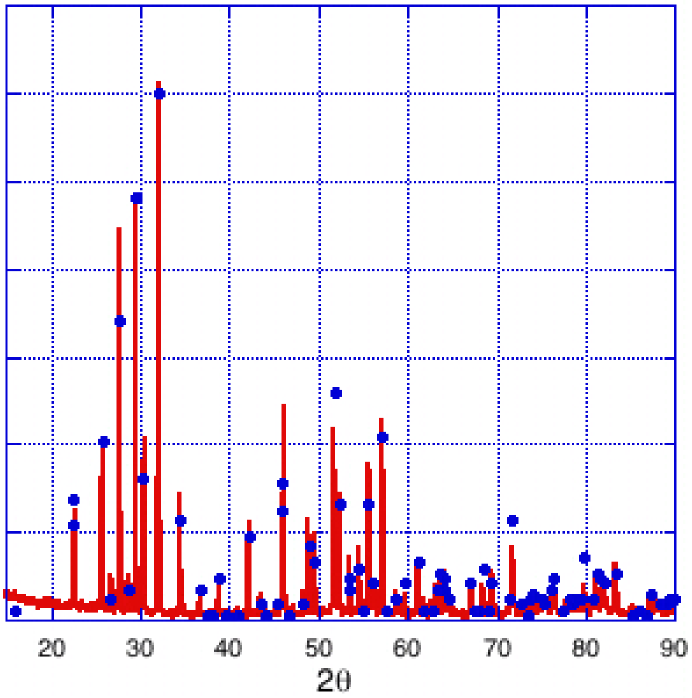

Figure 5.4: $\theta - 2\theta$ X-ray spectrum of SBN50 low purity ceramic target: Sr and Ba carbonate and Nb pentoxide calcined at 1100°C for 6h and sintered at1350°C for 12h.

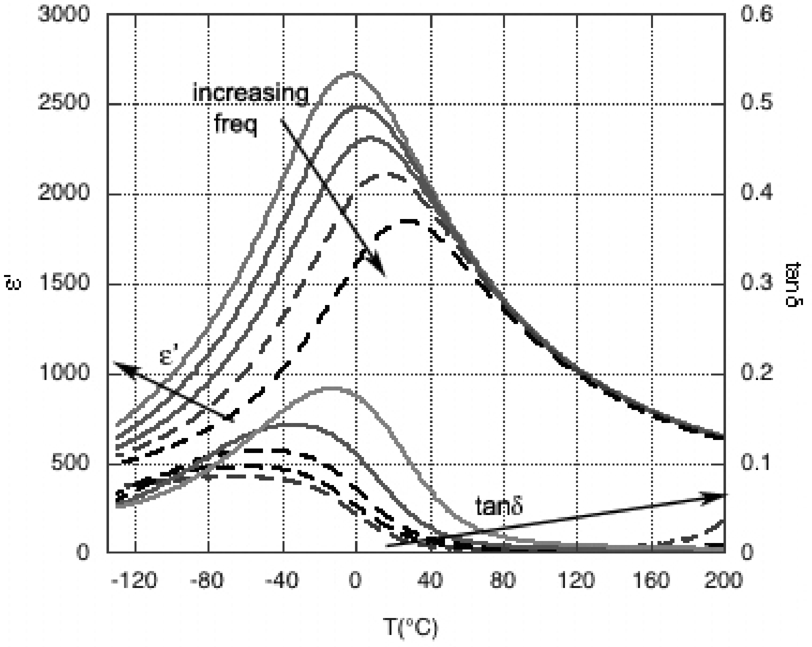

Figure 5.5: SBN50 ceramic: dielectric constant and losses as a function of temperature. Phase transition temperature is about 120° below the expected value and has a frequency dispersion typical of relaxor behavior.

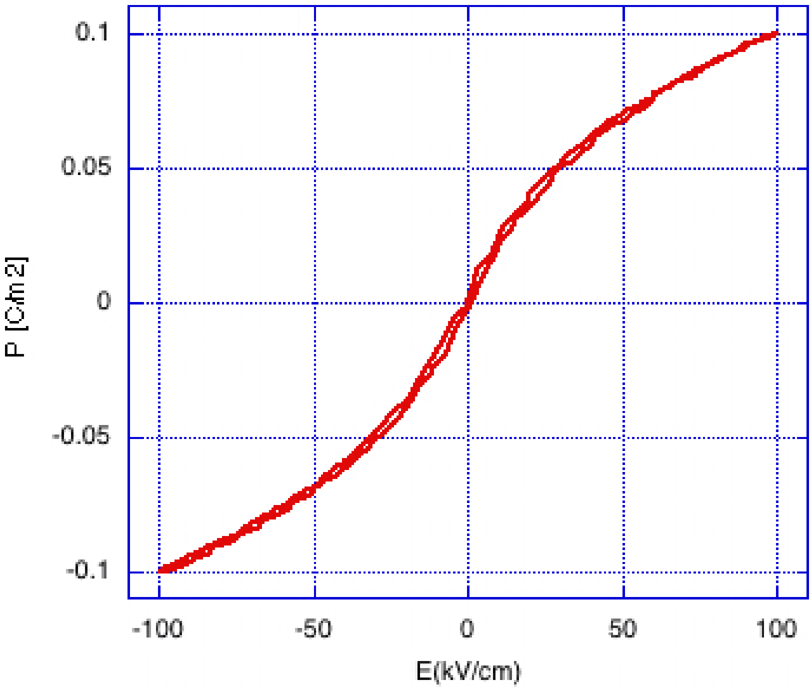

Figure 5.6: SBN50 ceramic: polarization as a function of applied field does not have hysteresis at room temperature.

5.2.2 Thin films

Thin films have been obtained from ablation of SBN50 and SBN60 targets and deposited on Pt(111)/Ta/Si and STO substrate as presented in the previous chapters. The measurements discussed in this section are from Pt/SBN50 and Pt/SBN60 samples, the first is (001) oriented, the second non oriented. STO/SBN60 (epitaxial growth) will be considered as well. We have found that the ratio Sr/Ba has little influence on the dielectric properties of the material, which are mainly defined by the substrate and the structure of the film.

5.2.2.1 Debye dielectric relaxation of oxygen vacancies

The dielectric constant measured at low field shows two anomalies with the same characteristic for both compositions, (figs.5.11, 5.14 and 5.17).

The anomaly at high temperature, about 120°C, has a broad frequency dispersion over a 100° interval, in both dielectric constant and losses. The exponential growth of losses above 120°C indicate the onset of conduction. Annealing in oxygen at 700°C (rapid thermal annealing, RTA) for 10 min, erase this anomaly, suggesting it is due to oxygen vacancies.

Dielectric anomalies with frequency dispersion in the temperature range $-100 \div 600$°C, were detected in various perovskites. Such anomalies are not related to the possible paraelectric-ferroelectric transition, but closely related to the oxygen vacancies.[144–146]

In the present case, supposing a Debye type dipolar relaxation where polarization occurs by a temperature-activated process, the dielectric constant is:

$$\begin{aligned}
\epsilon &= \epsilon_\infty + \frac{\epsilon_s - \epsilon_\infty}{1 + i\omega\tau} \\
\epsilon' &= \epsilon_\infty + \frac{\epsilon_s - \epsilon_\infty}{1 + \omega^2\tau^2} \\
\epsilon" &= \epsilon_s - \epsilon_\infty \frac{\omega\tau}{1 + \omega^2\tau^2}
\end{aligned}$$

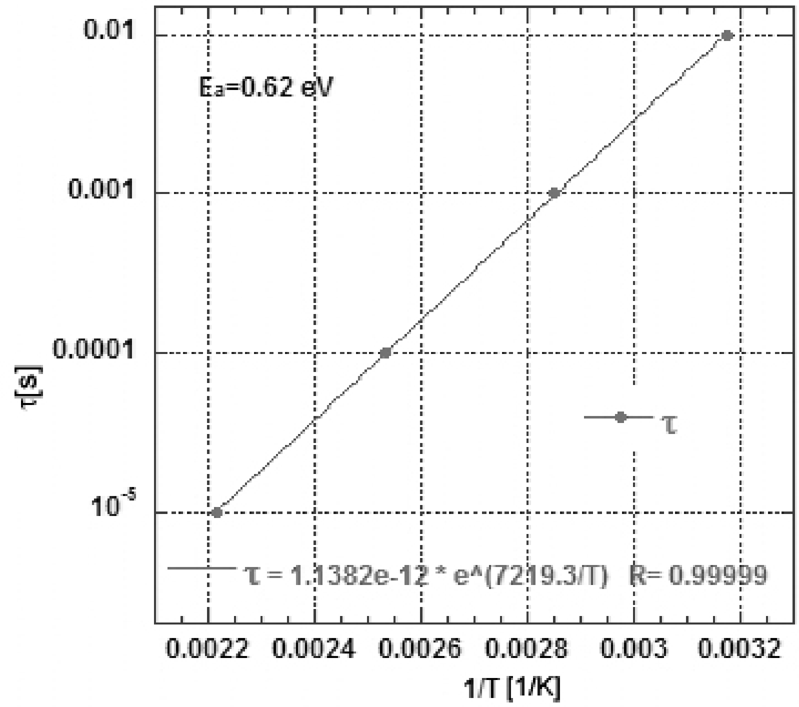

Figure 5.7: Arrhenius plot of Debye relaxation times. The fit with equation 5.4 give an activation energy of 0.64 eV.

the relaxation time τ depends on temperature following the Arrhenius law for thermal activation:

$$\tau = \tau_0 \exp(\frac{E_a}{kT}) \tag{5.4}$$

where k is the Boltzmann constant. The relaxation frequency τ^{-1}, is the frequency ω at which the imaginary part of the dielectric constant ϵ" is peaking, it is thus derived from the dielectric loss. The data yielded an activation energy of 0.64 eV. Similar activation energies[144]have been calculated for dielectric relaxation in Bi:STO, occurring at 80 $\div$ 380°C (0.63 $\div$ 0.66 eV), and attributed to the trap controlled ac conduction around doubly ionized oxygen vacancies.

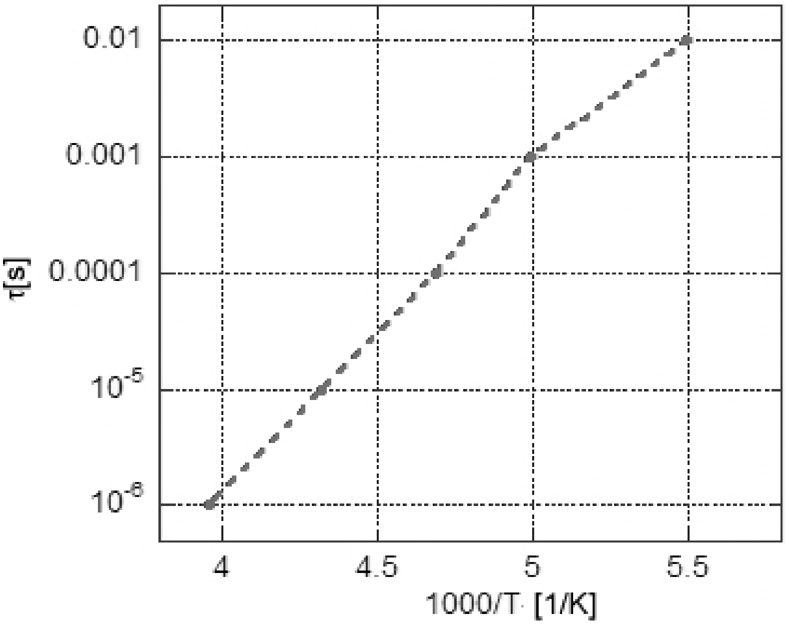

Figure 5.8: Arrhenius plot relative to the low temperature anomaly shown in Fig.5.11

5.2.2.2 Para to ferroelectric phase transition

Of the two dielectric anomalies, the one found at about −100°C, survives to the oxidation treatment (fig.5.14). The peak value of dielectric constant decrease from 750 to 530, this can be partially due to damaging of the top Pt electrode from annealing. The ensemble of the data on hysteresis discussed below, together with the frequency dispersion of the dielectric constant peak, allows us to identify the low temperature anomaly with a para to ferroelectric transition of relaxor type.

The Arrhenius plot of $(\log(1/\omega) vs. T_m)$ data relative to the low temperature anomaly does not deviate significatively from a linear dependence on 1/T (Fig. 5.8) (T_m = temperature of the dielectric peak at a given frequency), however, the value found for the attempt frequency ω_0 ($\omega_0 = 10^{-18}$) is to high to be attributed to ionic excitation process as can be seen in fig. 5.9. It is known[147,148] that the frequency dispersion of dielectric peak, in the case of relaxor behavior, is better described by the Vögel-Fulcher law 5.5 rather than by the Arrhenius law; in this law the relaxation frequency, ω_r,as

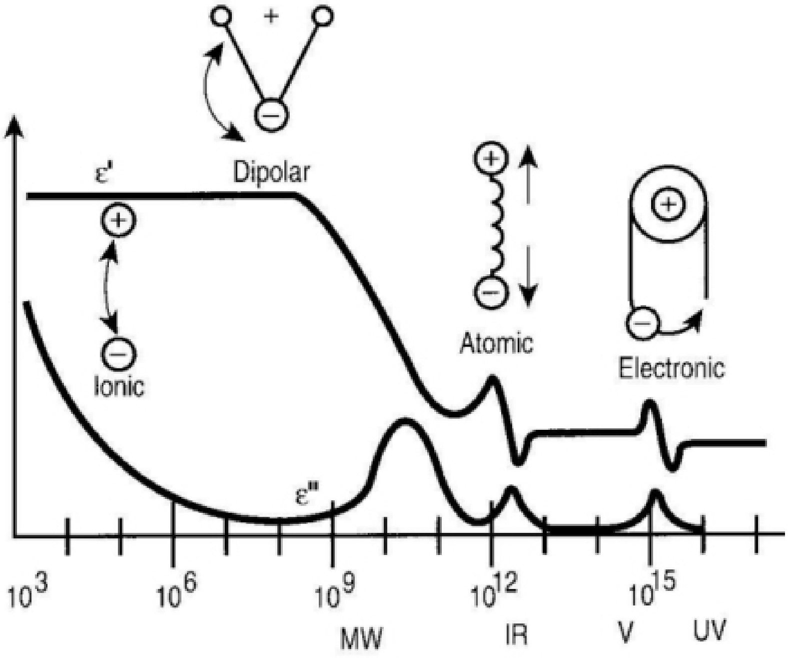

Figure 5.9: Real, ε', and imaginary, ε'', part of the dielectric constant as function of frequency for insulator materials. The physical processes responsible for the anomalies at the different frequencies are indicated.

ω_0	E_a/k	T_f
$3 \cdot 10^9 s^{-1}$	783K	156K

Table 5.1: Parameter from the modified Vogel-Fulcher fit to $\omega(T_m)$ data.

Ce content at.%	ω_0	E_a/k	T_f
0.0	$8 \pm 6 \cdot 10^8$	$160 \pm 40K$	$347 \pm 3K$
0.0066	$8 \pm 5 \cdot 10^9$	$368 \pm 49K$	$320 \pm 2K$

Table 5.2: Parameter of the Vogel-Fulcher fit from ref.[150]

function of temperature is given by:

$$\omega_r = \omega_0 \exp(-\frac{E_a}{k(T - T_f)}) \tag{5.5}$$

$$\tag{5.6}$$

where ω_0 is the attempt frequency and T_f the freezing temperature. A modification of Vögel-Fulcher law, linking the measurement frequency ω to the dielectric constant peak temperature T_m (5.7), has been introduced,[147] which can be applied to both real and imaginary part of the dielectric constant[149] :

$$\omega = \omega_0 \exp(-\frac{E_a}{k(T_m - T_f)}) \tag{5.7}$$

$$\tag{5.8}$$

Fitting our data with this law (Fig.5.10) gives for the parameters, the values reported in Tab.5.1.

In tab.5.2 are reported the fitting parameters of pure and Ce doped SBN61 data to the Vögel-Fulcher from ref.[150] It is seen how the introduction of dopant increases the activation energy E_a probably due to the enhancement of charge disorder. In the case of our films the effect is of higher intensity, in accordance with greater lowering of the critical temperature and supporting the hypothesis of higher impurities content. The value of the attempt frequency found for our films is of the same order of magnitude than the one relative to the Ce doped single crystal.

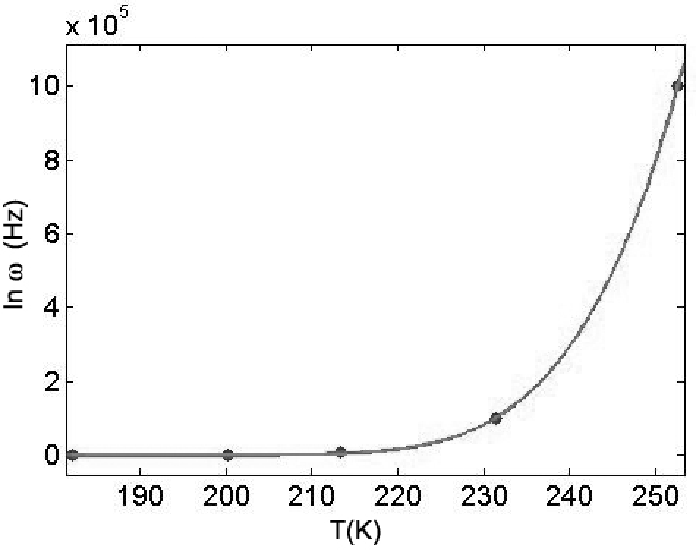

Figure 5.10: Vogel-Fulcher fit to $\omega(T_m)$ data

5.2.2.3 High field characterization: hysteresis loops

Polarization measured as function of applied electric field at room temperature, on Pt/SBN, clearly suffer from leakage, most probably originating from oxygen vacancies, (fig.5.12). At low temperature, below the critical temperature, hysteretic behavior ($-150 \div -170°C$) is well defined in the oriented samples. The loop has a coercive field of $20kV/cm$ and saturation polarization of $13\mu C/cm^2$, fig.5.13. Oxidation treatment has been detrimental to the sample, the bottom electrode got damaged by delamination from the silicon support.

The as deposited SBN60 non oriented sample is even more affected by leakage and polarization curve of the as deposited films were possible at low temperature only, (fig.5.15). This film has been successfully post annealed in oxygen. Leakage at room temperature is suppressed and polarization has no hysteresis, at −170°C hysteresis start to manifest but the coercive field and the remanent polarization are much lower than in the ordered film case (fig.5.16).

Qualitatively similar properties have been found for SBN60 grown on STO single crystal, however the transition temperature (about −10°C) is higher of about 70°C than in the case of Pt substrate (fig.5.19). Polarization hysteresis is present at room temperature (Fig.5.18), these loops attest for ferroelectricity above Tm. Non zero local spontaneous polarization above the dielectric peak temperature have been calculated in SBN single crystals and other relaxor, from measured optical properties.[27,151] Direct measurement of polarization revealed the same.[152,153] Field cooling of SBN has been proven to enhance polarization at high temperature and to induce a memory behavior in SBN.[26]

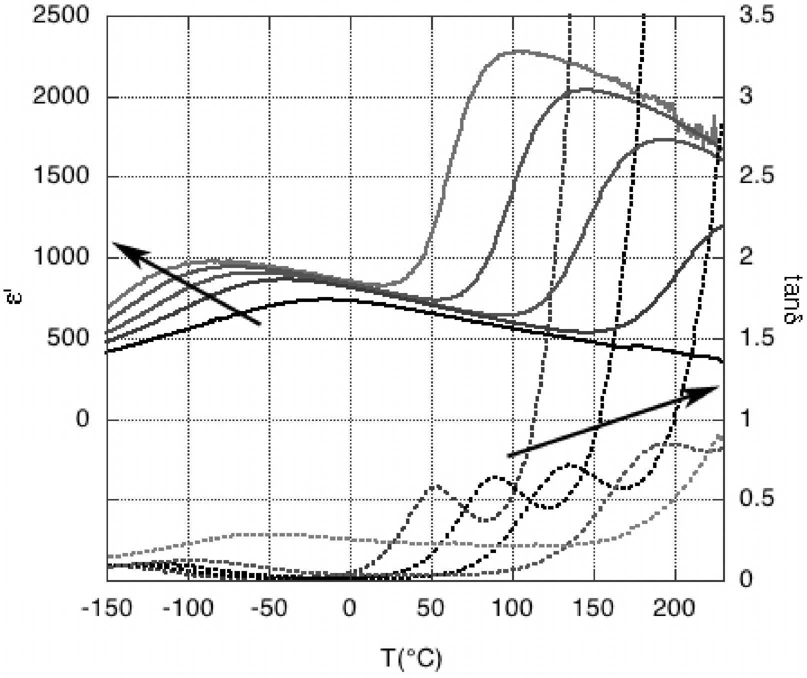

Figure 5.11: As deposited SBN50, grown on oxidized Ta/Pt: dielectric constant and losses as function of temperature. Phase transition temperature is about 220° below the expected value.

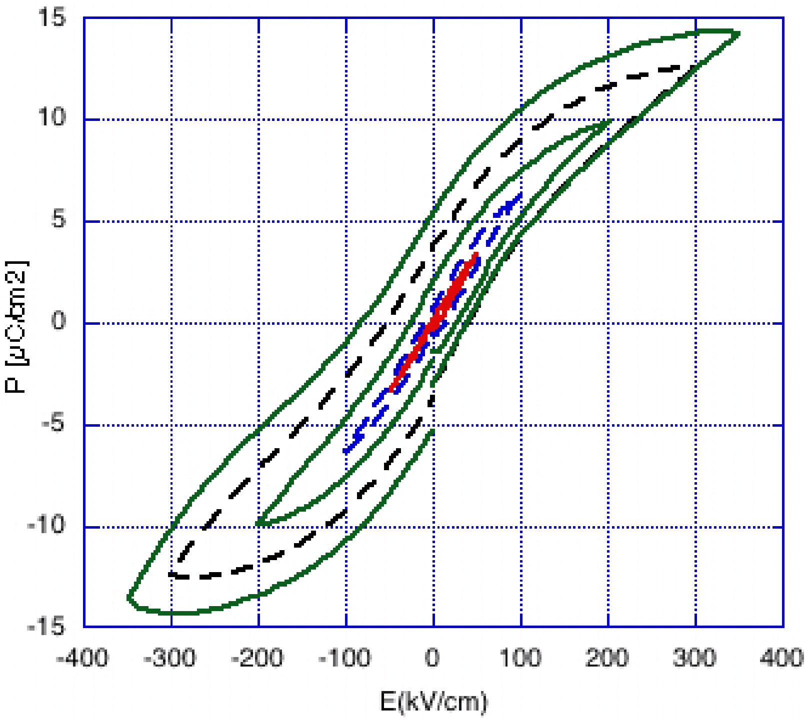

Figure 5.12: As deposited SBN50 grown on oxidized Ta/Pt: hysteresis loop at room temperature.

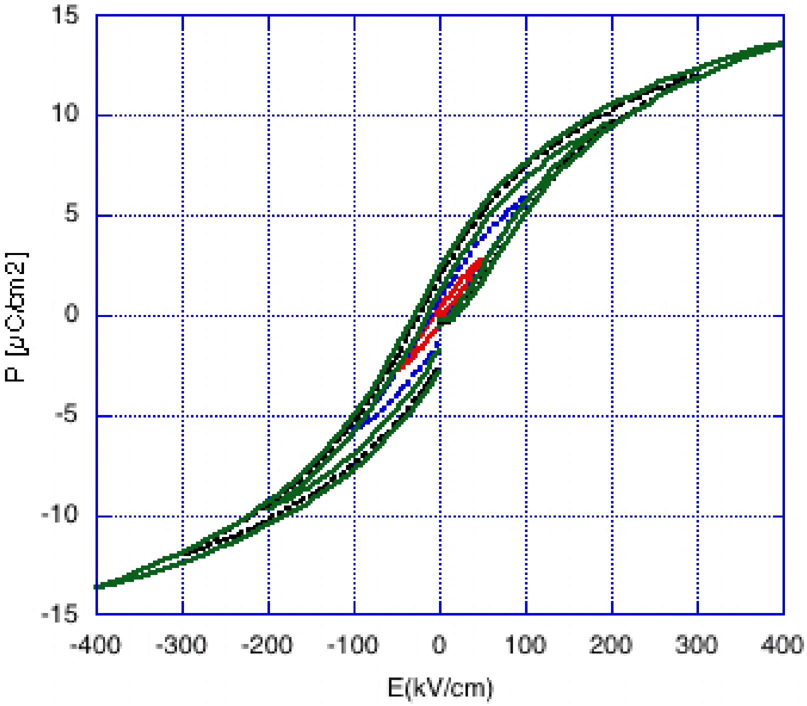

Figure 5.13: As deposited SBN50 grown on oxidized Ta/Pt: hysteresis loop at −150°C, below the phase transition temperature.

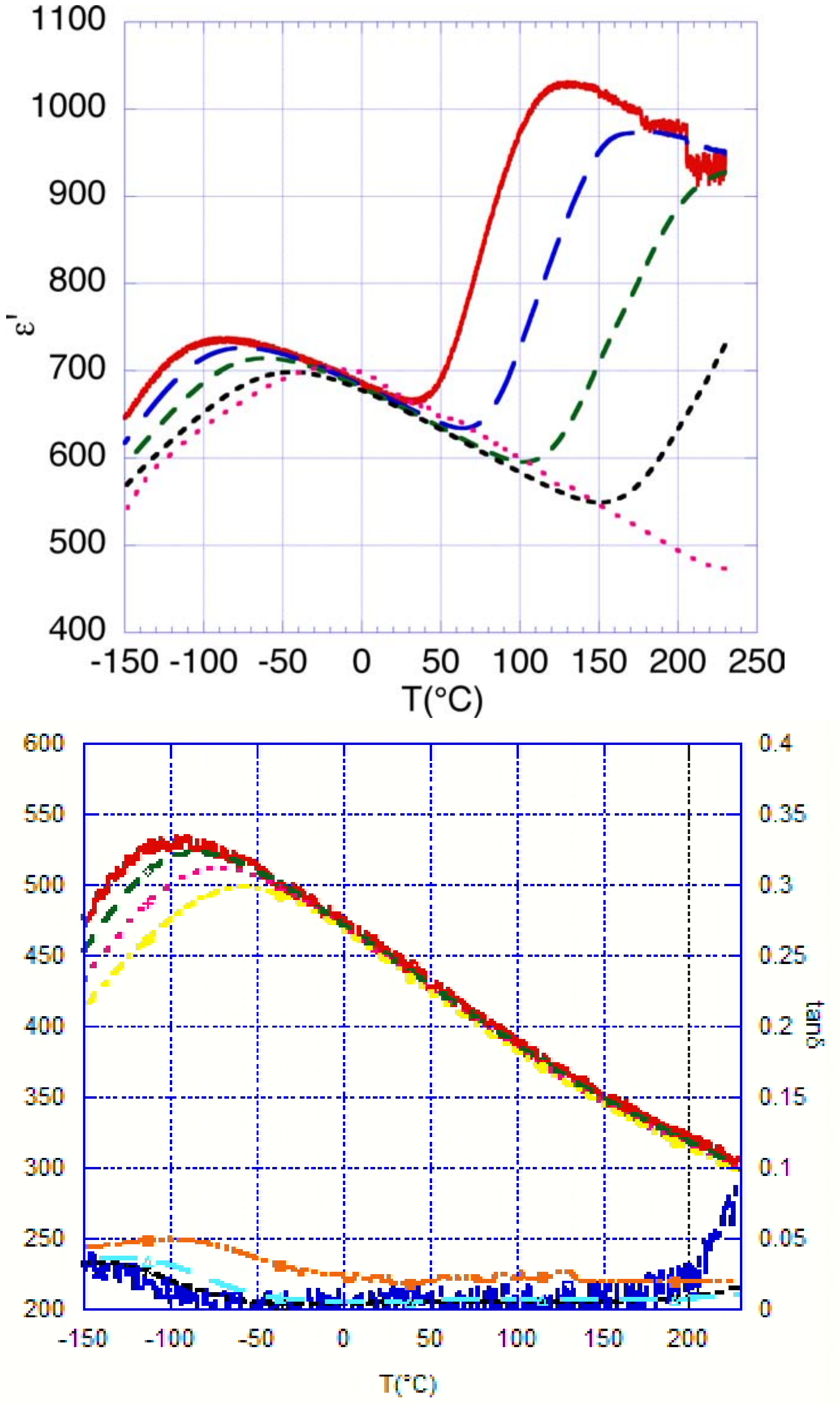

Figure 5.14: SBN60 grown on Ta/Pt oxidized: dielectric constant before (top) and after annealing (bottom) at 700°C in oxygen.

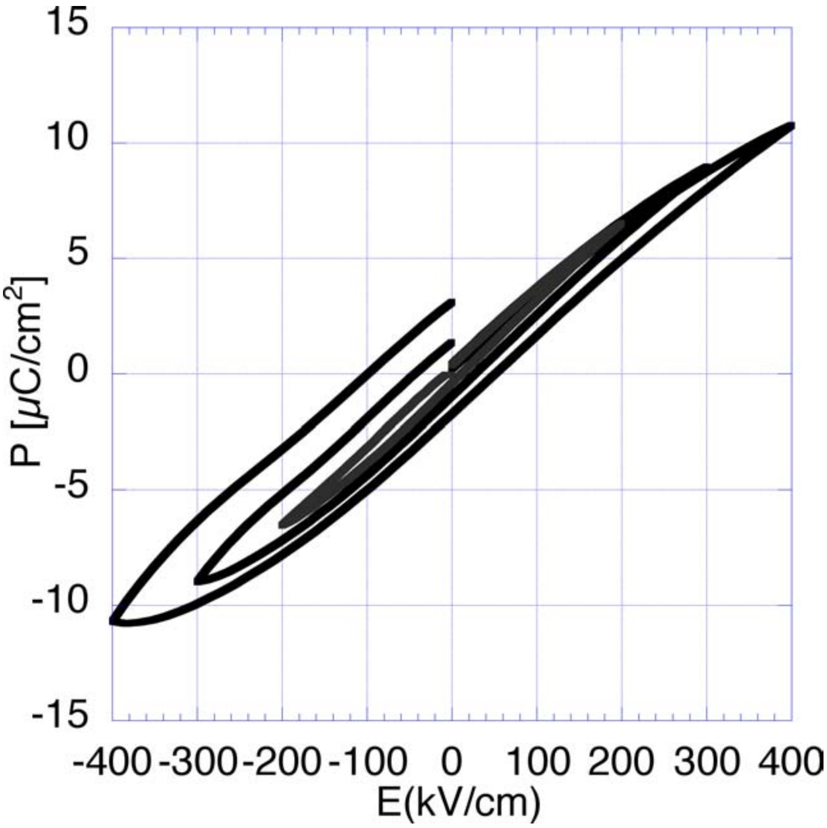

Figure 5.15: As deposited SBN60 grown on oxidized Ta/Pt: hysteresis loop at −150°C, below the phase transition temperature.

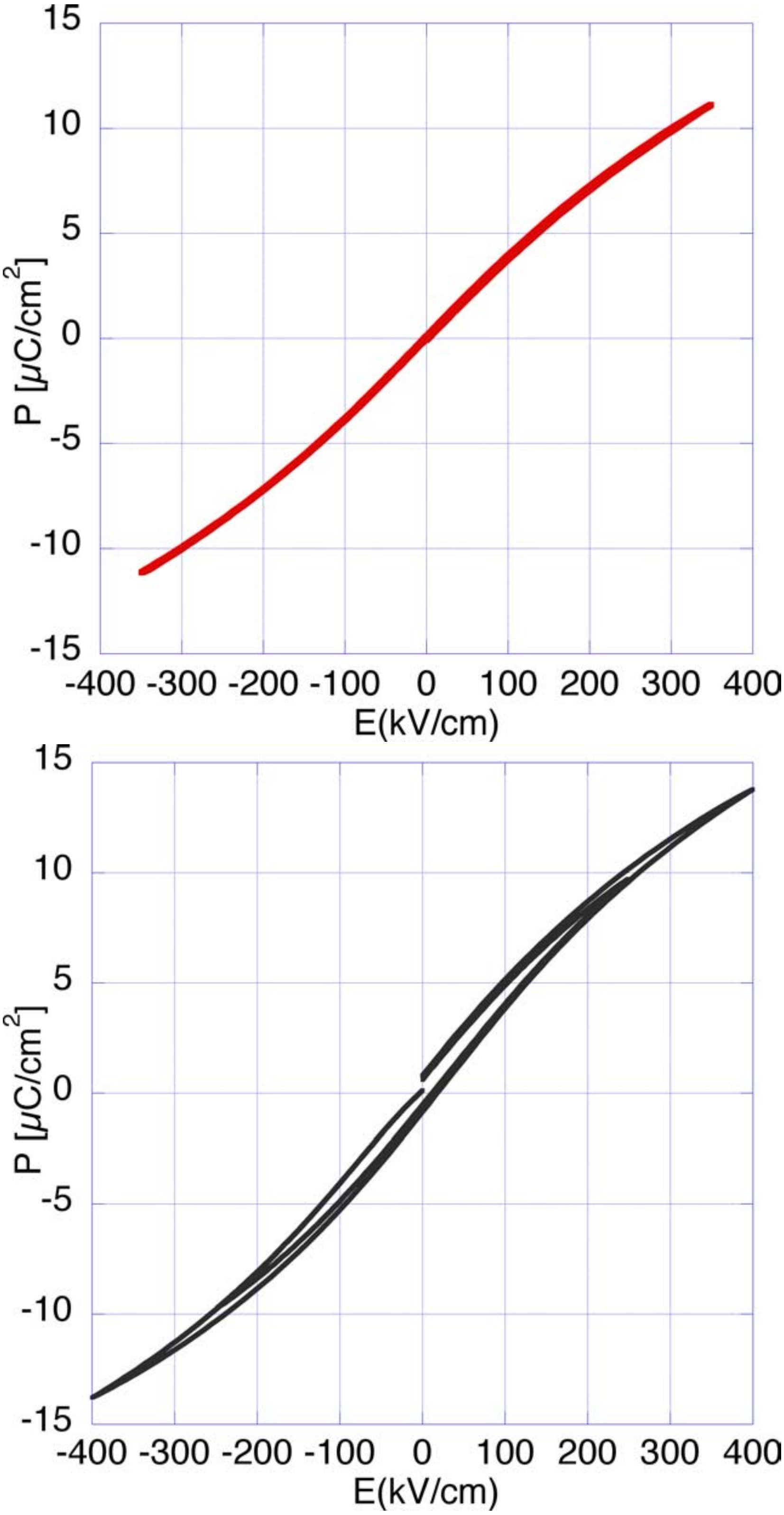

Figure 5.16: SBN60 grown on Ta/Pt oxidized: (top) hysteresis loops at room temperature and (bottom) at -170°C.

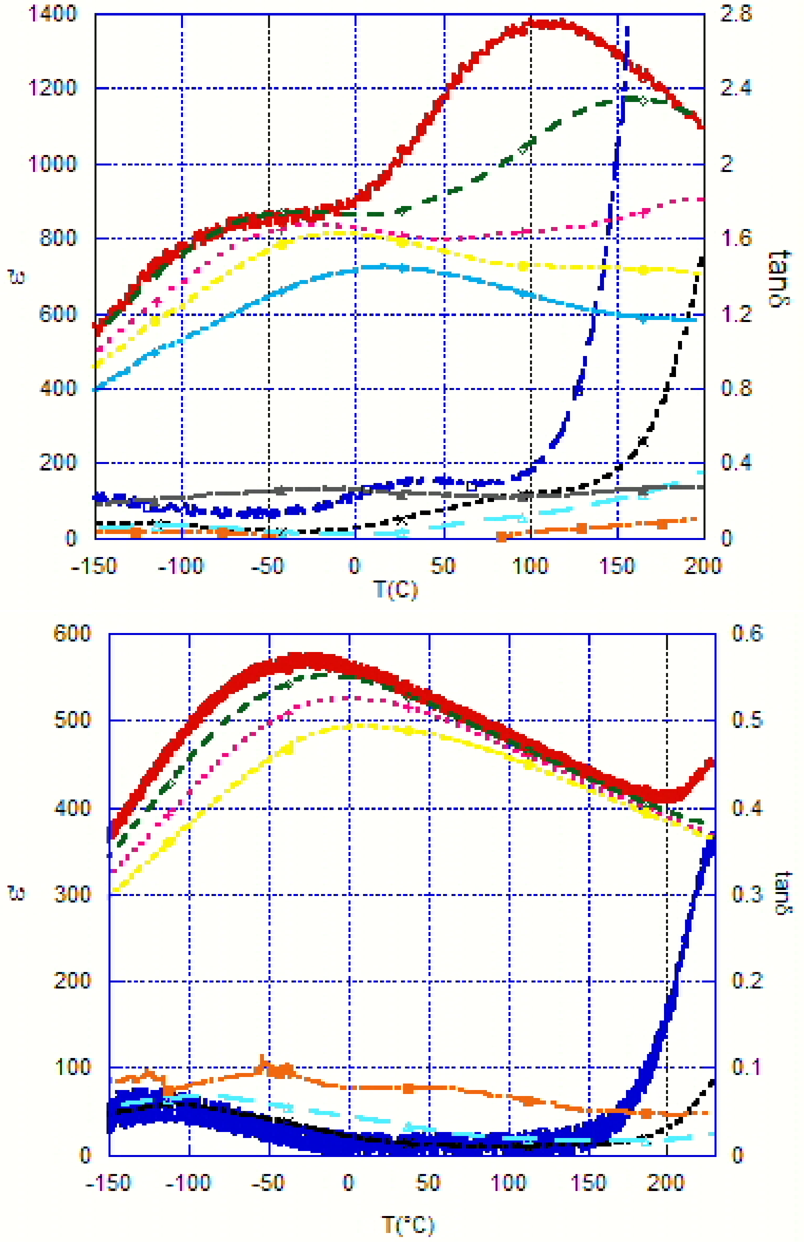

Figure 5.17: (001) oriented SBN60, grown on STO 1%Nb-doped single crstal:dielectric constant and losses as function of temperature of (top)the as grown film AND (bottom)after annealing in oxygen at 700°C.

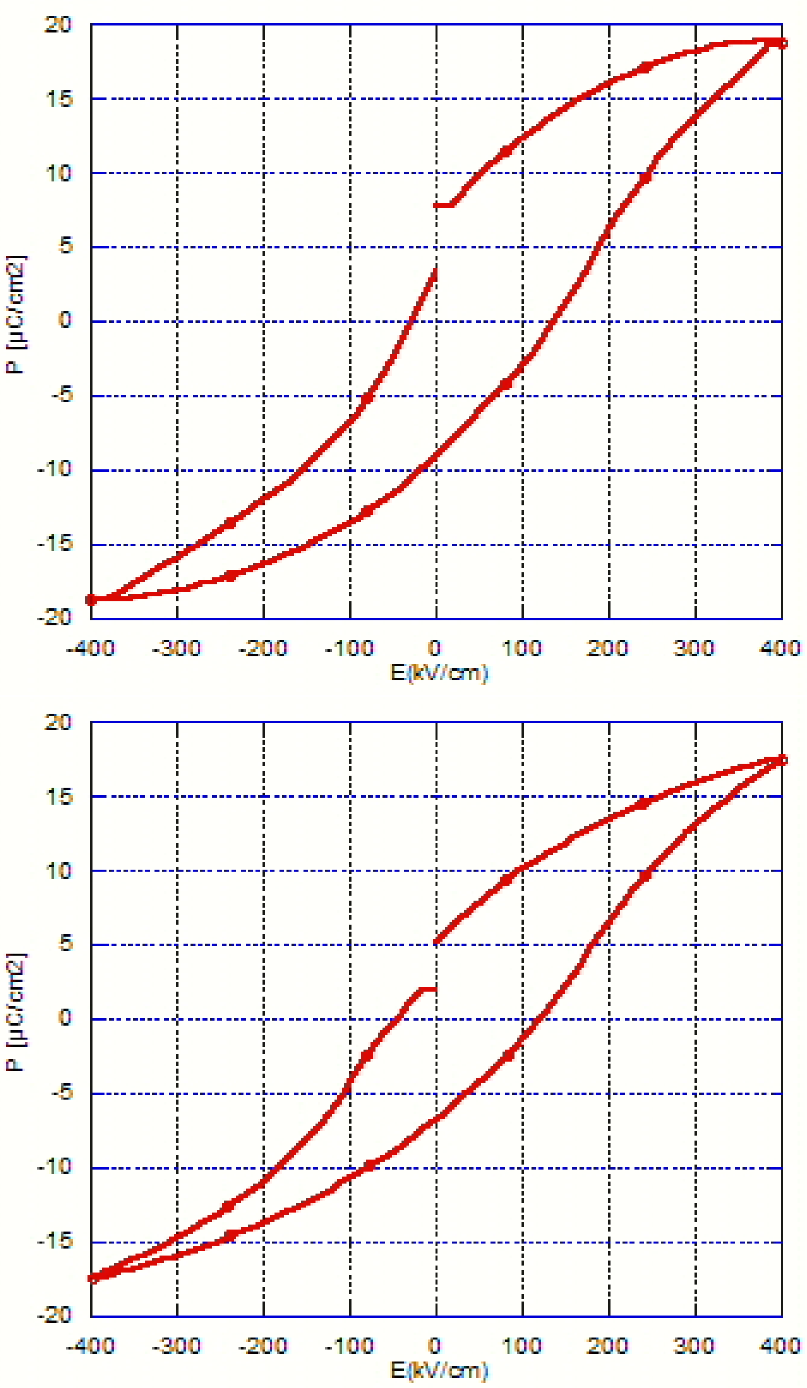

Figure 5.18: (001) SBN60 grown on STO single crystal: room temperature hysteresis loops of the as grown film (top) and after annealing in oxygen at 700°C (bottom).

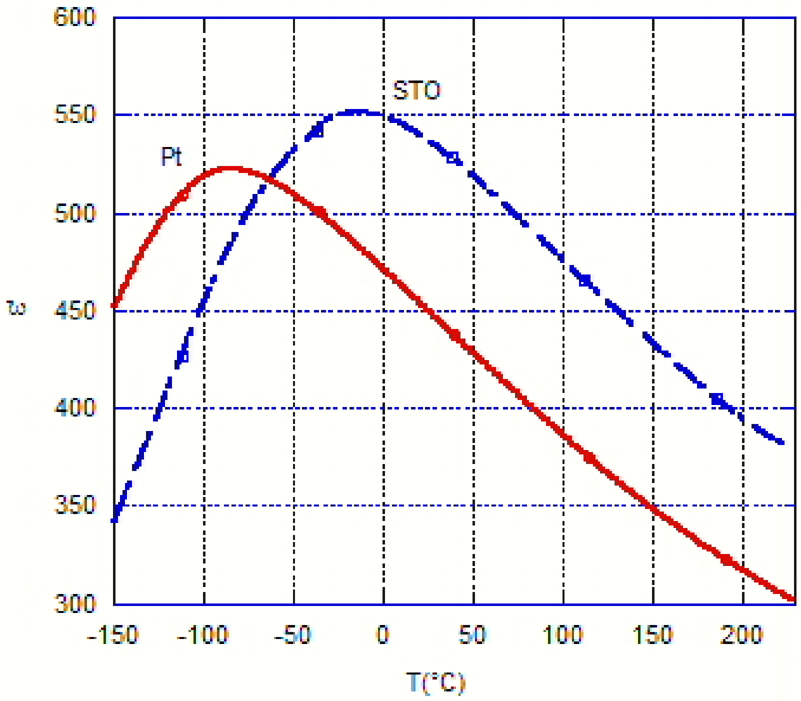

Figure 5.19: Dielectric constant as function of temperature of SBN60 grown on Pt/Ta/Si and STO substrate.

5.2.2.4 Effect of stress on SBN phase transition

The influence of the substrate induced stress on the behavior of SBN phase transition can be evaluated with the help of the Landau Ginzburg Devonshire theory as outlined in the introduction. An estimation of the effect of stress on SBN can be obtained by Eq.(1.12), p.26. The thermodynamic parameters, relative to SBN60, used for calculation are listed in tab.5.3 In the present case, the film is thick enough (about 500nm) to relax the stress, during the growth process, by formation of dislocations (see page 69) The presence of grains helps in the process of relaxation. However another source of strain is the thermal expansion. We can suppose that below a certain temperature dislocation formation is inhibited. At that moment differences in thermal expansion between film and substrate induce a strain that can not relax anymore.

$P_s C/m^2$	C $°C$	T_C $°C$	$Q_{13} m^4/C^2$	ϵ_0 F/m	ϵ_r	$s_{11} + s_{12} \cdot 10^{-12} m^2/N$
0.25	2 10^5	80	$-0.7 \cdot 10^{-2}$	$8.854 \cdot 10^{-12}$	470	3.86

Table 5.3: Saturation polarization P_s, Curie constant C,[47] phase transition temperature T_C, electrostrictive constant Q_{13},[27] dielectric constant of vacuum ϵ_0 and relative dielectric constant of SBN60. Room temperature values.

	SBN60	Silicon	STO
K^{-1}	$15 \cdot 10^{-6}$	$2.6 \cdot 10^{-6}$	$10.4 \cdot 10^{-6}$

Table 5.4: Linear thermal expansion coefficients of SBN60, Silicon and STO.

The in plane strain, S, due to thermal expansion, is given by:

$$S = (\alpha_{SBN} - \alpha_{sub})\Delta T \tag{5.9}$$

where α_{SBN} and α_{sub} are the thermal expansion of SBN and substrate respectively. Thermal expansion coefficients are listed in tab. 5.4 and considered to be constant in the temperature range of interest. We estimate relaxation by defect creation does not occurs anymore below 600-550°C. On both substrates SBN undergoes a tensile strain. Calculation with Eq. 5.9, considering $\Delta T = 500$, give a strain of 0.6% in the case of Si and 0.2% in the case of STO.

The temperature shift has been evaluated with Eq.(1.12), p.26. For a 0.6% tensile strain it is found to be in the interval $100 \pm 50°$ C and negative. The measured difference in phase transition temperature between the film deposited on STO substrate, the one deposited on single crystal silicon and the ceramic samples, can thus be interpreted as due to such a stress.

5.2.3 Discussion

The dielectric behavior of the as grown samples is indicating the presence of oxygen vacancies that can be removed by post annealing in oxygen at 700°C. Such a procedure is a common one for oxygen vacancy recovery in other ferroelectric materials.

The dielectric anomaly at low temperature has been identified as the transition from para to ferroelectric phase and the presence of impurities as the cause of temperature lowering respect to expected for the nominal composition (SBN50 120°C, SBN60 80°C). The phase transition has a strong relaxor character (frequency dispersion of the dielectric constant peak) even in SBN50. This composition is known to be purely ferroelectric in single crystal SBN and the relaxor behavior in our films is most likely due to the impurities.

Chemical analysis has been carried out on both target and films giving the same results, thus assuring the level of impurities is not higher than 1% at. As the source of contamination has not been identified, we can not exclude the presence of different elements. It is known that the combination of different dopant is more effective in both lowering the transition temperature and enhancing the relaxor behavior of SBN.[43]

The substrate has a strong effect on the dielectric properties of the film as proven by the different temperatures of the phase transition. While the film grown on STO has a behavior compatible with the bulk ceramic used as target, in the film grown on Pt the ferroelectric transition is manifesting at a much lower temperature. We believe the cause has to be found in the stress induced by the thermal expansion mismatch.

5.3 Characterization of high purity SBN/STO 1%Nb films

The films, whose properties will be discussed in this section, are grown from a different SBN50 target. X-ray diffraction patterns of this ceramic are shown in fig.3.1 at pg.46. A single anomaly is observed at about 120°C in the temperature dependence of the dielectric constant,(e.g. Fig. 5.33 page 149). Although leakage is strong at temperatures higher than 100°C, the anomaly at 120°C can be identified as the para-ferroelectric phase transition. The transition temperature thus corresponds to the expected value for such a composition in the single crystal case.

Growth of SBN on STO single crystals is epitaxial and dominated by the effect of substrate surface as seen in details in the previous chapter. In the following properties of pure (001) oriented, mixed (001)(310) oriented and (421)oriented films are analyzed.

5.3.1 Conduction trough the film

Leakage has been a major problem encountered during the characterization of SBN films grown on STO. As deposited, the films are affected by high losses which can be reduced by annealing in oxygen. Leakage and conduction can be attributed to oxygen vacancies formed during film growth. However high field conduction is enhanced by annealing of the top electrodes (see Sect.5.3.3).

Figure 5.20 shows the topography and current image taken from an as deposited film. The surface morphology is well recognizable in the current image and is in agreement with the topographic image. The current is in the interval 0.1-0.5 nA for 2V applied to the AFM tip, it increases to few 5-10 nA for 5V; the maximum is detected at the grain boundary. Annealing in oxygen effectively reduces the conduction through the sample from nA to pA as shown in fig.5.21 where a voltage of 10V applied to the tip has been necessary in order to obtain the image.

I-V curves (fig.5.22) evidence that conduction is one order of magnitude more intense in the rod shaped grains, where the polar axis lies in the film plane, than in the columnar grains with the polarization axis perpendicular to the film plane. Fig.5.23 shows I-V curves after annealing; conduction is the same in the two grain type,with intensity strongly reduced. The strong current reduction upon annealing in oxygen is an indication of the fact that conduction is due to oxygen vacancies. Such a conduction is strongly anisotropic and the movement of vacancies is easier in the direction perpendicular to the polar axis. This means conduction does not occurs along the octahedra chains but rather in the planes perpendicular to them. The Nb-O plane (the plane indicated as z=0 in fig.4.30) are the more dense in oxygen content, i.e. the ones with the smallest interatomic distance, therefore we can expect these are the ones where the mobility is facilitated. Once the vacancies responsible for conduction are removed, the strong anisotropy in conduction is logically expected to disappear as well, as actually does.

From the current profile of fig.5.21 a "hole" is seen (indicated by the bars), 15 nm wide, that can be related to the tip shape (tip radius= 15nm, as from technical specifications). In the topographic image, in fact, there is a corresponding cavity formed by four meeting grains perpendicular to each other. Other "holes" are visible in the current profile which can not be directly related to the topography; we could argue that the current measurement is more sensitive than the force ones, and actual electric properties of the sample are giving a contribution to the signal together with the topography. The interpretation is complicated by the fact that the measured current value is very close to the resolution of the measurement, $15 \cdot 10^{-4} nA$. What is important to notice here is the close resemblance of the current and topography measurement, and the fact that the tip dimensions constitute a limit in the resolution because close to the topographic features. For these reasons we believe that the higher current measured at the grain boundary has to be interpreted as an artifact due to the convolution of tip shape (radius of curvature about 15 nm) and film morphology rather than to a locally higher current density. Where the profile is steeper the tip-film surface of contact is wider and consequently the current signal stronger. Therefore the current measurements do not prove that grains boundary are easy path for conduction but do not exclude it either. The resolution is not good enough to inspect the boundary. What is clearly seen is that the bulk of grains is affected by conduction due to oxygen vacancies, removed by thermal treatment in oxygen atmosphere. Therefore post annealing leakage is unlikely to be due to conduction trough the grains.

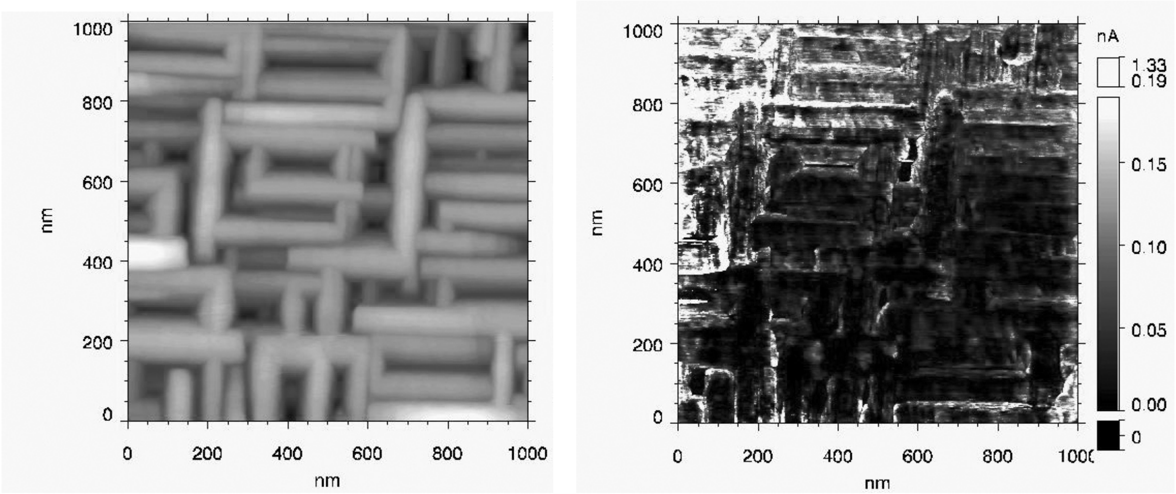

a) b)

Figure 5.20: As deposited SBN film a) AFM topographic image of the surface, b) current image with 1V applied at the tip. The conductive substrate is grounded.

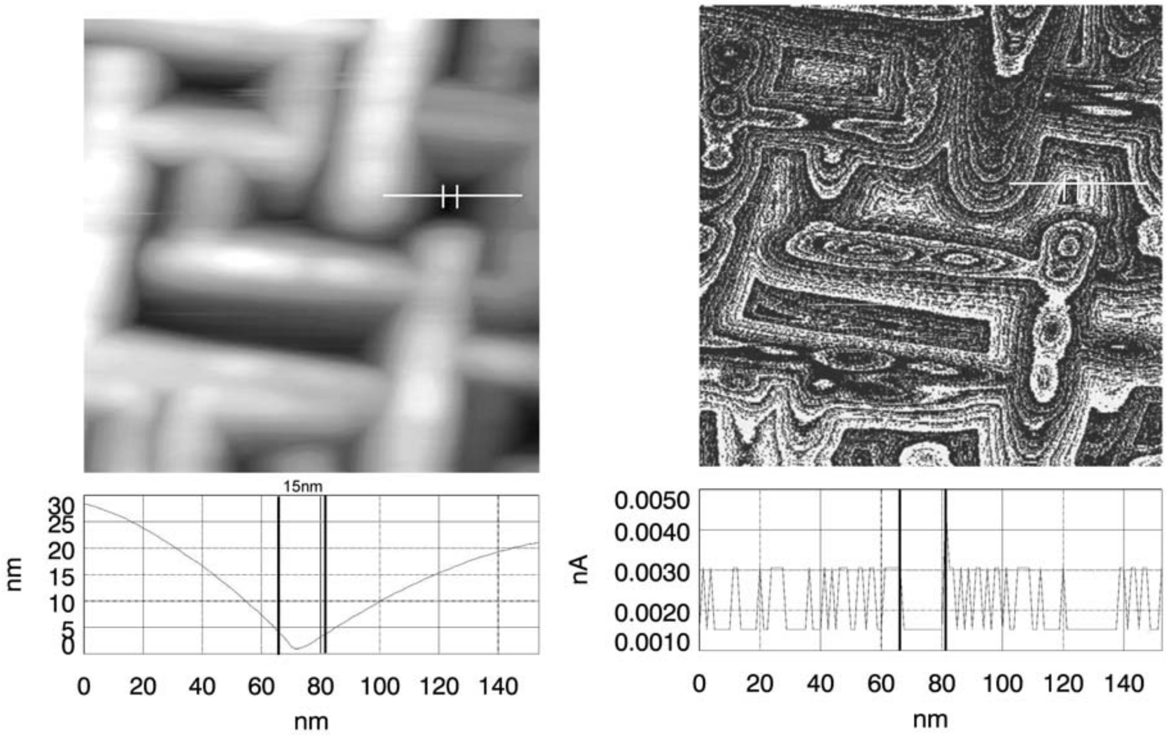

a) b)

Figure 5.21: Annealed SBN film: a) AFM topographic image of the surface, b) current image with 10V applied at the tip. The conductive substrate is grounded. In the lower part of the images, the profile of: a) topography and b) current, corresponding to a grain boundary is shown. The current resolution is $15 \cdot 10^{-4} nA$. The lateral resolution of the profiles is 1.25 nm and the tip radius 15nm. The higher current measured at the grain boundary is due to the convolution of tip shape and film topography rather than to locally higher current density.

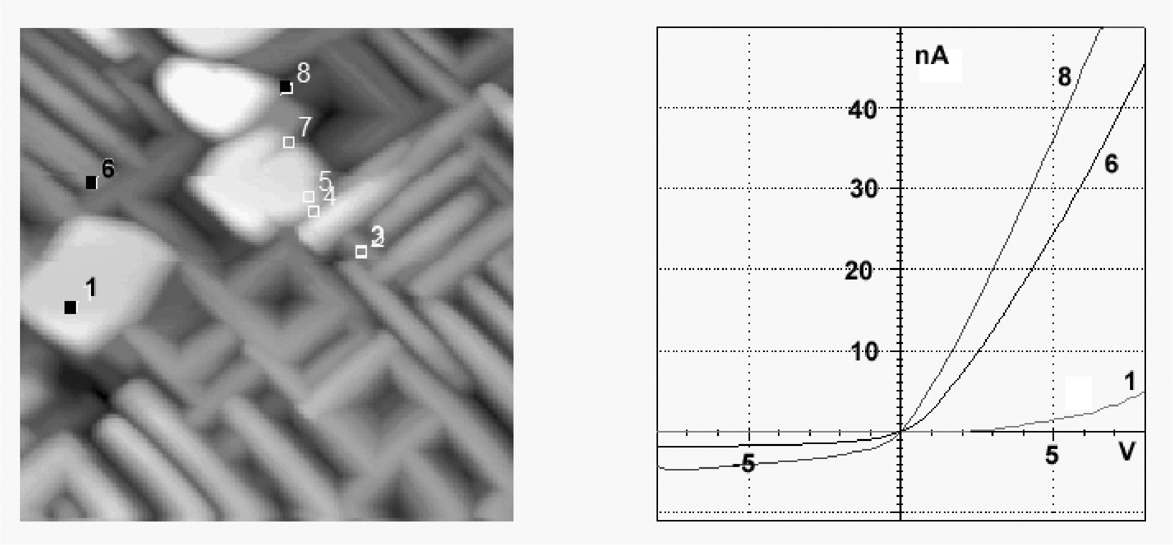

Figure 5.22: I-V curve measured on as deposited film: 1) along the polar axis, 6)8)perpendicular to the polar axis. Topografy image 1μm.

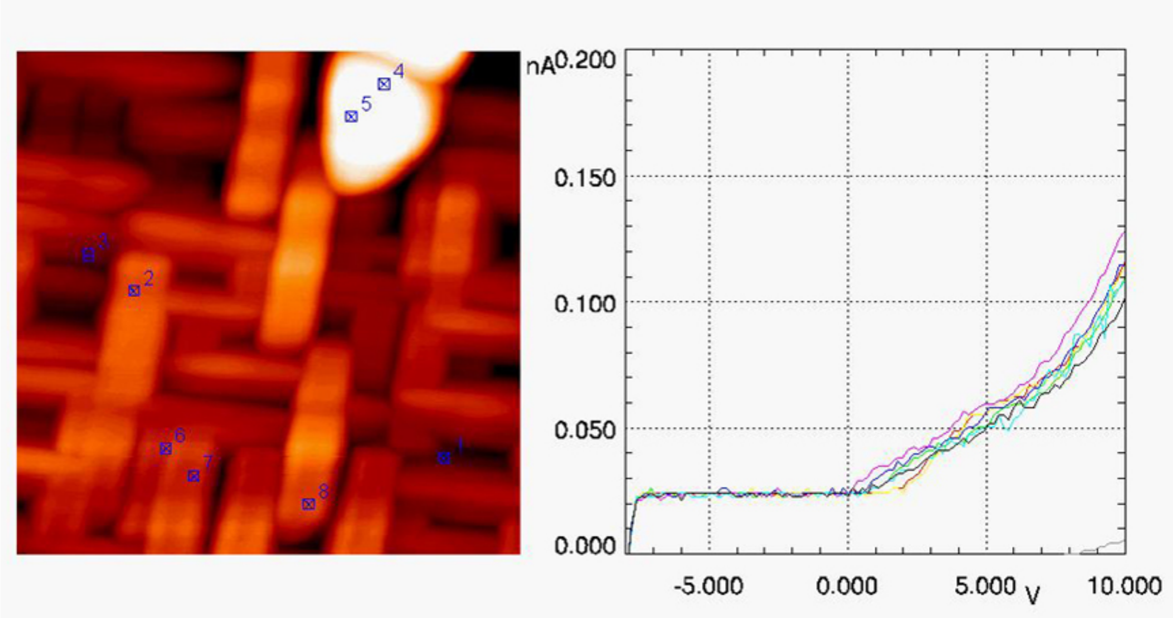

Figure 5.23: I-V curve of conduction along the polar axis and perpendicular to it, measured after annealing in oxygen. The peak of current at negative voltage is an artifact of measurement.

5.3.2 Piezoelectric Atomic Force Microscopy (PAFM)

In order to address conductivity, a 500 nm thick film exhibiting leakage on the macroscopic level was analyzed in more detail. Dielectric measurements have been performed on capacitors of a large range of electrodes sizes (10-500 μm diameter). The leakage current density was found to be independent of the electrode size. That means that, if the leakage were due to pinholes, their density would be higher than 0.012 μm^{-2}. The sample is formed mainly by rod shaped grains with polar axis in the plane of the film and therefore perpendicular to the applied field. The region of the sample chosen for the measurements includes some columnar grains that allows for characterization of the material along the polar axis as well.

Despite the strong conductivity at macroscopic scale, the local characterization by means of PAFM reveals piezoelectric activity of single grains. The sequence of images shows the response of the sample to a sinusoidal signal with 2V of amplitude applied to the bottom electrode while the AFM tip was grounded (Figs. 5.24-5.28). The columnar grain, with polar axis perpendicular to the film plane, at the center of the pictures and indicated by the arrows, is the most reactive to the excitation. It shows complete switching of polarization back and forth (Figs. 5.25-5.26).

In fig.5.24 is the piezo-response of the as grown film. The sample has been polarized afterwards, by applying a dc voltage to the bottom electrode while the grounded AFM tip was scanning the surface. The piezoelectric activity was measured after poling with the same amplitude ac exciting signal. Poling with +30V enhances the signal registered on the as grown film (fig.5.25). Here the polarization of columnar grains points out of the plane and the signal is more intense at their border. Poling with -30V reduce the amplitude of the signal but the phase of the columnar grains is inverted with respect to the previous picture (fig.5.26). A second scan with -40V fully switches the polarization as demonstrate by the phase shift of 180° and the strong contrast(fig.5.27). The previous direction of polarization is restored by poling with positive field (fig.5.28).

The sample shows an asymmetric electric behavior upon poling, the magnitude of the electric field has to be higher in the negative case. Such an asymmetry is found in macroscopic measurements as well, and can be attributed to the rectifying properties of the substrate-film interface.

The interpretation of the piezo-response of the columnar grains, where the polarization and the applied field are along the same direction, is straightforward. The amplitude is directly related to the intensity of piezoelectric activity. The phase shift depends on the reciprocal orientation of polarization and field, when the two vectors point in the same direction the response is in phase with the excitation, while it is it is out of phase when the two vectors are antiparallel. The grains show uniform response, therefore they are single domain.

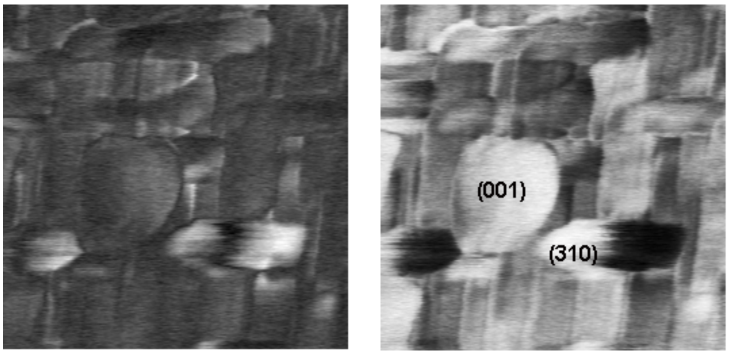

(a) (b)

Figure 5.24: (a) Amplitude and (b) phase, of piezo response without poling. Ac signal applied to the bottom electrode. The (001) grains exhibit a uniform polarization direction while the (310) oriented grains have a phase change. (1x1 μm scan area)

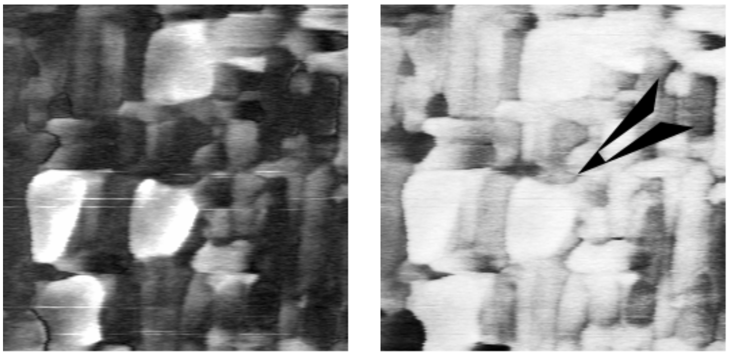

(a) (b)

Figure 5.25: (a) Amplitude and (b) phase, of piezo response after poling with +30V to bottom electrode, ac signal to the bottom electrode. The grains switched and give a signal in phase with ac voltage. (1.5x1.5 μm scan area)

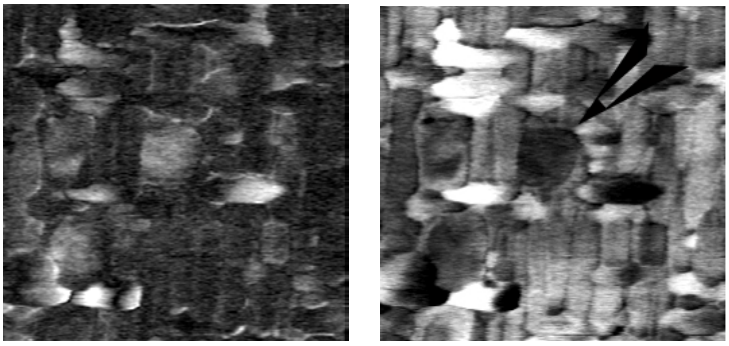

(a) (b)

Figure 5.26: (a) Amplitude and (b) phase, of piezo response after poling with -30V to bottom electrode, ac signal to the bottom electrode. (1.5x1.5 μm scan area)

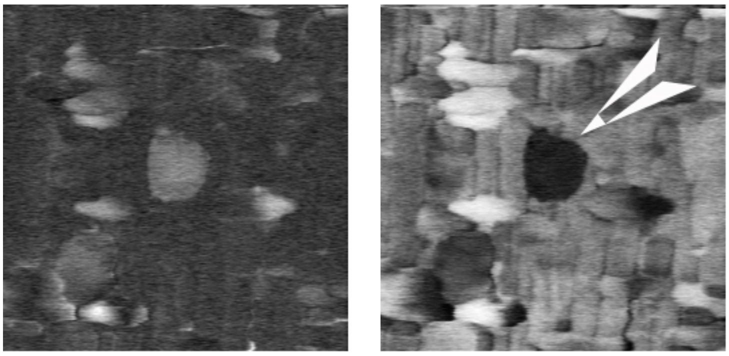

(a) (b)

Figure 5.27: (a) Amplitude and (b) phase, of piezo response after poling with -40V to bottom electrode, ac signal to the bottom electrode. (1.5x1.5 μm scan area)

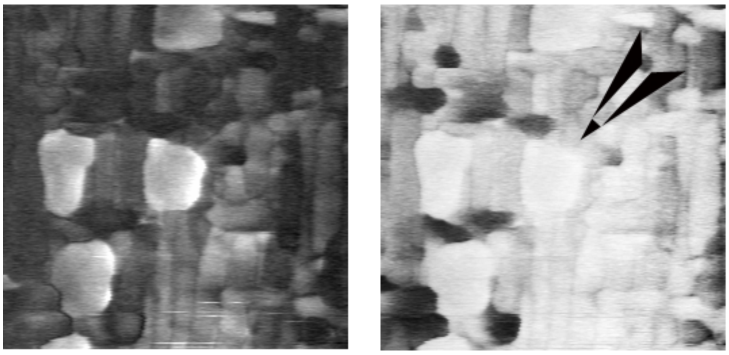

(a) (b)

Figure 5.28: (a) Amplitude and (b) phase, of piezo response after poling with +40V to bottom electrode, ac signal to the bottom electrode. (1.5x1.5 μm scan area)

In the case of rod-shaped grains the polar axis lays in the film plane and is thus perpendicular to the applied field. In this configuration no domain imaging is expected. However the field applied to the sample by the AFM tip is highly non uniform in both intensity and direction. Depending on the shape of the grain and on how the tip touches the surface, an unbalanced component of the electric field along the polarization direction can exist and be parallel or anti parallel to the polarization vector. The response of a rod-shaped grain shown in fig.5.29, can be interpreted as the distortion of the lattice due to an in-plane electric field (E_3) directed along the polar axis c. The measured out-of-plane distortion S_1 is characterized by the piezoelectric coefficient d_{31}, $S_1 = d_{31}E_3$. Note that d_{31} has a negative value. The direction of electric field and polarization coming from this interpretation are shown in fig.5.29b.

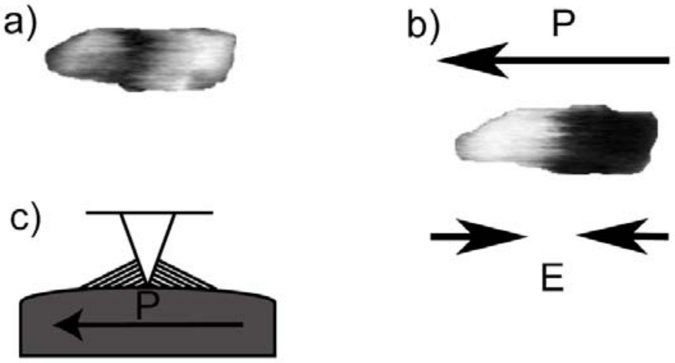

Figure 5.29: Piezo-response of a single rod-shaped grain with in plane polarization: a) amplitude, b) phase. Because of the negative value of the d_{31} piezoelectric coefficient, relevant in this experiment, where there is a component of the electric field parallel to the polarization the piezo-response is in antiphase with it, when the component is anti parallel the piezo-response is in phase. c) schema of the field lines coming out of the metallic AFM tip: the electric field is not perpendicular to the sample surface and a non zero component of the electric field E parallel to P exist. While in center of the grain this in-plane component of E is zero in average, when the tip is in proximity of the border of the grain it reaches a maximum. From this the high amplitude detected. At the very edge of the grain the overall intensity of the field is lower for both geometrical reasons and effect of conduction, as a consequence is lower the measured response.

5.3.3 Macroscopic characterization

Standard macroscopic capacitance measurement and hysteresis loops and have been performed using the capacitor prepared as described at page 112 Sect.5.1.2. In table 5.5 are summarized the properties of films with mixed phase(001)(310) where polarization lies both in-plane and perpendicular to the film plane, (Fig.5.32), and single phase (001) where polarization is perpendicular to the film plane (fig.5.30). Values for as deposited (ad) and post annealed in oxygen (ann) film are reported.

	mixed ad	mixed ann,	single ad	single ann
ϵ max	2400	2300	2400	2400
P_r ($\mu C/cm^2$)	5		5	10
E_c (kV/cm)	25		15	30
c. pyro ($\mu C/m^2 K$)		68		86

Table 5.5: Properties of SBN50 thin films deposited on STO single crystals. Mixed ((001)+(310) oriented) and single (pure (001) oriented) phase, as deposited (ad) and annealed in oxygen(ann).

5.3.3.1 Low field response

For all samples (Figs. 5.33, 5.31, 5.38), disregarding the orientation of the polar axis, the dielectric anomaly is very broad. The FWHM can be estimated as 300°C. The temperature at which the dielectric constant reach its maximum value is compatible with the bulk transition temperature, 120°C, and does not depend on frequency. This indicates that the material undergoes a phase transition of the ferroelectric type. The peak value of dielectric constant however, depends on the frequency and varies in an interval of about 300, such variability is reduced by annealing in oxygen (Fig. 5.31 and 5.33). No appreciable effect is seen in the losses of (001) oriented samples while in the (001)(310) case the exponential increase is shifted to higher temperature.

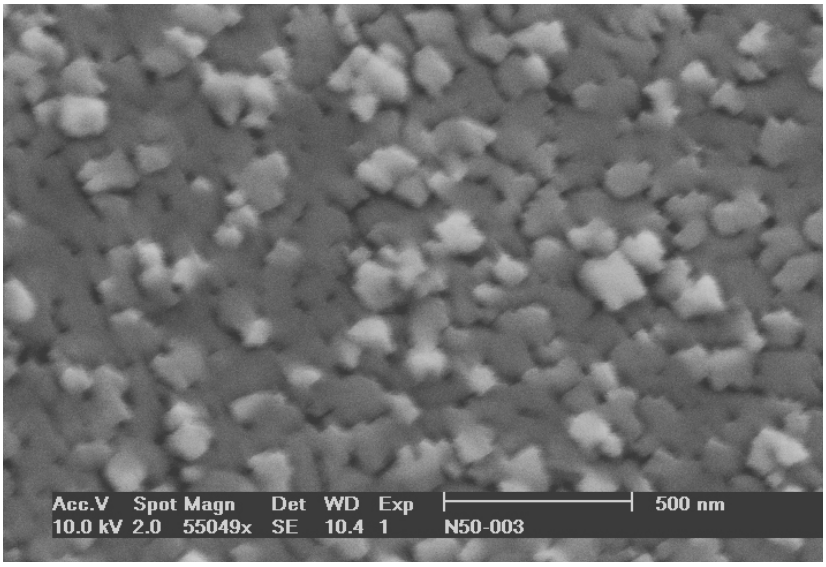

Figure 5.30: SBN50 grown on non treated STO. SEM image of the surface: the structure is purely columnar therefore the polar axis is oriented out of plane.

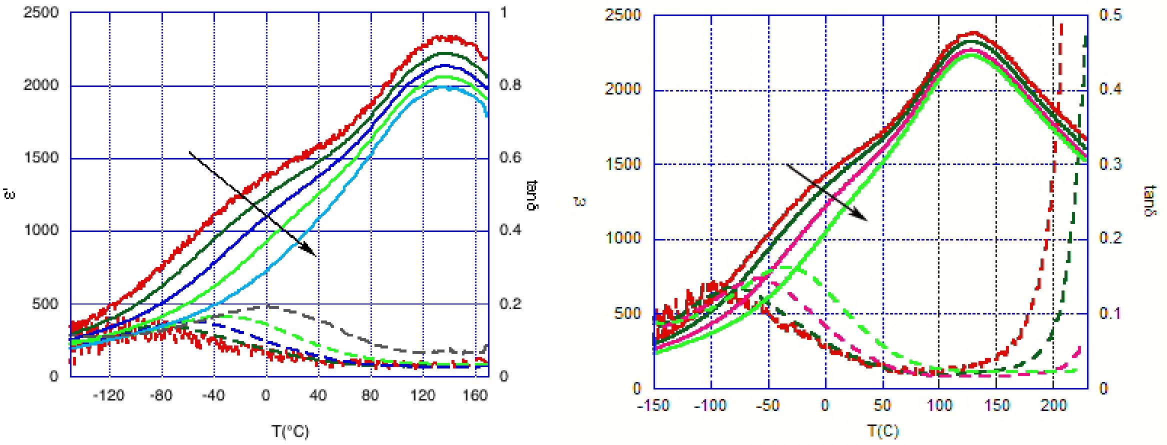

a)

b)

Figure 5.31: Dielectric constant and losses as function of temperature before (a) and after (b) annealing in oxygen for a (001) oriented sample. The arrows indicate increasing measurement frequency

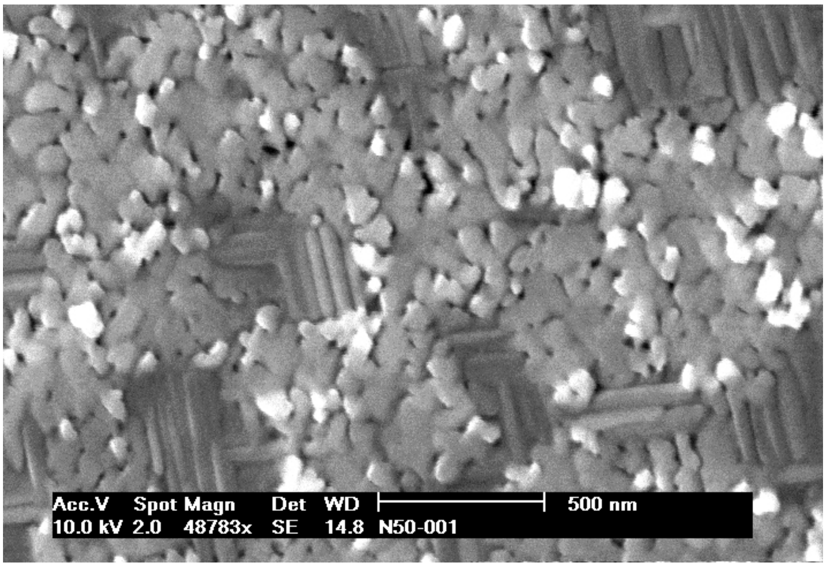

Figure 5.32: SBN50 grown on non treated STO. SEM image of the surface: the structure is a mix of columns and rods therefore the polar axis is oriented out-of-plane or in-plane.

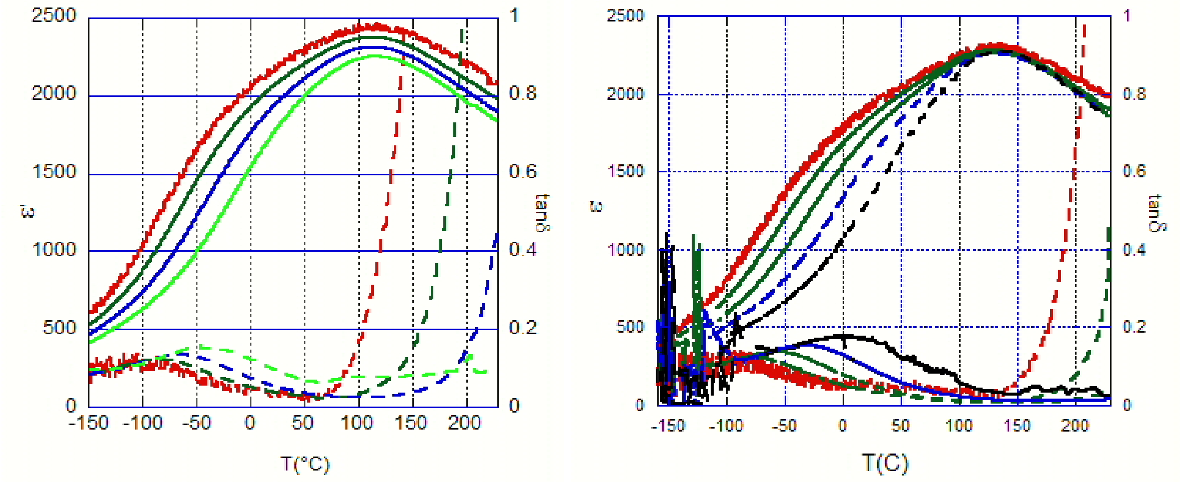

a) b)

Figure 5.33: Dielectric constant and losses as function of temperature before (a) and after (b) annealing in oxygen for a mixed phase sample.

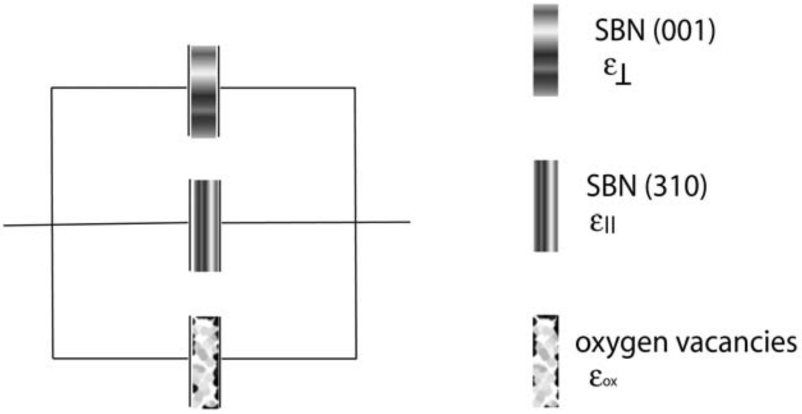

Figure 5.34: Capacitors model of SBN films with (001) and (310) oriented grains. The contribution of oxygen vacancies are taken into account by an in-parallel capacitor.

Two effects are expected from annealing in oxygen rich atmosphere: oxygen vacancies recovery, with consequent reduction of leakage, and better adhesion of electrodes with reduction of any inter-layer with different dielectric properties. From the AFM measurements we know that DC conduction of the as deposited samples is higher in the direction perpendicular to the polarization axis and annealing eliminates the asymmetry, this explains the behavior of losses in the mixed sample. The fact that the losses are not affected from this process indicate that in the (001) samples oxygen vacancies do not have a dominant effect in the leakage phenomenon. Conductive AFM measurements already gave evidence of this fact.

In both (001) and (310)-(001) samples the dielectric constant curves at different frequencies group together upon annealing, a contribution independent from temperature and from the absolute value of the dielectric constant is subtracted to each curve. This constant contribution can be represented by a capacitance in parallel to the ferroelectric one, a capacitance in series would give a stronger effect in correspondence of the dielectric peak and can therefore be excluded. The model of capacitance in parallel is represented in Fig.5.34: a first capacitance accounts for the bulk of the grains with ferroelectric properties, the second represents the contribution of oxygen vacancies. In single crystal form the real part of the dielectric constant along the polar axis ($\varepsilon_{\|}$) and perpendicular to the polar axis ($\varepsilon_{\perp}$) have values very close to each other, (about 400 at room temperature, Tab.1.2 and ref.[47]) with exception of temperatures close to the phase transition. Because in or samples the phase transition peak is strongly suppressed we take $\varepsilon_{\perp} = \varepsilon_{\|} = \varepsilon_f$ in the whole temperature interval measured, therefore the total dielectric constant becomes:

$$\varepsilon = (1-a)\varepsilon_{\perp} + a(\varepsilon_{\|} + \varepsilon_{ox}) \quad = \quad \varepsilon_f + a\varepsilon_{ox}$$

where ε_f is the dielectric constant due to the ferroelectric part. The constant a is a geometrical factor that takes in to account the fact that the oxygen vacancies contribution to the dielectric signal, ε_{ox}, is limited to the sample's portion with the in-plane polarization axis. The oxygen vacancies contribution is due to the dielectric relaxation of related hopping charged defects as discussed for the case of low purity SBN in Sect.5.2.2.1. It is reduced or eliminated by annealing.

The peak value of dielectric losses is reached at a temperature lower than the temperature of the dielectric constant peak, and it has a strong frequency dispersion; at this temperature the dielectric constant shows frequency dispersion not affected by annealing. tanδ measurement performed on single crystal samples (SBN60) by Huang at al. exhibit similar features[38] (Fig.1.4, page 16); in this case a broad peak at about −100°C, dispersed in frequency, is observed together with the peak at the critical temperature. While the dispersed low temperature peak is scarcely affected by the application of a bias field, the peak at the critical temperature is strongly suppressed by a field of 7.5 kV/cm. From the behavior of single crystals we can suppose that a bias electric field is acting on our samples, suppressing the peak at the critical temperature and leaving the dispersed broad peak only. Evidence for such a bias field, in the order of magnitude of 10kV/cm, will be found in the high field measurement discussed later.

5.3.3.2 Hysteresis and CV curves

High field measurements are strongly affected by leakage. Samples with mixed orientation,(310)(001), are more leaky than (001) oriented ones. In the first case, when enough field can be applied to the capacitor, hysteresis loops have rounded edges and very low remanent polarization, Fig.5.35. Annealing in oxygen can increase leakage leading to conduction, as in the mixed phase samples case, or reduce it as for the case of (001) oriented samples (Fig.5.36). Oxygen vacancies in the TTB structure therefore, are not the only responsible for conduction through the capacitor; we believe that annealing improves the adhesion of the Pt top electrode but, at the same time, creates paths for the charges to go trough the sample, experimental evidence for this phenomenon is found in the CV curves measurements. The comparison of experimental data taken from (001) and (310)-(001) oriented samples indicate that the creation of such paths is more effective in the case of in-plane polarization oriented grains.

The onset of conduction in the sample require the overcome of a threshold electric field, this is visible in the CV curves measured on (001) samples. The behavior of the dielectric loss as function of the applied voltage in the CV curves in Fig. 5.37, is clearly suggesting a diode behavior of the sample, which can be thought as a capacitor with ferroelectric properties, in parallel with a diode. When the diode is inversely biased, in our case when the electric field is directed from the STO electrode to the Pt electrode, the properties of the ferroelectric sample are measurable and the CV curve has the typical butterfly shape. When the diode is forward biased and the electric field is directed fro mthe Pt electrode to the STo electrode, a current can flow trough it, which is exponentially dependent on the applied dc voltage.

The current density in a diode is given by:

$$J = J_s \left[\exp\left(\frac{qV_{dc}}{k_B T} \right) - 1 \right] \tag{5.10}$$

where q is the unitary electric charge. The differential conductivity of the diode, σ_{ac}, can be calculated as:

$$\sigma_{ac} = \frac{dJ}{dE} = \frac{J_s q l}{k_B T} \left[\exp\left(\frac{qV_{dc}}{k_B T} \right) - 1 \right] \tag{5.11}$$

where l is the distance between the electrodes of our capacitance and E the applied electric field. The differential conductivity of dielectric material, is related to the dielectric loss, tanδ, by the the following formula:

$$\sigma_{ac} = \omega\varepsilon_0\varepsilon^{'}\tan\delta \tag{5.12}$$

where ω is the measurement frequency, $\varepsilon^{'}$ the real part of the relative dielectric constant and ε_0 the dielectric constant of vacuum. The combination of equations 5.11 and 5.12 gives the exponential dependence of the dielectric loss on the applied dc voltage:

$$\tan\delta = \frac{J_s q l}{k_B T\omega\varepsilon_0\varepsilon^{'}}\left[\exp\left(\frac{qV_{dc}}{k_B T}\right) - 1\right] \tag{5.13}$$

The interface SBN-STO is a junction between a heavily n-doped STO and an non or slightly doped SBN, and behaves as a rectifier. The electric field directed from the SBN film to the STO substrate, forward biases the junction and enhances the losses when it exceeds a threshold value, indicating the onset of leakage conduction. Below the threshold of 50 kV/cm leakage is low and the hysteretic behavior of the ferroelectric can be measured. Annealing sharpens the threshold field of conduction and eliminate the loss hysteresis, Fig. 5.37. The real part of the dielectric constant is increased but the range of applicable dc electric field is reduced of about one order of magnitude. This behavior well agrees with the low field measurements of fig.5.31. AFM measurements demonstrate that conduction through the bulk of grains is reduced by annealing. Therefore we conclude that, by improving adhesion of the Pt electrode, annealing creates easy paths for conduction through grain boundaries.

The hysteresis loops, before and after annealing, are clearly asymmetric as indicated by the coercive field and the slope of the loop, fig.5.36; the asymmetry amounts to about 50 kV/cm. Here the voltage is applied to the STO electrode.

CV curves have been measured on (001) oriented samples. They show the same asymmetric behavior of the hysteresis loops, with an offset of about 10kV/cm as determined by the position of the crossing point in the CV curve. In this case the voltage is applied to the Pt electrode, Fig. 5.37. Even though different in magnitude, both CV and hysteresis curves indicate the presence of a bias field directed from the bottom to the top

electrode with intensity in a range that support the hypothesis made at the end of section 5.3.3.1. There we suppose that the peak of dielectric losses, that should appear in correspondence of the critical temperature, is suppressed by a bias field. This field can be attributed to the different work function of the two electrodes, Pt and STO. When a metal is brought to contact with a ferroelectric a Schottky barrier can be formed, depending on the difference between metal and ferroelectric work functions and sign of the trapped charges. As a consequence a field is built-in. In our capacitors we have two metal ferroelectric interfaces. When both electrodes are made by the same metal the built-in fields have the same magnitude and opposite sign. In this case the CV and hysteresis curves are supposed to be symmetric and only the magnitude of the applied field needed to obtain a response (capacitance and polarization respectively) of a given magnitude is affected. In the case of films grown on doped STO substrates, the work function of the two electrode is not the same and the built-in fields at the two interface do not compensate. From this the asymmetry observed in the measurements.
Properties of (421) oriented films as-grown on (111) STO are shown in figs.5.38 and 5.39. The dielectric constant measured as function of temperature at different frequencies (figs.5.38a) show a wide gap between the curved measured at 10 kHz and the one measured at 100 kHz. The losses peak is smeared in temperature. The loss increase exponentially above a threshold temperature whose value depend on frequency as in the case of the mixed orientation samples. In the CV curve measurement (figs.5.38b) the loss remain below 0.1 for the whole range of applied field, the P-E loops (figs.5.39) are not affected by hysteresis due to leakage. From the limited experimental data available we can only argue that, the samples are much less affected by conduction at high field but they have defect contributing to the dielectric constant at low applied field in the frequency range 100 Hz-10 kHz. The diode behavior is present as well, even though shifted at higher field, confirming that this is rather a property of the interface STO/SBN than of the film itself.

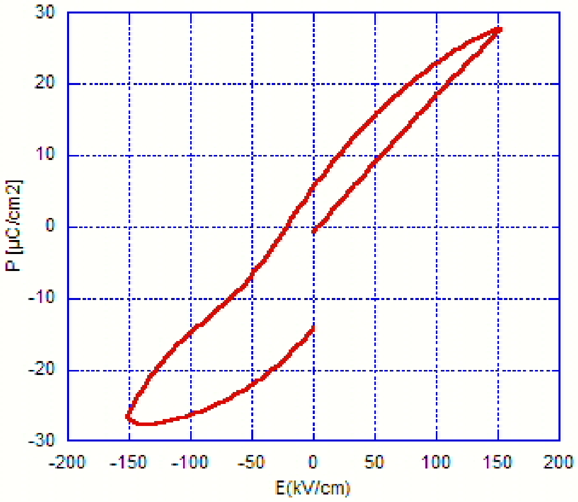

Figure 5.35: Hysteresis loop measured on a as deposited (310)(001) oriented sample

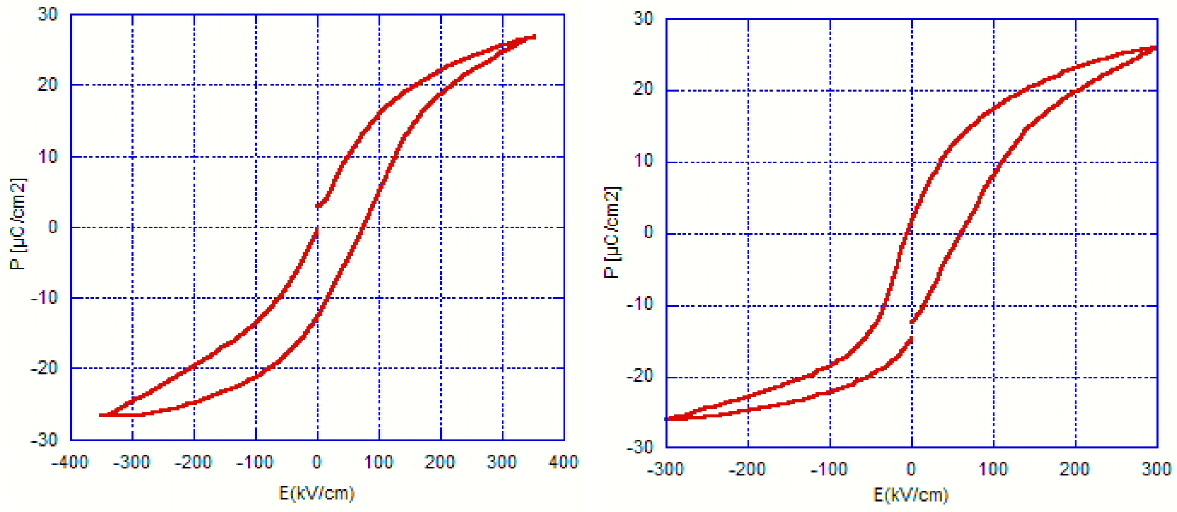

Figure 5.36: Hysteresis loops before and after annealing in oxygen measured on a (001) oriented film.

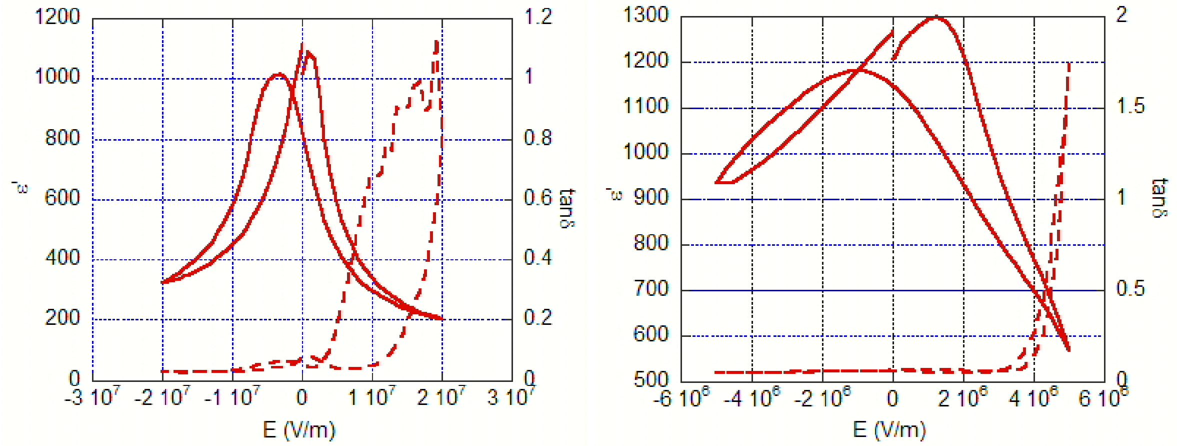

Figure 5.37: CV curve before (a) and after (b) annealing from a (001) oriented film. The thermal treatment removes the hysteresis in the losses and reduces the threshold field value below which the CV curve can be measured.

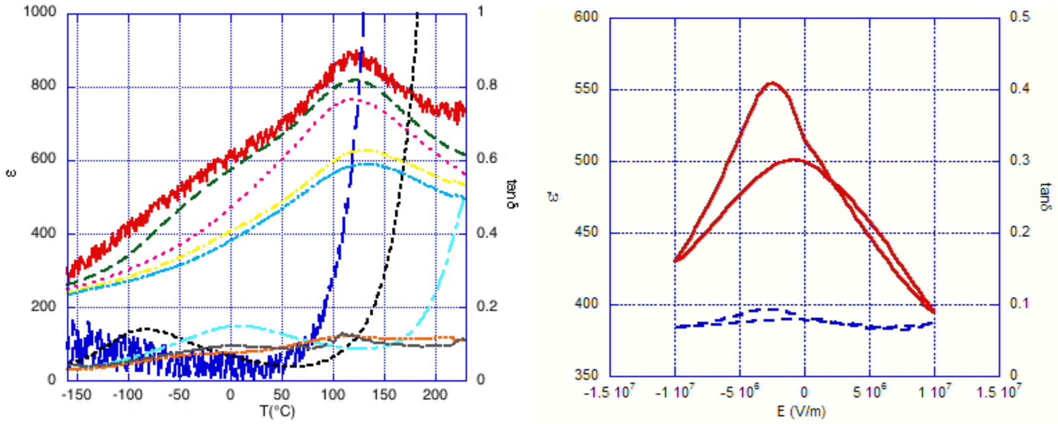

a) b)

Figure 5.38: a) Dielectric constant behavior as function of temeperature and b) CV curve at room temperature, of a (421) oriented film deposited on (111) STO single crystal

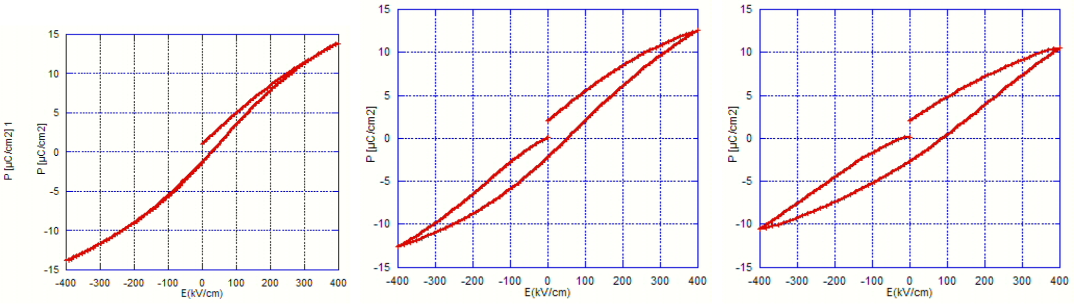

a) b) c)

Figure 5.39: Hysteresis loops measured on a (421) oriented thin film at a)$23°C$, b) $-80°C$, c)$-150°C$

5.3.3.3 Suppression of the phase transition dielectric peak

One of the more striking feature of the dielectric constant measurements as function of temperature presented in the previous pages is the suppression of the peak related to the phase transition. While for SBN50 single crystals peak values of about 10^5 are reported we found values in the order of 2×10^3. It is remarkable that the room temperature values are higher in the case of our thin films (10^3 against 400 for the single crystal). In the discussion that follows we will see how the presence of a non ferroelectric layer (referred to as "dead layer", Fig. 5.40) at the interface ferroelectric-electrode can induce the suppression of the phase transition peak leaving unchanged the critical temperature.

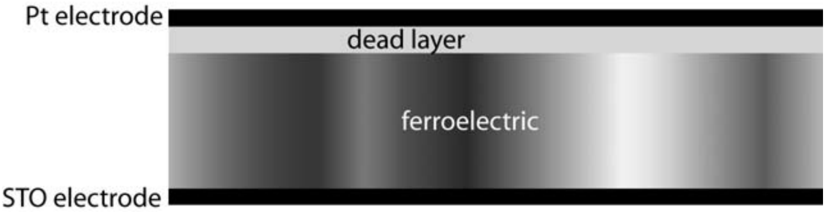

Figure 5.40: Ferroelectric film sandwiched between two electrodes with a dead layer at the Pt interface.

When a metal and a ferroelectric are bring to contact a Schottky barrier can be formed with a consequent space charge layer and a built-in field at the interface;[154] because there are no free charges in a dielectric, in our case we have depletion of traps at the interface. Such a depleted layer most likely has dielectric properties different from the "bulk" of the film and is not expected to be ferroelectric. The built-in field is expressed as:

$$E_{bi} = eNw/\varepsilon$$

N is concentration of relevant deep traps, e their charge, w depletion width (supposing w smaller the half film thickness) and ε dielectric constant of the ferroelectric.

The switching of polarization in the ferroelectric starts when the external applied electric field reach a value given by the sum of the interface field and the threshold field for nucleation typical of the ferroelectric material. The measured coercive field is thus the difference between threshold and built-in field: $E_c = E_t - E_{bi}$.

The intensity of the built-in electric field depends on the work function difference between metal and ferroelectric. Therefore, if the two electrodes are constituted by different materials we can expect the field at the two interfaces to be different. From this originate the asymmetry in measured hysteresis loops.

The presence of a non ferroelectric layer at the ferroelectric electrode interface has an influence on dielectric constant as function of temperature. The ferroelectric plus the non-ferro layer can be treated as in series capacitance and the dielectric constant of the sample becomes:

$$\frac{t_d + t_f}{\varepsilon} = \frac{t_d}{\varepsilon_d} + \frac{t_f}{\varepsilon_f}$$

where:

- t_d, t_f thicknesss of non-ferro and ferroelectric layers, respectively.

- $\varepsilon_d, \varepsilon_f$ dielectric constants of non-ferro and ferroelectric layers, respectively.

The dielectric constant of the ferroelectric layer is given by the Curie-Weiss law:

$$\varepsilon_f = \frac{C}{T - T_0}$$
$$T > T_0$$

$$\varepsilon_f = \frac{C}{2(T_0 - T)}$$
$$T < T_0$$

with T_0 the critical temperature and C Curie-Weiss constant. When approaching the critical temperature from the paraelectric phase ($T > T_0$) we have:

$$\frac{t_d + t_f}{\varepsilon} = \frac{t_f(T - T_0)}{C} + \frac{t_d}{\varepsilon_d}$$

$$\frac{1}{\varepsilon} = \frac{T - T_0 + \frac{t_d C}{t_f \varepsilon_d}}{\frac{C}{t_f}(t_f + t_d)}$$

The result is a shift of the critical temperature at lower values:

$$T_0 - \frac{t_d C}{t_f \varepsilon_d}$$

and a reduced "Curie-Weiss" constant, depending on the ratio t_d/t_f.
The same treatment, approaching the critical temperature from the ferroelectric phase gives a shift to higher values.

$$T_0 + \frac{2 t_d C}{t_f \varepsilon_d}$$

In both cases the effect of a non-ferroelectric layer in series with the ferroelectric, is to shift far away the critical temperature, independently on which side it is approached. The result of the two opposite effects is a suppression of the dielectric constant maximum that remains at the original critical temperature T_0 (see Fig. 5.41). In this discussion the sample is supposed to split into domains while it undergoes the phase transition. In this way the depolarizing field associated with the appearance of spontaneous polarization is on average suppressed within the film. If this is not the case and one single domain is created within the sample, the effect of the depolarizing field would be a shift to lower temperature of the transition depending on the intensity of

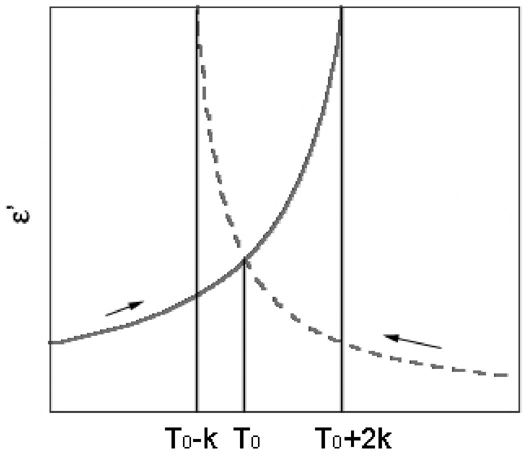

Figure 5.41: Non ferroelectric layer in series with a ferroelectric one: effect on the dielectric constant behavior across the phase transition

the depolarizing field itself.

In Fig. 5.42 is shown the comparison between the inverse of dielectric constant of our thin film sample (001) oriented, and the data reported by Olivier et al.[47] for SBN60 single crystal along the [001] direction. The behavior is clearly different in the two cases. We can remark the following features of curve belonging to the thin film:

- the peak of dielectric constant is suppressed
- the critical temperature remains the same as in single crystals
- at temperature much lower than the critical temperature, the slope of the curve is highly increased and is higher than in single crystals (the difference would be higher than shown, with data belonging to SBN50 crystal)
- there is a change in slope around $0°C$

The first two points are in agreement with the prediction of the model presented above. The third is against the model that predicts a decrease of slope as the curie constant

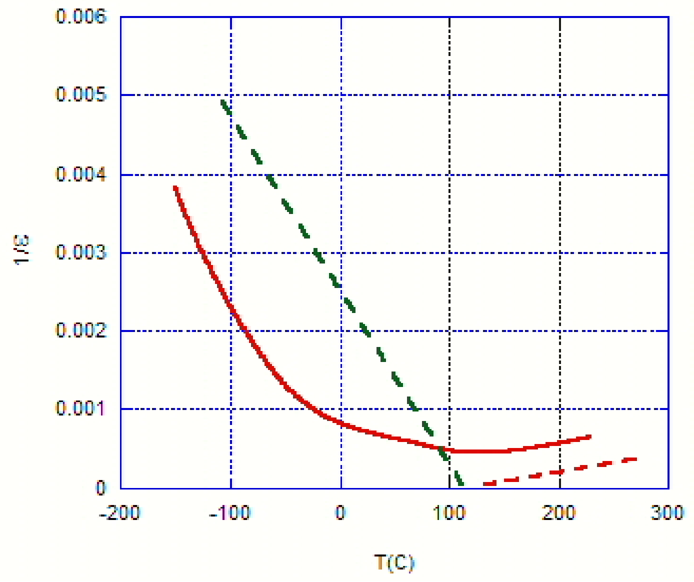

Figure 5.42: Inverse of the real part of the dielectric constant in a temperature range including the phase transition. The values measured on a (001) oriented sample at 10kHz (full line) are compared with values measured on SBN60 single crystal in the same conditions[47] (broken line). The curve relative to the single crystal has been translated in temperatures to have the the critical temperature at 120°C, for the sake of comparison.

C transforms in $C(1+\frac{t_d}{t_f})$. The fourth point is not predicted by the model. The values of dielectric constant at low temperature, higher in the film than in the single crystal, do not find explanation in the proposed model. While the passive layer scenario is plausible, it can not fully describe the behavior of our films. Such a behavior can be due to the existence of not one but a distribution of transition temperatures (from the experimental data we can estimated this distribution to be in the interval $0° - 120°$C). This would lead to both suppression of the peak and rise of the dielectric constant value in the phase transition temperature range. The smearing of the transition over an interval of temperature has been observed in SBN single crystals as well (see Olivier et al.[47]), and it is attributed to the unfilled nature of the TTB structure in SBN. While for single crystals the temperature range amounts to something like 10°, in thin films this feature is highly enhanced, a sign of higher degree of disorder.

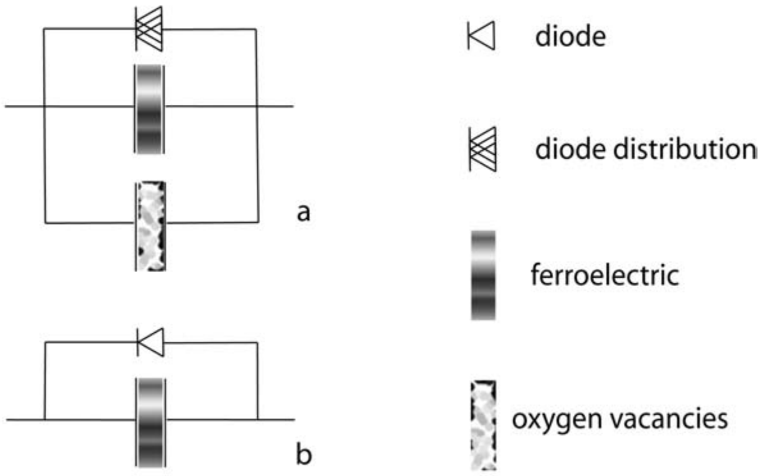

Figure 5.43: Circuit model of thin film capacitor: a) as deposited b) after annealing.

5.3.4 Conclusions

The properties of the SBN films analyzed in this section are summarized as follows:

- Oxygen vacancies conduction is more efficient along the (310) direction, i.e. perpendicular to the polarization axis.
- Single grains of both (001) and (310) orientation are piezoelectric and ferroelectric.
- The dielectric anomaly at $120°C$, related to the ferroelectric phase transition, is broader with reduced peak value than in the single crystal case. Diffusion of the phase transition over a temperature range is the most probable explanation even tough the passive layer scenario can not be excluded as concomitant cause.
- Annealing promote the creation of easy path for conduction, located at the grain boundary.
- The different work-function of the two electrodes induces the diode behavior of the dielectric losses, whose threshold field is sharpened by annealing.

In fig. 5.43 are represented the samples before and after annealing. There we find: a capacitance in parallel with the ferroelectric representing the oxygen vacancies contribution, a distribution of diodes with different I-V characteristic and threshold field. Depending on crystals orientation, the importance of each element is different. Upon annealing the oxygen vacancies contribution is strongly reduced and the threshold field for the onset of conduction is sharpened, its magnitude depends on grain orientation and boundaries distribution: very low in the (320) orientation, higher for the (001) and (421) orientation. Clearly thermal treatment is efficient in reducing defects at the interface with the Pt electrode but not at the grain boundaries; for this reason leakage remains as the main problem of our samples.

Summary of results and conclusions

This thesis was devoted to the study of growth and functional properties of SBN thin films. The main goals were to grow SBN thin films with the polar axis oriented perpendicular to the film plane and to integrate them in capacitor structures. As this has been proven to have a strong influence on both structural and functional properties of the films, special attention has been put in the substrate choice.

SBN thin films were grown in-situ by Pulsed Laser Deposition from ceramic targets prepared by calcination and sintering of Ba and Sr carbonate and Nb pentoxide. The ablation of the ceramic was congruent resulting in a film composition that was identical to the target composition. It was found that the dielectric and ferroelectric properties of SBN are very sensitive to contaminations of even less than 1 % concentration. Ceramics prepared from low purity Ba carbonate show a lowering of the critical temperature superior to $100°C$ and enhancement of the relaxor properties. Therefore, high purity powders are necessary for the fabrication of the target.

For the nucleation of the TTB structure, the deposition temperature and the oxygen partial pressure must exceed $720°C$, and 10^{-2} mbar, respectively. A lower deposition rate, obtained by a smaller laser pulse repetition frequency, improves the epitaxial growth in agreement with standard theories on growth. Target-to-substrate distance and laser pulse energy have no evident influence on the film properties indicating that the ion impact does not play any role. The main growth mechanisms are a consequence of large thermal activation to overcome nucleation and growth activation energies, and to increase diffusivity. The temperature threshold is common to other deposition techniques, like sol-gel and sputtering, reflecting the large activation energies needed for the formation of a complex structure such as TTB, which cannot be supplied by the kinetic energy of the arriving species. As-deposited films suffer from oxygen vacancies independently from the oxygen partial pressure during deposition. These can be significantly removed by a post-deposition thermal treatment in oxygen rich atmosphere. The high deposition and post annealing temperatures require the use of chemically inert and thermally stable substrates. Direct growth of SBN on Si leads to the formation of an amorphous oxide interlayer composed of Si and Nb oxides. The TTB film exhibits mostly (001) orientation. The use of Pt films as substrate and electrodes has been considered, but Pt thin film on oxidized silicon are thermally unstable and tend to delaminate during the deposition process or the post-anneal. The instability is caused by the large difference in thermal expansion of SBN and silicon, leading to compressive stresses, in combination with Pt diffusion along grain boundaries and interfaces. Optimization of adhesion and barrier layer between Pt and Si (Ta/Si_3N_4) has been attempted, but no well reproducible quality of adhesion was achieved.

SBN was found to grow well in an epitaxial manner on STO single crystals; the interface stays clean and no interdiffusion was observed. The growth is characterized by the following features:

1. The growth proceeds in Volmer-Weber mode. This means that we do not deal with a simple epitaxy leading to layer-by-layer growth. Instead, the new phase must first nucleate. Interface and/or surface energy must be large enough to result in 3-d island growth.

2. The crystalline orientation, and consequently also grain shape, is controlled by the STO surface termination. The starting point of SBN crystal nucleation is the perowskite kernel that grows as a continuation of the substrate perowskite structure, the SBN unit cell then organizes around the perowskite kernel. In case of STO(100), the development of c-axis direction depends on the surface termination of STO: TiO_2 termination leads to in-plane c-axis orientation (i.e. (310)), SrO termination to out-of-plane c-axis orientation (i.e. (001)). The observed (421) orientation on STO(111) is readily explained by postulating the nucleation of the perowskite kernel in (111) orientation as continuation of the substrate structure. We always observe growth of twins related to ±18° rotation of the perowskite kernel with respect to the unit cell

a-axis. The realization of a unique variant seems highly improbable. The nucleation mechanism based on the perowskite kernel makes possible two in-plane orientation of the SBN film (two variants) in the case of (001) orientation. By the same mechanism four variants grow in the (310) and (421) oriented films.

Concerning dielectric properties, it has been found that the films grown on Si-based substrates have the peak of the dielectric constant shifted to a $100°C$ lower temperature than measured in the bulk ceramic (target). This is due to the thermal stress induced in the film during cooling from the deposition temperature. The amount of the shift can be explained in the framework of the LGD theory. The films grown on Nb-doped STO exhibit the same critical temperature as the target ceramic. In the case of high purity SBN films on STO, the critical temperature coincides also with the one of single crystals of the same composition (SBN50). Such film show the characteristics of a para to ferroelectric phase transition, although it is much broader than in the single crystal case, and the peak values are strongly reduced. In contrast the dielectric constant at room temperature is higher in the thin films than in the single crystals. Both effects can be explained supposing the smearing of the phase transition on a temperature interval. The cause of smearing is to be found in the high disorder of A and B site occupancy induced by the low processing temperature of thin films compared to the processing temperature of single crystals. The presence of a dielectric layer at the interface SBN/substrate could account for the lowering of the dielectric peak, and its contribution to the effect is not excluded, but not to the increased room temperature value.

Leakage is the main problem of the obtained samples. It affects the small field dielectric behavior and even more the high field dielectric properties, as shown by CV curves (i.e. quasi-static) and hysteresis loops (500Hz). A diode effect has been found, attributed to the rectifying characteristic of the STO:Nb/SBN interface. Such an effect is accentuated by annealing after the deposition of the top electrodes. AFM spectroscopic measurement revealed that the conduction is much stronger in the direction perpendicular to the polar axis than along it. After annealing, grains of both orientations have the same I-V curve and the conduction is reduced by about three orders of magnitude. We conclude that the conduction is due to oxygen vacancies and that the observed asymmetry is an asymmetry the in mobility of oxygen atoms. Single grains have been proven to be ferroelectric by PAFM measurements, in the case of both in-plane and out-of-plane polar axis. The leakage observed in macroscopic measurements after recovering oxygen vacancies by thermal treatment, is most likely to occur at the grain boundaries. This type of leakage mechanism is also supported by the fact that columnar grain structure like SBN(001) on STO(100) are more conductive than random grain structures as in case of SBN(421)/STO(111).

The main results of this work can be summarized in the following points:

- SBN films grow in Volmer-Weber mode and the grains grow along the polar axis, as observed in single crystals growth. On amorphous or polycrystalline substrates the film grows with the polar axis perpendicular to the film plane. In the case of epitaxial growth the direction of the polar axis with respect to the film plane is determined by the substrate surface, therefore it can be tailored by the appropriate choice and preparation of the substrate. The observed crystal twins prove that the film starts to nucleate from the perovskite kernel.

- oxygen vacancies are easily formed in the TTB structure under the processing condition of PLD. They induce an anomaly in the dielectric constant at the temperature of 100°C and conduction at room temperature with intensity higher in the direction perpendicular to polarization axis than along it.

- ferroelectricity is possible in SBN films. Single grains are proven to be ferroelectric but leakage trough grain boundaries does not allow the observation of ferroelectric properties at bigger scale.

- the ferroelectric properties are strongly dependent on the processing condition, raw materials quality and film-substrate thermal expansion mismatch. The smearing of the phase transition is most likely due to the low processing temperature, preventing an ideal distribution of A and B site occupancy by Ba and Sr ions.

Outlook

$(SrBa)Nb_2O_6$ has proven to be an interesting system not only for its unique ferroelectric properties but also for the study of heteroepitaxial growth of complex oxide thin films. Better knowledge on the nucleation can be gained by using monocrystalline substrates with perovskite structure and others. Various orientations of the terminating surface should be chosen and special attention should be given to the symmetry of the reconstructed surface.

In order to study the ferroelectric properties of these samples the electric leakage needs to be minimized. For this purpose, the effect of thermal treatments at temperature higher than the processing one, should be investigated. Grain growth due to high temperature and long annealing time would result in a decreased density of grain boundaries. At the same time, defects in the grain boundary would be reduced as well. The use of dopants is another possibility to reduce electrical leakage; a dopant concentrated in the boundary would reduce the mobility of ions and therefore their conduction and would have influence on the electronic conduction at the same time.

The optimal conductive substrate for the fabrication of parallel plate capacitors has not been found yet. Doped ionic crystals like STO show a semiconductor behavior which interferes with the ferroelectric properties of SBN. Such an interference is avoided by using a metallic electrode. Chemical as well as mechanical stability of metallic films on silicon wafers proved to be difficult to achieve at processing conditions needed for SBN. A multilayer electrode like Ir/Pt on silicon could solve these problems by combining the mechanical stability of Ir with the chemical stability of Pt.

Bibliography

[1] R.R. Neurgaonkar, J. R. Oliver, W.K. Cory, L.E. Cross, and D. Viehland. *Ferroelectrics*, 160:265–276, 1994.

[2] A.M. Glass. *Journal of applied physics*, 40(12):4699, 1969.

[3] R. R. Neurgaonkar, R. Ratnakar, W.K. Cory, J.R. Oliver, M.D. Ewbank, and W.F. Hall. *Optical Engineering*, 26(5):392–405, 1987.

[4] W. Kleemann, J. Dec, P. Lehnen, R. Blinc, B. Zalar, and R. Pankrath. *Europhysics Letters*, 57(1):14–19, 2002.

[5] P.B. Jamieson, S.C. Abrahams, and J.L. Bernstein. *The J. of Chem.Phys.*, 48(11):5048–5057, 1968.

[6] T. S. Chernaya, T. R. Volk, I. A. Verin, L. I. Ivleva, and V. I. Simonov. *Crystallography Reports*, 47(2):213–216, 2002.

[7] T. S. Chernaya, B. A. Maksimov, I. V. Verin, L. I. Ivleva, and V. I. Simonov. *Crystallography Reports*, 42(3):375–380, 1997.

[8] T. S. Chernaya, B. A. Maksimov, T. R. Volk, L. I. Ivleva, and V. I. Simonov. *Physics of the Solid State*, 42(9):1716–1721, 2000.

[9] M. P. Trubelja, E. Ryba, and D. K. Smith. *Journal of Materials Science*, 31(6):1435–1443, 1996.

[10] H. Lee and R. Freer. *J.Appl.Cryst*, 31:683–691, 1998.

[11] L.A. Bursill and P.L. Lin. *Acta Cryst.*, B43(2):49, 1987.

[12] Subbarao, Shirane, and Jona. *Acta crystall.*, 13:226, 1960.

[13] R. R. Neurgaonkar, W.K. Cory, and J. R. Oliver. *Ferroelectrics*, 15:3, 1983.

[14] R. R. Neurgaonkar, J. R. Oliver, and L.E. Cross. *Ferroelectrics*, 56:31, 1984.

[15] R. R. Neurgaonkar and W.K. Cory. *J. Opt. Soc. Am. B*, 3(2):274, 1986.

[16] R. R. Neurgaonkar, J.R. Hall, J. R. Oliver, W.W. Ho, and W.K. Cory. *Ferroelectrics*, 87:167, 1988.

[17] S.C. Abrahams, L.A. Kurtz, and P.B. Jamieson. *Phys. Rev*, 172:551, 1968.

[18] Y. Xu. *Ferroelectric materials and their application.* North-Holland, 1991.

[19] Y. Xu, Z. Li, W. Li, and H. Wang. *Phys. Rev. B*, 40(17):902, 1989.

[20] W. Kleemann. *Journal of Non-Crystalline Solids*, 307:66–72, 2002.

[21] N. Setter and L.E. Cross. *J.Appl.Phys*, 51(8):4356, 1980.

[22] L.E. Cross. *Ferroelectrics*, 76:241, 1987.

[23] G. Burns and F. Dacol. *Solid state communications*, 48(10):853ñ856, 1983.

[24] T. Granzow, T. Woike, M. Wohlecke, M. Imlau, and W. Kleemann. *Physical Review Letters*, 92(6):–, 2004.

[25] T. Granzow, U.B. Dorfler, and T. Woike. *Phys. Rev. B*, 63:174101, 2001.

[26] T. Granzow, T. Woike, M. Wohlecke, M. Imlau, and W. Kleemann. *Phys. Rev. lett*, 89(12):127601, 2002.

[27] A.S. Bhalla, R. Guo, L.E. Cross, G. Burns, F.H. Dacol, and R. R. Neurgaonkar. *J.Appl.Phys*, 71(11):5591, 1992.

[28] W.H. Huang, D. Viehland, and R. R. Neurgaonkar. *J.Appl.Phys*, 76(1):490, 1994.

[29] N.S. VanDamme, A.E. Sutherland, L. Jones, K. Bridger, and S.R. Winzer. *Journal of American Ceramic Society*, 74(8):1785–1792, 1991.

[30] S.B. Desphande. *J. Am. Ceram. Soc.*, 75(9):2581, 1992.

[31] C Ellisade and J Ravez. *J. Materials Chem*, 10:681–683, 2000.

[32] Schneck, Toledano, R.W. Whatmore, and Ainger. *Ferroelectrics*, 36:327, 1981.

[33] L.A. Bursill and C. Y. Lin. *Philosophical Magazine B*, 54:157, 1986.

[34] Schneck, J. Primot, R. von der Muhl, and J Ravez. *Solid State Comm.*, 21:57, 1977.

[35] J.L.B. Faria, P.T.C. Freire, A.P. Ayala, Melo.F.E.A., J. Mendes Filho, C.W.A. Paschoal, A.I. Santos, and J. A. Eiras. *J. Raman Spec.*, 34:826, 2003.

[36] Toledano. *Phys. Rev. B*, 12:943, 1975.

[37] Schneck and D. Paquet. *Ferroelectrics*, 21:577, 1978.

[38] T.G. Huang, Z. Xu, D. Viehland, and R. R. Neurgaonkar. *J.Appl.Phys*, 77(4):1677, 1995.

[39] U.B. Dorfler, R. Piechatzek, T. Woike, M.K. Imlau, V. Wirt, L. Bohaty, T. R. Volk, R. Pankrath, and M. Wohlecke. *Applied Physics B*, 68:843–848, 1999.

[40] R. R. Neurgaonkar and L.E. Cross. *Mater Res Bull*, 21:893, 1986.

[41] N.M. Shorrocks, R.W. Whatmore, and S.T. Liu. *J.Phys D*, 15:2469, 1982.

[42] S. Ducharme, J. Feinberg, and R.R. Neurgaonkar. *IEEE JOURNAL OF QUANTUM ELECTRONICS.*, QE-23(12):2116, 1987.

[43] T.R. Volk, V.Y. Salobutin, L. I. Ivleva, N.M. Polozkov, R. Pankrath, and M. Woehlecke. *Physics of the solid state*, 42(11):2066–2073, 2000.

[44] R.A. Vasquez, M.D. Ewbank, and R. R. Neurgaonkar. *opt.commun*, 80(3,4):253, 1991.

[45] T. R. Volk, D. Isakov, V.Y. Salobutin, L. I. Ivleva, P. Lykov, V. Ramazaev, and M. Wohlecke. *Solid State Comm.*, 130:223–226, 2004.

[46] N.A. Petersev, A.G. Zembligotov, and A Tagantsev. *Phys. Rev. Lett.*, 80(9):1988, 1998.

[47] J. R. Oliver, R. R. Neurgaonkar, and L.E. Cross. *J.Appl.Phys*, 64(1):37, 1988.

[48] Shrouth, L.E. Cross, P. Moses, H.A. McKinstry, and R. R. Neurgaonkar. *Proceedings of the IEEE 1980 Ultrasonic Smposium*, page 414, 1980.

[49] J. Koo, J. H. Jang, and B. S. Bae. *Journal of the American Ceramic Society*, 84(1):193–199, 2001.

[50] Y. H. Xu, C. J. Chen, R. Xu, and J. D. Mackenzie. *Physical Review B*, 44(1):35–41, 1991.

[51] M. J. Nystrom, B. W. Wessels, W. P. Lin, G. K. Wong, D. A. Neumayer, and T. J. Marks. *Applied Physics Letters*, 66(14):1726–1728, 1995.

[52] Z. Lu, R. S. Feigelson, R. K. Route, S. A. Dicarolis, R. Hiskes, and R. D. Jacowitz. *Journal of Crystal Growth*, 128(1-4):788–792, 1993.

[53] M. Cuniot-Ponsard, J. M. Desvignes, B. Ea-Kim, and E. Leroy. *Journal of Applied Physics*, 93(3):1718–1724, 2003.

[54] C. A. Jong and J. Y. Gan. *Japanese Journal of Applied Physics Part 1*, 39(2A):545–550, 2000.

[55] S. S. Thony, K. E. Youden, J. S. Harris, and L. Hesselink. *Applied Physics Letters*, 65(16):2018–2020, 1994.

[56] H. F. Cheng, C. T. Hu, and I. N. Lin. *Japanese Journal of Applied Physics Part 1-*, 36(1A):284–288, 1997.

[57] K. Kakimoto, H. Kakemoto, A. Baba, S. Fujita, and Y. Masuda. *Journal of the European Ceramic Society*, 21(10-11):1569–1572, 2001.

[58] A. D. Li, C. L. Mak, K. H. Wong, M. M. T. Ho, T. B. Tang, K. M. Yeung, D. Wu, and S. Z. Yang. *Japanese Journal of Applied Physics Part 1*, 41(11B):6806–6809, 2002.

[59] H. Liu, S. T. Li, G. K. Liu, W. Jia, and F. E. Fernandez. *Journal of Luminescence*, 83-4:367–371, 1999.

[60] C. J. Forst, C. R. Ashman, K. Schwarz, and P. E. Blochl. *Nature*, 427(6969):53–56, 2004.

[61] H. F. Cheng, G. S. Chiou, K. S. Liu, and I. N. Lin. *Applied Surface Science*, 114:217–221, 1997.

[62] S. B. Xiong, Z. M. Ye, X. Y. Chen, X. L. Guo, S. N. Zhu, Z. G. Liu, C. Y. Lin, and Y. S. Jin. *Applied Physics a-Materials Science and Processing*, 67(3):313–316, 1998.

[63] X. L. Guo, Z. G. Liu, X. Y. Chen, S. N. Zhu, S. B. Xiong, W. S. Hu, and C. Y. Lin. *Journal of Physics D-Applied Physics*, 29(6):1632–1635, 1996.

[64] D. Trivedi, P. Tayebati, and M. Tabat. *Applied Physics Letters*, 68(23):3227–3229, 1996.

[65] C. M. Rouleau, G. E. Jellison, and D. B. Beach. *Applied Physics Letters*, 82(18):2990–2992, 2003.

[66] Y. S. Yang, M. K. Ryu, H. J. Joo, S. H. Lee, S. J. Lee, K. Y. Kang, and M. S. Jang. *Applied Physics Letters*, 76(23):3472–3474, 2000.

[67] K. Tanaka, O. Nakagawara, M. Nakano, T. Shimuta, H. Tabata, and T. Kawai. *Japanese Journal of Applied Physics Part 1*, 37(11):6142–6145, 1998.

[68] T. W. Chiu, N. Wakiya, K. Shinozaki, and N. Mizutani. *Thin Solid Films*, 426(1-2):62–67, 2003.

[69] K Nishio, Y Watanabe, and T Tsuchiya. *J. Sol-gel Sci. Tech.*, 26:245–250, 2003.

[70] K. Kakimoto, H. Kakemoto, and A. Baba. *J. Mater. Sci.*, 37:3045–3051, 2002.

[71] K Nishio, Seki N, Thongrueng J, Watanabe Y, and R. Tsuchiya. *J.Sol-Gel Sci. Tech.*, 16(1-2):37–45, 1999.

[72] J Zhao, Y Li, X Liu, H Zhang, and B Wang. *Materials Letters*, 58:1456–1460, 2004.

[73] W Sakamoto, T Yogo, and K Kikuta. *Journal of American Ceramic Society*, 79:2283–2288, 1996.

[74] H. F. Cheng, G. S. Chiou, K.S. Liu, and I.N. Lin. *Appl. Surf. Sci.*, 113-114:217–221, 1997.

[75] R. G. Mendes, E. B. Araujo, and J. A. Eiras. *Material Research*, 4(2):113–116, 2001.

[76] S.P. Alpay, I.B. Misiriliogu, A. Sharma, and Z.G. Ban. *J.Appl.Phys*, 95(12):8118, 2004.

[77] J.W. Matthews. *Epitaxial Growth.* Academic Press, New York, 1975.

[78] D Bauerle. *Laser processing and chemistry.* Springer, 2000.

[79] D.B. Chrisey and K.H. Graham. *Pulsed Laser Deposition of Thin Films.* Wiley Interscience, 1994.

[80] T.J. Jackson and S. B. Palmer. *J. Phys. D, Appl. Phys*, 27:1581, 1994.

[81] P.R. Willmott and J.R. Huber. *Rev. Mod.Phys*, 72(1):315, 2000.

[82] Z. Y. Zhang, Z. X. Han, and G. S. Dulikravich. *Journal of Applied Physics*, 90(12):5889–5897, 2001.

[83] L.M. Doeswijk, G. Rijnders, and D. H. A. Blank. *Appl. Phys. A*, 78:263–268, 2004.

[84] M. Tyunina, C. Wittborn, C. Bjormander, and V. Rao. *J. Vac. Sci. Technol. A*, 16(4):2381, 1998.

[85] D. H. A. Blank, R.P.J. Ijsselsteijn, P.G. Out, H.J.H. Kuiper, J. Flokstra, and H. Rogalla. *Mat. Sci. Eng. B*, 13:67, 1992.

[86] B. Schey, W. Biegel, M. Kuhnn, and B. Strizker. *Appl. Phys. A*, 69(suppl):S419, 1999.

[87] S. I. Anisimov, D. Bauerle, and B. S. Lukyanchuk. *Physical Review B*, 48(16):12076–12081, 1993.

[88] T. Scharf and H. U. Krebs. *Applied Physics a-Materials Science and Processing*, 75(5):551–554, 2002.

[89] T. E. Itina. *Journal of Applied Physics*, 89(1):740–746, 2001.

[90] S. Proyer, E. Stangl, M. Borz, B. Hellebrand, and D. Bauerle. *Physica C*, 257(1-2):1–15, 1996.

[91] K. Bierleutgeb and S. Proyer. *Applied Surface Science*, 110:331–334, 1997.

[92] P. E. Dyer, S. R. Farrar, and P. H. Key. *Applied Surface Science*, 54:255–263, 1992.

[93] D. S. Misra and S. B. Palmer. *Physica C*, 176(1-3):43–48, 1991.

[94] P. E. Dyer, R.D. Greenough, A. Issa, and P. H. Key. *Appl. Phys lett*, 53:534, 1988.

[95] M. Nakano, H. Tabata, K. Tanaka, Y. Katayama, and T. Kawai. *Japanese Journal of Applied Physics Part 2-Letters*, 36(10A):L1331–L1332, 1997.

[96] J. G. Zhu, S. K. Singh, P. A. Thomas, and S. B. Palmer. *Philosophical Magazine a-Physics of Condensed Matter Structure Defects and Mechanical Properties*, 79(11):2869–2876, 1999.

[97] J.S. Yeo, K. E. Youden, T.G. Huang, L. Hesselink, and J. S. Harris. *Mat.Res.Soc.Symp.Proc.*, 401:225, 1996.

[98] P. Tayebati, D. Trivedi, and M. Tabat. *Applied Physics Letters*, 69(8):1023–1025, 1996.

[99] F. E. Fernandez, H. M. Liu, C. M. Jin, and W. Y. Jia. *Integrated Ferroelectrics*, 29(1-2):A111–A126, 2000.

[100] D.J. O'Connor, B.A. Sexton, and R.St.C. Smart. *Surface Analysis Methods in Material Science*, volume 23 of *Spiringe series in surface science.* Springer, 2003.

[101] M.H. Loretto. *Electron Beam Analysis of Materials.* Chapman and Hall, 1984.

[102] D.P. Woodruff and T.A. Delchar. *Modern Techniques of Surface Science.* Solid State Science. Cambridge University Press, 1999.

[103] T. T. Fang and N. T. Wu. *Journal of Materials Science*, 30(13):3376–3382, 1995.

[104] W. J. Lee and T. T. Fang. *Journal of the American Ceramic Society*, 81(4):1019–1024, 1998.

[105] D. Briand, S. Heimgartner, M. Leboeuf, M. Dadras, and N.F. de Rooij. *Mat.Res.Soc.Symp.Proc.*, 729:63–68, 2002.

[106] T. Maeder, L. Sagalowicz, and P. Muralt. *Jpn. J. Appl. Phys*, 37:2007–2012, 1998.

[107] J.H. van der Merwe, J. Woltersdorf, and W.A. Jesser. *Mat. Sci. Eng.*, 81:1–33, 1986.

[108] F.C. Franck and J.H. van der Merwe. *Proc.R.Soc.London Ser.A*, 198:217, 1949.

[109] J.H. van der Merwe. *Philosophical Magazine a*, 45:127,145,159, 1982.

[110] J.H. van der Merwe. *Jour. Appl. Phys*, 41:4725, 1970.

[111] E. Bauer. *Appl. Surf. Sci.*, 11-12:479, 1982.

[112] F.C. Franck and J.H. van der Merwe. *Proc.R.Soc.London Ser.A*, A189:205, 1949.

[113] M. Volmer and A. Weber. *Z.Phys. chem*, 119:277, 1926.

[114] I.N. Stransky and L. Krastanow. *Sitzungsber. Akad.Wiss.Wien, Math-Naturwiss. Klasse*, 146:797, 1937.

[115] J.H. van der Merwe. *Chemistry and Physics of Solid Surfaces*, volume 5. Springer, Berlin, 1984.

[116] E. Bauer. *Z. Kristallogr.*, 110:423, 1958.

[117] E. Bauer and J.H. van der Merwe. *Phys. Rev. B*, 33:3657, 1986.

[118] J.W. Matthews and A.E. Blakeslee. *J. Cryst. Growth*, 27:118125, 1974.

[119] J.W. Matthews. *J. Vac. Sci. Technol.*, 12:126, 1975.

[120] H. J. Osten, J. Klatt, G. Lippert, B. Dietrich, and E. Bugiel. *Phys. Rev. Lett.*, 69:450ñ453, 1992.

[121] U. Kohler, O. Jusko, B. Muller, M. Hornvonhoegen, and M. Pook. *Ultramicroscopy*, 42:832–837, 1992.

[122] A. Fissel, R. Akhtariev, and W. Richter. *Thin Solid Films*, 380(1-2):42–45, 2000.

[123] R. Koch, D. Winau, and K. H. Rieder. *Physica Scripta*, T49B:539–543, 1993.

[124] J.A. Floro, S.J. Hearne, J.A. Hunter, and P. Kotula. *J.Appl.Phys*, 89(9):4886, 2001.

[125] A.L. Shulls and F. Spaepen. *J.Appl.Phys*, 80:6243, 1996.

[126] R. C. Cammarata. *Progress in Surface Science*, 46:1, 1994.

[127] R.C. Cammarata, T.M. Trimble, and D.J. Srolovitz. *Journal of Materials Research*, 15(11):2468, 1999.

[128] R.W. Hoffmann. *Thin Solid Films*, 34:185, 1976.

[129] W D Nix and B.M Clemens. *J. Mater. Res*, 14:3467, 1999.

[130] L.B. Freund and E. Chason. *J.Appl.Phys*, 89:4866, 2001.

[131] C. V. Thompson. *J. Mater. Res*, 8:237, 1993.

[132] M. A. Phillips, V. Ramaswamy, B. M. Clemens, and W. D. Nix. *Journal of Materials Research*, 15(11):2540–2546, 2000.

[133] V. Ramaswamy, M. A. Phillips, W. D. Nix, and B. M. Clemens. *Materials Science and Engineering a-Structural Materials Properties Microstructure and Processing*, 319:887–892, 2001.

[134] K. Szot and W. Speier. *Physical Review B*, 60(8):5909–5926, 1999.

[135] Koster Gertjan, Rijnders Guus, Blank Dave H.A., and Rogalla Horst. *Physica C*, 339:215–230, 2000.

[136] K. Szot, W. Speier, R. Carius, U. Zastrow, and W. Beyer. *Physical Review Letters*, 88(7):075508, 2002.

[137] M. Kawasaki, A. Ohtomo, T. Arakane, K. Takahashi, M. Yoshimoto, and H. Koinuma. *Applied Surface Science*, 107:102–106, 1996.

[138] G. Koster, B. L. Kropman, G. J. H. M. Rijnders, D. H. A. Blank, and H. Rogalla. *Applied Physics Letters*, 73(20):2920–2922, 1998.

[139] W. M. Sigmund, M. Rotov, Q. D. Jiang, J. Brunen, J. Zegenhagen, and F. Aldinger. *Applied Physics a-Materials Science and Processing*, 64(2):219–220, 1997.

[140] Hiroyuki Tanaka and Tomoji Kawai. *Surface Science*, 365(2):437–442, 1996.

[141] Damjanovic. *Rep. Prog. Phys*, 61:1267, 1998.

[142] F. Chu and N. Setter. *J.Appl.Phys*, 74(8):5129, 1993.

[143] F. Chu, I.M. Reaney, and N. Setter. *J.Appl.Phys*, 77(4):1671, 1994.

[144] O Bidault, P Goux, M Kchikech, M Belkaoumi, and M Maglione. *Phys. Rev. B*, 49(12):7868–7873, 1994.

[145] C Ang, Z Yu, and L.E. Cross. *Phys. Rev. B*, 62(1):228–236, 2000.

[146] C Ang, Z Yu, P.Q. Vilarinho, Q.P. Mantas, and J.L. Baptista. *J.Appl.Phys*, 83(9):4874, 1998.

[147] D. Viehland, J. H. Jang, L.E. Cross, and M. Wuttig. *J.Appl.Phys*, 68:2916, 1990.

[148] E.V. Colla, E. Yu Koroleva, N.M. Okuneva, and S.B. Vakhrushev. *Phys. Rev. lett*, 74:1681, 1995.

[149] A Tagantsev. *Phys. Rev. lett*, 72(7):1100, 1994.

[150] J. Dec, W. Kleemann, T. Woike, and R. Pankrath. *Eur. Phys. J. B*, 14:627, 2000.

[151] A.S. Bhalla, R. Guo, L.E. Cross, G. Burns, and F.H. Dacol. *Physical Rev. B*, 36(4):2030, 1987.

[152] V.V. Gladkii, V.A. Kirikov, T. R. Volk, D. Isakov, and E.S. Ivanova. *Phys. solid state*, 45(11):2171, 2003.

[153] V.V. Gladkii, V.A. Kirikov, T. R. Volk, and L. I. Ivleva. *J. Exp. Theor. Phys*, 93(3):596, 2001.

[154] S.M. Sze. *Physics of semiconductor devices.* ii edition, 1981.

Acknowledgments

I want to thank my thesis director Prof. Nava Setter, Prof. Paul Muralt and Dr. Alexander Tagantsev, for the extremely valuable experience made at the Ceramic Laboratory.

The collaboration with Dr. Marco Cantoni, who provided the TEM observations, made possible the detailed study of the film growth and is gratefully acknowledged. I would like to thank furthermore all those that, not directly involved with my project, have always been available for discussion and help: Dr. Dragan Daminanovich, Dr. Enrico Colla, Dr. Ludovic Arzel, Dr. Sandrin Gentil, Dr. Simon Buhelmann, Lino Olivetta, Jacques Castano, David Metral, Nicholas Santopulos, Eva Favre. The contribution of the mechanic workshop as well as the support of the staff of CMI, have been of fundamental importance for the experimental work of my thesis and the good functioning of the "Sputnik".

I thank all the Ph.D. students at LC contemporary with me, starting from my office mate Marko, whit whom I shared a great time in Lausanne and elsewhere.

I am grateful to Ms. Zimmermann of ACIDE for the interest shown and the support given in the last period of my permanence at EPFL and I would like to thank Prof. Rappaz for his intervention in the solution of my case.

I am in debt with Prof. Ludwig Gauckler of the Ceramic Laboratory in ETHZ, for giving me the opportunity to work in his lab while still completing my thesis.

Curriculum Vitae

Personal

Name:	Anna Infortuna
Birth:	11 January 1968, Moncalieri (To)
Nationality:	Italian

Education

1995	Physics degree, Faculty of Mathematical Physical and Natural Science, Torino University.
1987	Scientific Maturity, Liceo Scientifico Ettore Mayorana , Moncalieri, Torino.

Professional

since 2004	Research Assistant at ETH Zuerich
2000 - 2004	Research Assistant at EPF Lausanne
1997 - 1999	Internship at IEN "G.Ferraris" Torino
1995 - 1997	External Consultant for ABB Ricerca, Milano

Publications

V. Basso, G. Bertotti, A. Infortuna, M. Pasquale

Preisach model study of the connection between magnetic and microstructural properties of soft magnetic materials

IEEE Transactions on Magnetics, Vol: 31(6) pp.4000-4005, 1995

E. Ferrara, A. Infortuna, A. Magni, M. Pasquale

Structural and magnetic analysis of amorphous $Fe_{64}Co_{21}B_{15}$ *ribbons*

IEEE Transactions on Magnetics, Vol: 33(5) pp.3781-3783, 1997

M.Pasquale, F.Offi, A.Infortuna, E.Ferrara, C.Beatrice, G.Bertotti, C.Appino

Histeresys modeling and microstructural analysis of soft amorphous alloys

J.Phys. IV France 8, 1998

M.Pasquale, A. Infortuna, L. Martino, C. Sasso, C. Beatrice, S.H. Lim

Magnetic properties of TbFe thin films under applied stress

Journal of Magnetism and Magnetic Materials. Vol. 215, pp. 769-771. 2000

A. Infortuna, P. Muralt, , M. Cantoni, A. Tagantsev, N. Setter

Microstructural and electrical properties of $(Sr, Ba)Nb_2O_6$ *thin films grown by pulsed laser deposition*

Journal of the European Ceramic Society, Vol 24(6),Pages 1573-1577, 2004

A.Bieberle-Hütter, D.Beckel, U.P.Muecke, J.L.M.Rupp, A.Infortuna, L.J.Gauckler

Micro-Solid oxide fuel cells as battery replacement

mst news, No.4/05, August 2005, pag. 12